



Circuits and Systems

Mekelweg 4,
2628 CD Delft
The Netherlands

<http://ens.ewi.tudelft.nl/>

CAS-2019-00

M.Sc. Thesis

An Investigation of the Medical Ultrasound Image Sparse Spaces used for the Model-Based Imaging

Zheheng Liu

Abstract

In this thesis, we investigate a sparse basis for ultrasound images, so that we can use sparse regularization in imaging. Actually, there are few previous researches explicitly demonstrating that medical ultrasound images can be sparsified for some dictionary. We consider various orthogonal transforms such as wavelet transforms, cosine transforms and wave atom transforms. Then, we perform those transforms on various ultrasound images and analyze their sparsity. These ultrasound images include the images of two computer ultrasound phantoms and beamformed ultrasound images with good quality from real people. We looked at sparsity of the true pre-beamformed images, as well as beamformed images. We also consider constructing a specific ultrasound image dictionary using the K-SVD algorithm. We observed that, the pre-beamformed images hardly have no sparse basis, and the sparsity of beamformed images will only increase slightly if we use different 1D-DWT in each direction. We also found that the wide overdetermined dictionary generated by K-SVD significantly increases sparsity. After this, we simulate the ultrasound image reconstruction from the ultrasound RF measurements, and we analyze the effects of the different sparse spaces on the reconstruction performance. We observed that, the l_1 -regularization can work for ultrasound imaging better than l_2 -regularization, but the orthogonal transforms as well as the dictionary do not improve the reconstruction image quality much.

An Investigation of the Medical Ultrasound Image Sparse Spaces used for the Model-Based Imaging

THESIS

submitted in partial fulfillment of the
requirements for the degree of

MASTER OF SCIENCE

in

ELECTRICAL ENGINEERING

by

Zheheng Liu
born in Baotou, China

This work was performed in:

Circuits and Systems Group
Department of Microelectronics & Computer Engineering
Faculty of Electrical Engineering, Mathematics and Computer Science
Delft University of Technology



Delft University of Technology

Copyright © 2019 Circuits and Systems Group
All rights reserved.

DELFT UNIVERSITY OF TECHNOLOGY
DEPARTMENT OF
MICROELECTRONICS & COMPUTER ENGINEERING

The undersigned hereby certify that they have read and recommend to the Faculty of Electrical Engineering, Mathematics and Computer Science for acceptance a thesis entitled “**An Investigation of the Medical Ultrasound Image Sparse Spaces used for the Model-Based Imaging**” by **Zheheng Liu** in partial fulfillment of the requirements for the degree of **Master of Science**.

Dated: 11-2018

Chairman:

prof.dr.ir. G.J.T. Leus

Advisors:

dr.ir. P. Kruizinga

ir. P.Q. van der Meulen

Committee Members:

dr.ir. M.D. Verweij

Abstract

In this thesis, we investigate a sparse basis for ultrasound images, so that we can use sparse regularization in imaging. Actually, there are few previous researches explicitly demonstrating that medical ultrasound images can be sparsified for some dictionary. We consider various orthogonal transforms such as wavelet transforms, cosine transforms and wave atom transforms. Then, we perform those transforms on various ultrasound images and analyze their sparsity. These ultrasound images include the images of two computer ultrasound phantoms and beamformed ultrasound images with good quality from real people. We looked at sparsity of the true pre-beamformed images, as well as beamformed images. We also consider constructing a specific ultrasound image dictionary using the K-SVD algorithm. We observed that, the pre-beamformed images hardly have no sparse basis, and the sparsity of beamformed images will only increase slightly if we use different 1D-DWT in each direction. We also found that the wide overdetermined dictionary generated by K-SVD significantly increases sparsity. After this, we simulate the ultrasound image reconstruction from the ultrasound RF measurements, and we analyze the effects of the different sparse spaces on the reconstruction performance. We observed that, the l_1 -regularization can work for ultrasound imaging better than l_2 -regularization, but the orthogonal transforms as well as the dictionary do not improve the reconstruction image quality much.

Acknowledgments

I really thank Prof. G. Leus, Mr. P. Kruizinga and Mr. P. van der Meulen for their help. Without their guidance, I cannot finish this thesis. They taught me a lot, and what I learned from them will benefit my entire life.

I am very grateful to my parents. They provide me economic support which is not an easy thing for them. But they never show me any of their difficulties, furthermore, they care about my happiness and unhappiness.

I also want to really thank my girlfriend. She is a smart and considerate person. She helps me a lot and cares about me, and I also learned a lot from her.

Zheheng Liu
Delft, The Netherlands
11-2018

Contents

Abstract	v
Acknowledgments	vii
1 Introduction	1
1.1 Overview	1
1.2 The organization of this thesis	3
2 Methods	5
2.1 The signal model	5
2.2 The reconstruction algorithms	6
2.2.1 An introduction to LSQR	6
2.2.2 An introduction to YALL1	7
2.3 The sparse bases	7
2.3.1 The model of medical US phantoms	8
2.3.2 An introduction to several transformations	8
2.3.3 The K-SVD sparse dictionary learning algorithm	10
3 Simulation results and analysis	13
3.1 The sparse space of the linear interpolation images of the phantom US scattering intensity	13
3.1.1 The fetus phantom US scattering intensity linear interpolation image	14
3.1.2 The kidney phantom linear interpolation image	19
3.1.3 Analysis	24
3.2 The sparse space of the ultrasound reconstruction images	24
3.2.1 The fetus phantom 21-PW MF image	24
3.2.2 The experimental carotid MF image	34
3.3 Sparse dictionary learning for the US images	42
3.4 Reconstruction from the simulated US measurements	52
4 Conclusions	59
5 Future work	61

Introduction

1.1 Overview

Ultrasound (US) imaging plays an important role in medical imaging. Compared with many other imaging techniques such as CT and MRI, US imaging is safer and more convenient and less expensive. Since US is non-ionizing and non-carcinogenic, it is able to be safely used in the human body, especially fetus. US can also be used for real-time imaging, because of its fast imaging and easy operation.

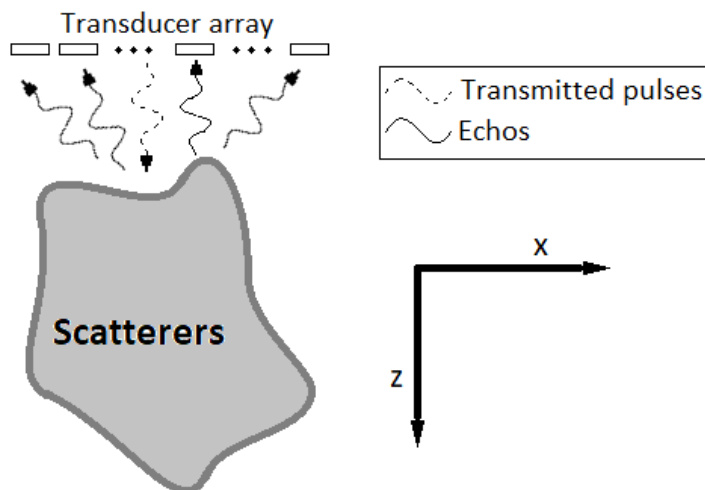


Figure 1.1: Sketch of the US pulse propagation during US imaging

Medical US imaging usually uses the transducer arrays to transmit the US pulses and receive the echos. The imaging procedure can be roughly described as follows. As Figure 1.1 shows, firstly, the transducers emit the US pulses to the tissue. And the US pulses are scattered in the tissue. Then, the transducers receive the echos caused by the scattering. Finally, the US images of the tissue can be reconstructed from the received echo data. In this way, the US images can show the scattering intensity at the different positions of the tissue. These US images are also known as the B-mode (brightness mode) ultrasound images, and what are shown to the doctor are usually the log-compressed versions of these images.

Currently, delay-and-sum (DS) beamforming is commonly applied to reconstruct the US image, but the image resolution is not sufficiently high with DS or the other conventional beamforming techniques. One of the reasons is that the prior knowledge is not fully exploited. As an example, DS merely utilizes the geometrical information in the spatial domain.

Therefore, acoustic wavefield theory ought to be considered to reconstruct the US

images. That is also explained in [21], [37] and [35]. It is known as the *inverse scattering problem* in the acoustic theory to reconstruct the US images from the received scattering echo data. With the Born approximation, the relationship of the variables in this problem can be expressed as the linear equation (1.1).

$$\mathbf{y} = \mathbf{A}\mathbf{x} + \mathbf{n}. \quad (1.1)$$

Where $\mathbf{x} \in \mathbb{R}^{N \times 1}$ is the discretized US image in linear scale (N is the number of the image pixels), $\mathbf{y} \in \mathbb{C}^{M \times 1}$ is the received sampled echo data (M is the total number of the data samples received by all the transducers), $\mathbf{A} \in \mathbb{C}^{M \times N}$ is the known array manifold matrix[12] and $\mathbf{n} \in \mathbb{C}^{M \times 1}$ is the additive noise. So the US imaging becomes linear inverse problem.

However, *inverse scattering problems* are always ill-posed, so some regularization methods are necessary to apply. Namely, in (1.1), \mathbf{A} is always an ill-conditioned matrix that has very small non-zero singular values. These small singular values badly increase the impacts of the noise on the US image reconstruction. Proper regularization can suppress the effect of these small singular values. The truncated SVD (TSVD) regularization can be used to remove these small singular values, and the number of the remaining singular values is a parameter that affects the regularization performance. Tikhonov regularization is the most commonly used regularization method, which uses the l_2 -norm. And l_2 -regularization is the simplest case of Tikhonov regularization. With the l_2 -regularization, the least squares (LS) problem (1.2) can represent the linear inversion problem for the US imaging. $\|\cdot\|_2$ denotes the l_2 -norm, and ρ is the parameter that controls the importance of the l_2 -regularization term.

$$\min_{\mathbf{x}} \{ \|\mathbf{y} - \mathbf{A}\mathbf{x}\|_2^2 + \rho \|\mathbf{x}\|_2^2 \} \quad \text{s.t. } \mathbf{x} \in \mathbb{R}^N. \quad (1.2)$$

Currently, there is an increasing focus on using the l_1 -norm. One of the reasons is the proposition of compressive sensing (CS). If the signal to be reconstructed has a sparse space, the CS can possibly break through the Shannon sampling rate. The l_1 -norm plays an important role in the CS. Recently, there are many studies about applying CS to US imaging. What follow are some studies about applying CS to RF data. The study in [23] regards the *sym8* wavelet transform as the sparse space of the RF data; the wave atom transform is used as the sparse space for RF data in [22]. Other studies assume that the US image is sparse in some domain. For example, [30] and [8] have regarded the spatial domain as the sparse space, although it cannot be always assumed that the US image is sparse in the spatial domain for human tissue; the compression in [28] is obtained by subsampling the scanning lines in the image and the k-space is the sparse space; the sparse space in [6] is the curvelet transform; [5] uses the concatenation of some Daubechies wavelet bases as the sparse space.

Another reason that we are interested in sparsity is that, l_1 -regularization can also make the US image reconstruction without compression have better performance, if there is a good sparse space for the US images. If $\Psi \in \mathbb{C}^{K \times N}$ is assumed to be the transform matrix of the US image sparse space (K is the number of the transformation coefficients), (1.3) expresses the linear inversion problem for the US image reconstruc-

tion, with the l_1 -regularization in this sparse space.

$$\min_{\mathbf{x}} \{ \|\mathbf{y} - \mathbf{A}\mathbf{x}\|_2^2 + \tau \|\Psi\mathbf{x}\|_1 \} \quad \text{s.t. } \mathbf{x} \in \mathbb{R}^N. \quad (1.3)$$

In (1.3), $\|\cdot\|_1$ denotes the l_1 -norm, and τ is a parameter to control the weight of the l_1 -regularization term.

Since a sparsity-constraint on the image \mathbf{x} can improve the imaging performance both with and without compression, it is very helpful to find a good sparse space of the US images. However, all the previous studies that assume sparsity of $\Psi\mathbf{x}$ did not explicitly demonstrate that US images can be sparsified for some Ψ . Therefore, this thesis analyzes and experiments the sparsity of the medical US linear-scale image in the various transform spaces.

1.2 The organization of this thesis

In Chapter 1, the background is introduced and the motivation of this thesis is explained. Chapter 2 gives the signal model and introduces the image reconstruction algorithms and describes some linear transformations that are possibly the good sparse spaces to improve the reconstruction performance, and the dictionary learning algorithm K-SVD is introduced at the end of this chapter. Chapter 3 shows the simulation results. Section 3.1 in Chapter 3 gives the sparsity analysis for the scattering intensity images of the phantoms before being beamformed, and in Section 3.2, we analyze beamformed MF images. Section 3.3 contains the analysis for the performance of the K-SVD on the beamformed carotid US images from several volunteers. The reconstruction from the simulated US measurements are shown in Section 3.4. Chapter 4 draws the conclusions for this thesis. Chapter 5 discusses the future work.

In this chapter, the signal model is firstly described in Section 2.1. Section 2.2 explains the algorithms used for the image reconstruction such as LSQR[26] and YALL1[40], and Section 2.3 introduces some transformations and the K-SVD algorithm that are later used to analyze the US image sparse space.

2.1 The signal model

The signal model here is described by (1.1). \mathbf{y} is a vector which contains all the echo samples received by each transducer. The imaging domain scattering intensity is discretized in the spatial domain, so the imaging domain is divided into many grid points, i.e., the US image pixels. The columns of \mathbf{A} one-to-one correspond to these grid points. Each column contains the echo data of the corresponding grid point, and the echo samples in each column are arranged in same way as \mathbf{y} . Therefore, the received echo data \mathbf{y} is approximated by a linear combination of every grid's echo data, which is formulated as $\mathbf{y} = \mathbf{A}\mathbf{x}$. \mathbf{x} contains the scattering intensity of each grid. Here, the scattering intensity of each grid is represented by the intensity of a point scatterer at this grid center. However, there are a large number of the signal samples because of the high sampling rate, which makes \mathbf{A} become a very big matrix.

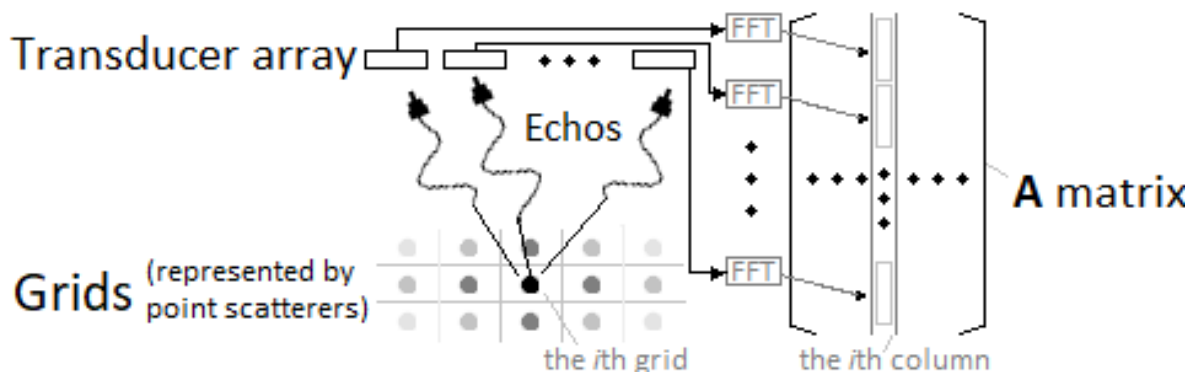


Figure 2.1: Sketch of \mathbf{A} matrix construction.

Since the pulse is approximately bandlimited, the amount of data can be reduced by truncating the FFT of the pulse-echo signals. In this way, the construction of \mathbf{A} is shown as Figure 2.1. In both \mathbf{A} and \mathbf{y} , the signal samples received by each transducer are substituted by their FFT coefficients of a limited band. Since the structure of every \mathbf{A} column and \mathbf{y} are the same, the constitution of the i th column is explained here as an example. Suppose the vector \mathbf{s}'_k contains the echo samples from the i th grid point in the

time domain received by the k th element of the transducer array. $\mathcal{F}\{\mathbf{s}'_k\}$ is the Fourier transform of \mathbf{s}'_k . $\mathbf{s}'_{F,k}$ contains the frequency samples that are selected from $\mathcal{F}\{\mathbf{s}'_k\}$ within certain frequency band. At last, the i th column of \mathbf{A} is $[\mathbf{s}'_{F,1}{}^T, \mathbf{s}'_{F,2}{}^T, \dots]{}^T$.

The environment noise, together with the signal errors caused by the approximation, is regarded as additive white Gaussian noise (AWGN). So the signal model is formulated as (1.1). As the FFT coefficients are complex, the AWGN should correspondingly be complex Gaussian distributed when (1.1) is formulated in Fourier domain.

2.2 The reconstruction algorithms

Having obtained a linear signal model, this section introduces some algorithms for solving this linear inverse problem (i.e. reconstructing \mathbf{x}), namely, the LSQR and YALL1 algorithms.

The matrix \mathbf{A} is always very big due to a large number of the image pixels and the signal samples. As a result, there are so many computations with the common algorithms to solve \mathbf{x} that it costs a lot of time and computer memory. Therefore, some fast and sparse algorithms are utilized in this thesis for this linear inverse problem.

2.2.1 An introduction to LSQR

LSQR is a good iterative algorithm for solving the large LS problems. It does not require much additional computer memory, since it does not store big matrices besides \mathbf{A} and does not need to compute any matrix inversion. It is based on the Golub-Kahan bidiagonalization process. Algorithm 1 shows the procedure of LSQR.

Algorithm 1 LSQR

- 1: **Given:** α_1, β_1 , unit vectors \mathbf{u}_1 and \mathbf{v}_1 satisfy $\beta_1\mathbf{u}_1 = \mathbf{y}$ and $\alpha_1\mathbf{v}_1 = \mathbf{A}^H\mathbf{u}_1$; $\mathbf{w}_1 = \mathbf{v}_1$, $\mathbf{x}_0 = \mathbf{0}$, $\bar{\phi}_1 = \beta_1$, $\bar{\rho}_1 = \alpha_1$.
 - 2: For $i=1, 2, 3, \dots$ **iterate:**
 - 3: $\Rightarrow \beta_{i+1}\mathbf{u}_{i+1} = \mathbf{A}\mathbf{v}_i - \alpha_i\mathbf{u}_i$ ▷ The bidiagonalization
 - 4: $\alpha_{i+1}\mathbf{v}_{i+1} = \mathbf{A}^H\mathbf{u}_{i+1} - \beta_{i+1}\mathbf{v}_i$
 - 5: $\Rightarrow \rho_i = \sqrt{\bar{\rho}_i^2 + \beta_{i+1}^2}$ ▷ The orthogonal transformation
 - 6: $c_i = \bar{\rho}_i/\rho_i$, $s_i = \beta_{i+1}/\rho_i$
 - 7: $\theta_{i+1} = s_i\alpha_{i+1}$, $\bar{\rho}_{i+1} = -c_i\alpha_{i+1}$, $\phi_i = c_i\bar{\phi}_i$
 - 8: $\bar{\phi}_{i+1} = s_i\bar{\phi}_i$
 - 9: $\Rightarrow \mathbf{x}_i = \mathbf{x}_{i-1} + (\phi_i/\rho_i)\mathbf{w}_i$, $\mathbf{w}_{i+1} = \mathbf{v}_{i+1} - (\theta_{i+1}/\rho_i)\mathbf{w}_i$ ▷ Update \mathbf{x} and \mathbf{w}
-

The residuals of the problem can be reduced monotonically, as the number of LSQR iterations increases. LSQR can solve the least square problems with l_2 -regularization, like (1.2) on page 2. In addition, limiting the number of LSQR iterations is similar to a filtered SVD inverse[15]. The ready-made LSQR solver is available online[25].

2.2.2 An introduction to YALL1

As for the LS problems with l_1 -regularization, there are many iterative algorithms that can save much time and computer memory, such as TwIST[7], FISTA[3], NESTA[4], SPGL1[34] and YALL1. TwIST (Two-step Iterative Shrinkage/Thresholding Algorithm) is a commonly used solver based on soft thresholding and TwSIM (Two-Step Iterative Method), for the l_1 -regularized LS problem like (1.3) on page 3. Similar to TwIST, FISTA (Fast Iterative Shrinkage-Threshold Algorithm) combines the IST algorithm with Nesterov's accelerated gradient descent (instead of TwSIM) to solve the problems like (1.3). Unlike TwIST and FISTA and YALL1, NESTA and SPGL1 solve the problems that minimize the l_1 -norm and constrain the l_2 -norm to no more than a certain value. For the problems in this thesis, we found that YALL1 converges much faster and easier to use than the other algorithms. YALL1 is a ready-made solver based on Alternating Direction Method (ADM). It can solve the l_1 -regularized linear inverse problems like (1.3) as well as the l_2 -regularized problems like (1.2). Besides the LS problems, YALL1 can also solve the least absolute deviations (LAD). YALL1 can add the non-negative constraints to the problems as well. In this thesis, it is only used to solve the LS problems, with l_1 -regularization in some transform space.

[39] demonstrates the theory of YALL1. YALL1 can solve the unconstrained basis pursuit denoising (QP) problem, which can be easily obtained by reformulating (1.3) when $\tau > 0$ and $\Psi^\dagger \Psi = \mathbf{I}$ (i.e., Ψ is full column rank), \dagger indicates pseudo inverse. Let \mathbf{z} denote the transformation of \mathbf{x} , that is, $\mathbf{z} = \Psi \mathbf{x}$, and let \mathbf{G} denote $\mathbf{A} \Psi^\dagger$. Then (1.3) can be reformulated as (2.1).

$$\min_{\mathbf{z}} \|\mathbf{z}\|_1 + \frac{1}{\tau} \|\mathbf{y} - \mathbf{G}\mathbf{z}\|_2^2. \quad (2.1)$$

After \mathbf{z} is calculated, \mathbf{x} can be obtained by $\mathbf{x} = \Psi^\dagger \mathbf{z}$. As for solving (2.1) by applying ADM to its dual problem, Algorithm 2 expresses the procedure of YALL1.

Algorithm 2 YALL1 for QP problem

- 1: **Given** $\mathbf{z}_0, \mathbf{u}_0, \beta > 0$ and $\gamma \in (0, (\sqrt{5} + 1)/2)$
 - 2: For $i = 0, 1, 2, \dots$ **iterate**:
 - 3: $\mathbf{v}_{i+1} = \mathcal{P}_{\mathbf{B}_1^\infty}(\mathbf{G}^H \mathbf{u}_i + \mathbf{z}_i / \beta)$
 - 4: $\mathbf{u}_{i+1} = [\beta \mathbf{G} \mathbf{v}_{i+1} - (\mathbf{G} \mathbf{z}_i - \mathbf{y})] / (0.5\tau + \beta)$
 - 5: $\mathbf{z}_{i+1} = \mathbf{z}_i - \gamma \beta (\mathbf{v}_{i+1} - \mathbf{G}^H \mathbf{u}_{i+1})$
 - 6: **Until** $\|\hat{\mathbf{z}}_i - \hat{\mathbf{z}}_{i-1}\|_2 / \|\hat{\mathbf{z}}_i\|_2 \leq \text{tolerance}$
-

Where H indicates conjugate transpose, \mathbf{B}_1^∞ is a set that $\mathbf{B}_1^\infty \triangleq \{\mathbf{s} : \|\mathbf{s}\|_\infty \leq 1\}$, $\mathcal{P}_{\mathbf{B}_1^\infty}(\cdot)$ computes the orthogonal projection (in Euclidean norm) onto \mathbf{B}_1^∞ .

2.3 The sparse bases

For solving (1.3), a good sparse basis Ψ can improve the performance of the reconstruction of the medical US image \mathbf{x} . This section will introduce several bases that are chosen as the candidates of the sparse bases and introduce a sparse dictionary learning

algorithm K-SVD. Furthermore, \mathbf{x} is a B-mode image that shows the scattering intensities of the US scatterers, so the characteristics of the medical US scatterers should be firstly analyzed, which helps to determine the sparse bases.

Section 2.3.1 discusses the model of medical US scatterers to help to select the bases used as sparse transformations. Then Section 2.3.2 introduces several transformations that will be experimented in next chapter. At last, K-SVD algorithm is introduced in Section 2.3.3, which will be simulated in Chapter 3.

2.3.1 The model of medical US phantoms

[18] and [16] describe a model of the medical US scattering intensity, which will be applied throughout this thesis. There are also some improved models such as [27] and [20], but they are less general. The phantom can be regarded as the sum of the strong scatterers and the other weaker scatterers. The strong scatterers are usually some tissue boundaries and bones. They have very strong scattering intensities due to an acoustical impedance contrast, and they are usually sparse in the spatial domain. Subtracting these strong scattering intensities, the rest of the phantom can be regarded as the product of a scattering strength map and a white Gaussian stochastic process. Figure 2.2 is a sketch of the phantom model that the strong scatterers plus the product of the scatter map and a stochastic process.

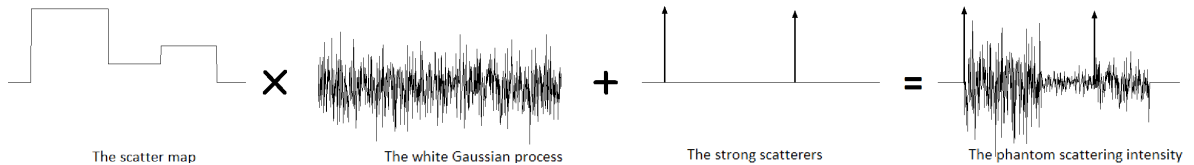


Figure 2.2: The sketch showing the constitution of the computer medical US phantom.

It is impossible to reconstruct the Gaussian signal but it helps us to see the scatter map. However, they are usually not sparse in spatial domain, and due to the stochastic nature of this signal, they are also not sparse in frequency domain. Therefore, some other transformations should be used. In this thesis, several kinds of the 2D wavelet transformations as well as the block 2D-DCT are chosen to analyze the sparsity of the medical US phantoms.

2.3.2 An introduction to several transformations

In this section, several transformations are introduced briefly which will be experimented as the sparse bases in next chapter.

2.3.2.1 The 2D-DWTs with the Haar, Daubechies and Meyer filters

The wavelet transforms can display a combination of the spatial and frequency characteristics, which are used as the sparse spaces in many cases. The filter bank shown in Figure 2.3 describes one dimension of the DWTs used in this thesis. The 2D-DWT

is an extensions of the 1D-DWT to the 2-dimensional case. This filter bank is only a single level of the 1D-DWTs. In Figure 2.3, $x[n]$ is the original signal, and the approximation and detail coefficients are the result of the DWT transformation. The approximation coefficients mainly contain the information in the low frequencies and detail coefficients mainly contain the information of the high frequencies. Since the lower frequency corresponds to the longer wavelength, the approximation coefficients can perform the decomposition once again, which is the next level of DWT. The symbol \downarrow denotes the downsampling, and the number 2 indicates that the signal is subsampled by 2. Because of the downsampling, if $x[n]$ has an even number of the signal samples, $x[n]$ will have the same number of the samples with all of the approximation and detail coefficients so that the DWT does not change the number of the samples.

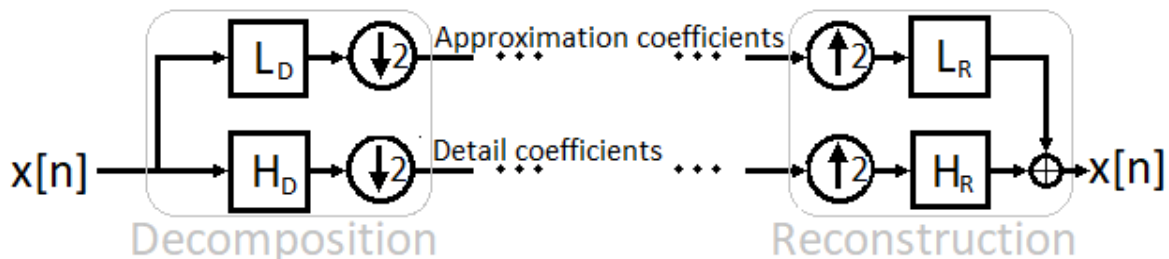


Figure 2.3: The filter bank describing the DWTs.

L_D and H_D denote a low-pass filter and a high-pass filter for the decomposition, and L_R and H_R denote the filters for the reconstruction. These filters must satisfy (2.2)[32].

$$\begin{cases} L_D(\omega)L_R(\omega) + H_D(\omega)H_R(\omega) = 2 \\ L_D(\omega - \pi)L_R(\omega) + H_D(\omega - \pi)H_R(\omega) = 0 \end{cases} \quad (2.2)$$

Therefore, the DWTs varies with the different filter banks. There are some commonly used filter banks for the DWT, such as the Haar filter bank, the Daubechies filter banks and the Meyer filter filter bank.

For example, the sequence $[1 \ 1]/\sqrt{2}$ expresses the low-pass filter L_D of the Haar filter bank in 1D, and $[1 \ -1]/\sqrt{2}$ expresses its high-pass filter H_D . The filter length is only 2, so the edge of its passband is gradual. The Haar DWT is often a sparse representation of the piece-wise constant signals[31].

The Daubechies DWTs are the extensions of the Haar DWT with longer filters. The piece-wise linear signals are usually sparse in some Daubechies DWT[31].

As for the Meyer DWT, [36] gives the formulas of its filters. The frequency bands of its filters have sharp edges. So the bandlimited signals can be sparse in the Meyer DWT. But, according to the uncertainty principle of Fourier transform, the filter needs to be long enough in spatial domain to have the sharp edge of the frequency band, so the Meyer DWT are not a good sparse representation for the sharp edges or thin lines in spatial domain. The DWT only decompose the approximation coefficients. However, it can work better if some detail coefficients are also decomposed, which becomes the

wavelet packet transform[2].

2.3.2.2 The wave atom transform

The wavelet transforms do not make sufficient use of the 2D-image geometrical characteristics, so more multiscale geometric transforms have been proposed, such as the Ridgelet, curvelet[14], contourlet[10] and wave atom[9] transforms. The wave atom decomposition is a good sparse representation for the oscillatory patterns. [22] find that the wave atom is a good sparse transform for the raw RF data. Since the reconstructed US images are usually oscillatory, the wave atom could also be a sparse space for the US image.

2.3.2.3 The 2D-DCT and block 2D-DCT

The 2D-DCT is an extension of the 1D-DCT, that is, the 1D-DCT is performed in each dimensions one after another. It is related to the Fourier transform that it shows the frequency information as well, but the number of DCT coefficients is about twice the number of DFT coefficients. Moreover, if the original signal is real, its DCT is also real.

The computations of one kind of DCT can be described as follows. Suppose a real finite digital signal $s[n]$, $0 \leq n \leq N - 1$. Then, it is extended to a symmetric signal $s[|n|]$, $1 - N \leq n \leq N - 1$. The DFT of the real even signal $s[|n|]$ is also real even, which is denoted as $S[k]$, $1 - N \leq k \leq N - 1$. And then, the whole $S[k]$ can be recovered just from the $S[k]$ at $k = 0, 1, \dots, N - 1$, which are about half of the entire $S[k]$. So the $s[n]$ can be reconstructed from the $S[k]$ at $k = 0, 1, \dots, N - 1$, which is also known as the DCT of $s[n]$. According to DFT is an orthogonal transform, it can be derived that DCT is also.

As for the block 2D-DCT, it is widely used by the JPEG algorithm[38]. First, the image is divided into many blocks. Then, the 2D-DCT is computed for each block individually. The block 2D-DCT is a localized frequency representation. And the block size need to be chosen. Larger block size means the sparsity of the block 2D-DCT is closer to that of the frequency domain, and the smaller block size means its sparsity is closer to the spacial domain.

2.3.3 The K-SVD sparse dictionary learning algorithm

If there are a lot of ultrasound image samples that are reconstructed very well, they can be used as the training data to find the sparse space of the ultrasound image. The optimization problem for training the sparse dictionary can be expressed by (2.3).

$$\min_{\mathbf{D}, \mathbf{\Gamma}} \{ \|\Theta - \mathbf{D}\mathbf{\Gamma}\|_F^2 \} \quad \text{s.t.} \quad \forall i, \|\gamma_i\|_0 \leq T_0. \quad (2.3)$$

$\Theta \in \mathbb{R}^{N' \times M'}$ is the set of the training samples. Each of its columns is one training sample with a data length of N' . M' is the number of the training samples and should be large enough to make Θ adequately representative. $\mathbf{D} \in \mathbb{R}^{N' \times K'}$ is the sparse dictionary matrix to be computed. K' is the length of the dictionary and usually equal to or

larger than N' . $\mathbf{\Gamma} \in \mathbb{R}^{K' \times M'}$ contains the corresponding representation coefficients. $\|\cdot\|_F$ indicates the Frobenius norm. When applied to a matrix, the Frobenius norm calculates the square root of the sum of the squares of the singular values of the matrix, which is equal to the root of the sum of the squares of each element in the matrix. γ_i is the i th column of $\mathbf{\Gamma}$, which contains the corresponding coefficients when the i th training sample in $\mathbf{\Theta}$ is represented with the dictionary \mathbf{D} . $\|\cdot\|_0$ denotes the l_0 -norm, which computes the number of the non-zero elements in a vector. T_0 is a parameter constraining the number of non-zero representation coefficients of each training sample. So the constraint is that the number of the dictionary coefficients for each training sample cannot exceed T_0 .

To solve (2.3), there are many kinds of the sparse dictionary learning algorithms, such as MOD[13], K-SVD[1], etc. However, because (2.3) is a non-convex and NP-hard problem[33], these algorithms cannot guarantee a globally optimal solution to (2.3). In this thesis, the K-SVD algorithm is chosen to train the the sparse dictionary, since it is widely used for the sparse dictionary learning and there are many off-the-shelf K-SVD programs on the internet. In this thesis, we use the K-SVD decribed in [29]. For (2.3), K-SVD alternately iterates the dictionary \mathbf{D} and the representation coefficients $\mathbf{\Gamma}$. For each iteration, $\mathbf{\Gamma}$ is calculated from the $\mathbf{\Theta}$ and updated \mathbf{D} and constrained to have no more than T_0 non-zero elements in each column. Matching pursuit (MP) is always used to compute it. For updating \mathbf{D} , each of its columns is iterated sequentially. And the principle of the calculations is that each column should fit the current residuals of $\mathbf{\Theta}$ as much as possible. To achieve this, the SVD can be performed on the current residuals of $\mathbf{\Theta}$ and the singular vector corresponding to the largest singular value is used to update the column of \mathbf{D} . In addition, to keep the sparsity of $\mathbf{\Gamma}$, only the residuals that correspond to non-zero representation coefficients of the column participate in the calculation.

Assume $\gamma_{T,k'}$ indicates the k' th row of $\mathbf{\Gamma}$, then the K-SVD algorithm flow is described as Algorithm 3.

Algorithm 3 K-SVD

- 1: **Given:** training data set $\mathbf{\Theta}$, sparsity constraint parameter T_0 , length of dictionary K' , initial dictionary matrix $\mathbf{D}^{(0)} \in \mathbb{R}^{N' \times K'}$
 - 2: For $i=0, 1, 2, \dots$ **iterate:**
 - 3: • Solving (2.3) by MP to get the representation coefficient matrix $\mathbf{\Gamma}^{(i)}$
 - 4: • For $k'=1, 2, \dots, K'$ **iterate:**
 - 5: - Compute $\mathbf{\Theta}$'s residuals $\mathbf{\Xi}_{k'}^{(i)}$ without $\mathbf{D}^{(i)}$'s k' th column $\mathbf{d}_{k'}^{(i)}$ by

$$\mathbf{\Xi}_{k'}^{(i)} = \mathbf{\Theta} - \sum_{j \neq k'} \mathbf{d}_j^{(i)} \gamma_{T,j}^{(i)} = \mathbf{\Theta} - \mathbf{D}^{(i)} \mathbf{\Gamma}^{(i)} + \mathbf{d}_{k'}^{(i)} \gamma_{T,k'}^{(i)}$$
 - 6: - Selecting $\mathbf{\Theta}$'s columns θ_j satisfying $j \in \{j \in N^+ | 1 \leq j \leq M', [\gamma_{T,k'}^{(i)}]_j \neq 0\}$, then $\mathbf{\Theta}_{R,k'}^{(i)}$ consists of these columns.
 - 7: - Performing SVD as $\mathbf{\Theta}_{R,k'}^{(i)} = \mathbf{U} \mathbf{S} \mathbf{V}^T$. The updated column $\mathbf{d}_{k'}^{(i+1)}$ is \mathbf{U} 's column corresponding to the largest singular value. The non-zero coefficients in $\gamma_{T,k'}^{(i)}$ are updated as the multiplication of the largest singular value and its corresponding column in \mathbf{V} .
-

3

Simulation results and analysis

In this chapter, the transformations introduced in Chapter 2 are performed on several phantom images and their sparsity is analyzed, and the performance of the K-SVD on the US images is analyzed. In Section 3.1, several transforms are performed on the scattering intensity linear interpolation images of a fetus phantom and a kidney phantom to analyze their sparsity. In Section 3.2, some transforms are performed on a simulated fetus phantom MF image and a real carotid MF image. Section 3.3 performs the K-SVD on some beamformed carotid US images from the real people. Section 3.4 shows the reconstructions from the simulated US measurements and analyzes the effects of the selected sparse spaces on the reconstruction image quality.

3.1 The sparse space of the linear interpolation images of the phantom US scattering intensity

On the Field II[17][19] website, there are several computer phantoms typically used for simulating ultrasound imaging. The fetus and kidney computer phantoms are used here to analyze the sparsity level of the linear interpolation images of the medical US scattering intensity. Some transformations, such as the 2D-DCT and the 2D-DWTs, are performed on these two US scattering intensity images to compare the sparsity of these transformations. At the end of this section, the sparsity of these two scattering intensity images is analyzed.

As usual, what is shown to the operator is the log-compression of the absolute values of the ultrasound images, because taking logarithms will magnify the dim part of the image. Before converting into the logarithm or decibels, the absolute values of the image are usually normalized. Suppose matrix \mathbf{X} represents the linear-scale image. Then, the magnitudes of the image \mathbf{X} are normalized and converted into decibels as (3.1), and the image \mathbf{X}' is usually displayed in certain decibel range to the operator. $[\cdot]_{ij}$ means the matrix element at the i th row and the j th column, and $\|\cdot\|_{max}$ indicates the max norm of a matrix (i.e., $\|\mathbf{X}\|_{max} = \max_{ij}[\mathbf{X}]_{ij}$).

$$[\mathbf{X}']_{ij} = 20 \log_{10}(|[\mathbf{X}]_{ij}|/|\mathbf{X}|_{max}). \quad (3.1)$$

3.1.1 The fetus phantom US scattering intensity linear interpolation image

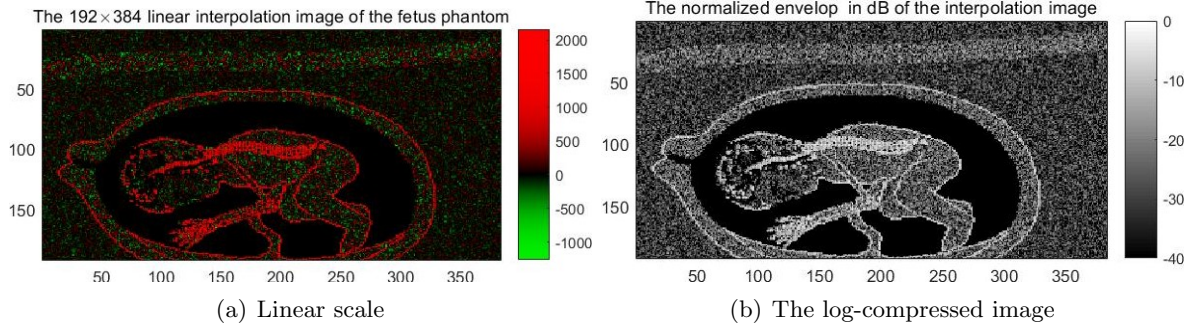


Figure 3.1: The linear interpolation image of the fetus phantom US scattering intensity.

In this part, the sparsity of many transforms for fetus phantom interpolation image are compared, and the reconstructions from their maximal 15% coefficients in the transform domain are shown respectively to compare their reconstruction performance for the interpolation image of the fetus phantom US scattering intensity.

Figure 3.1 shows the 192×384 linear interpolation image of the fetus phantom US scattering intensity in linear scale and its log-compressed image from -40dB to 0dB. Here 20dB is equal to 10 times.

To compare the sparsity of the different orthonormal transforms, the curves are drawn between the percentage of the number of the maximum coefficients and the normalized RMSE. The horizontal axis of the curve is the percentage of the number of the maximum coefficients used for the reconstruction, i.e., the ratio between the number of the maximum coefficients used for the reconstruction and the total number of the coefficients. The vertical axis of the curve is the normalized RMSE between the reconstruction and original image, which is formulated as (3.2).

$$\epsilon = \|\hat{\mathbf{x}} - \mathbf{x}\|_2 / \|\mathbf{x}\|_2. \quad (3.2)$$

Where ϵ is the normalized RMSE and \mathbf{x} is the original image vector and $\hat{\mathbf{x}}$ is the reconstructed image vector.

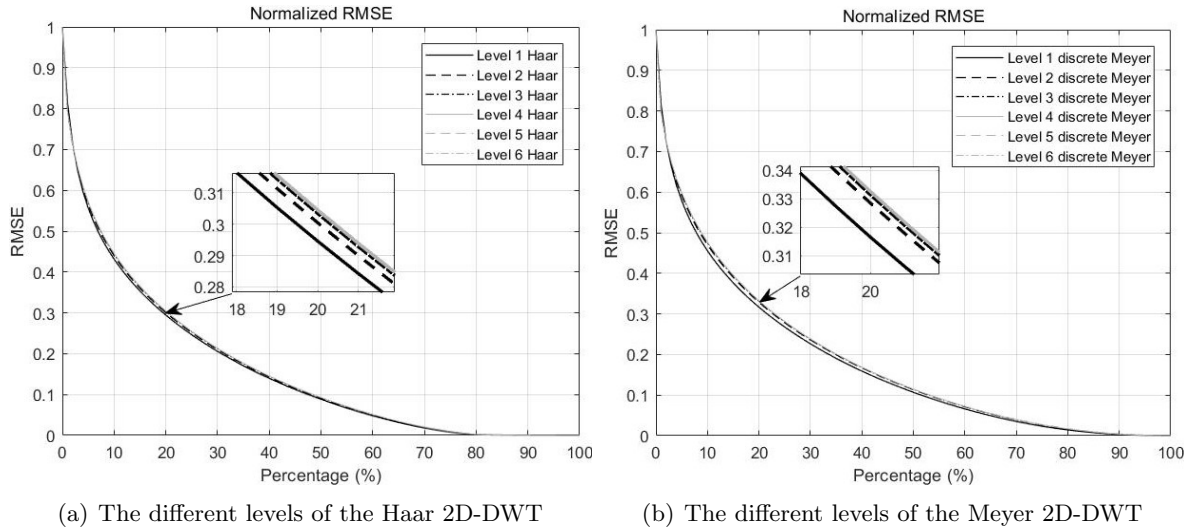


Figure 3.2: Comparison among the different levels of the Haar 2D-DWT and the Meyer 2D-DWT.

In general, the smaller the under region of the curve is, the sparser the transform is. Figure 3.2(a) shows the curves of the Haar 2D-DWT from level 1 to level 6 respectively. The level 1 Haar DWT is sparser than the others, but the difference is little. Figure 3.2(b) shows the curves of the discrete Meyer 2D-DWT from level 1 to level 6 respectively. The level 1 discrete Meyer 2D-DWT is sparser than the others, but the difference is little as well. The other DWTs, such as the Daubechies, are used, and the level 1 is always the best. All the DWTs are in periodical mode, so that the total number of the coefficients is always equivalent to the number of the image pixels.

Figure 3.3(a) shows the curves of the level 1 2D-DWTs with the filter banks from Daubechies1 to Daubechies6 respectively. The Daubechies1 2D-DWT, also known as the Haar 2D-DWT, is sparser than the others. To combine the spatial characteristics and frequency characteristics, another transformation is implemented in which the image is divided into a number of small blocks, each of which performs 2D-DCT separately. Figure 3.3(b) shows the curves of the block 2D-DCT with the block size 1×2 , 2×1 , 2×2 , 4×4 , 8×8 and 16×16 respectively. The block 2D-DCT with block size 1×2 is sparser than the others. The smaller the blocks are, the more the spatial characteristics are emphasized. Since the block size 1×1 means that the block 2D-DCT is equivalent to the spatial domain, the block size 1×1 will not be considered here.

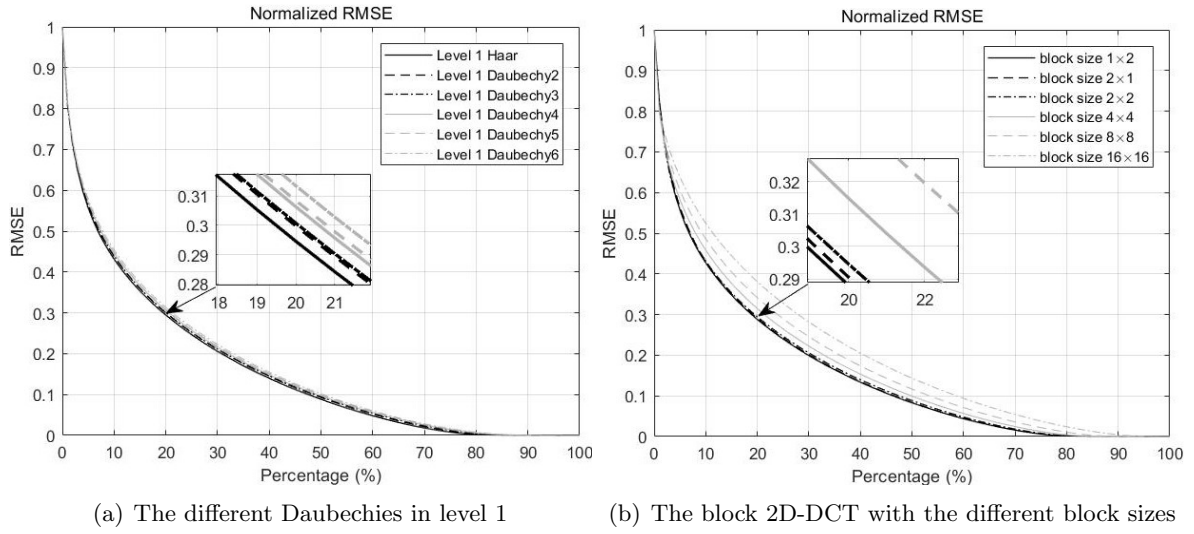


Figure 3.3: Comparison among the different Daubechies in level 1 and comparison among the block 2D-DCT with the different block sizes.

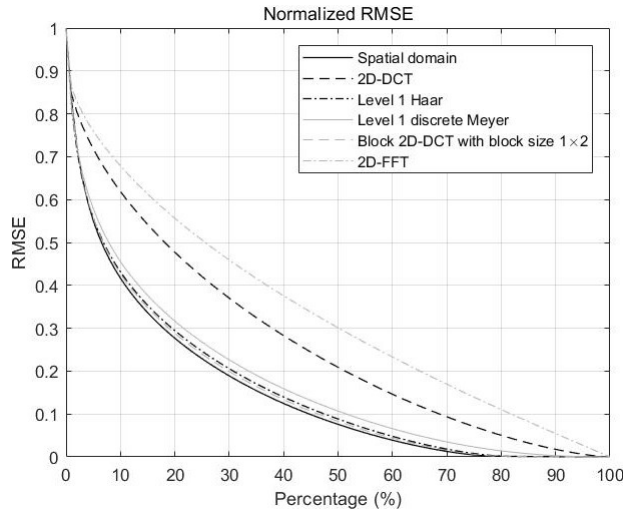


Figure 3.4: Comparison among the spatial domain, the 2D-DCT, the Haar 2D-DWT, the discrete Meyer 2D-DWT, block 2D-DCT and 2D-FFT.

Figure 3.4 shows the curves of the spatial domain, 2D-DCT, 2D-FFT and the sparsest transformations in Figures 3.2(a), 3.2(b), 3.3(a) and 3.3(b) respectively. The sparsest is the spatial domain. That is, as for the fetus phantom interpolation image, the original image is sparser than the other transformations. From Figure 3.1(a), we can also see that the spatial domain looks sparse. Because of the multiplicative white Gaussian process described in Section 2.1, the scattering intensity interpolation image is hard to be sparser in other transform space.

Figure 3.5 shows the normalized spectrum from -40dB to 0dB of the 2D-DCT and the 2D-FFT of the fetus phantom interpolation image.

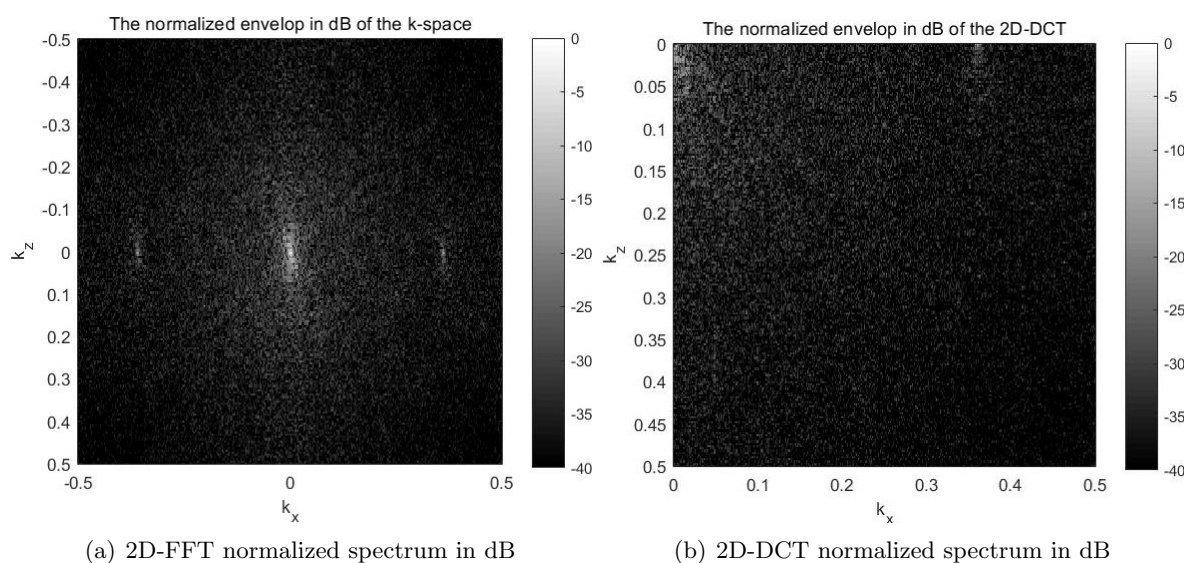


Figure 3.5: The 2D-FFT and 2D-DCT normalized spectrum in dB of the fetus phantom interpolation image.

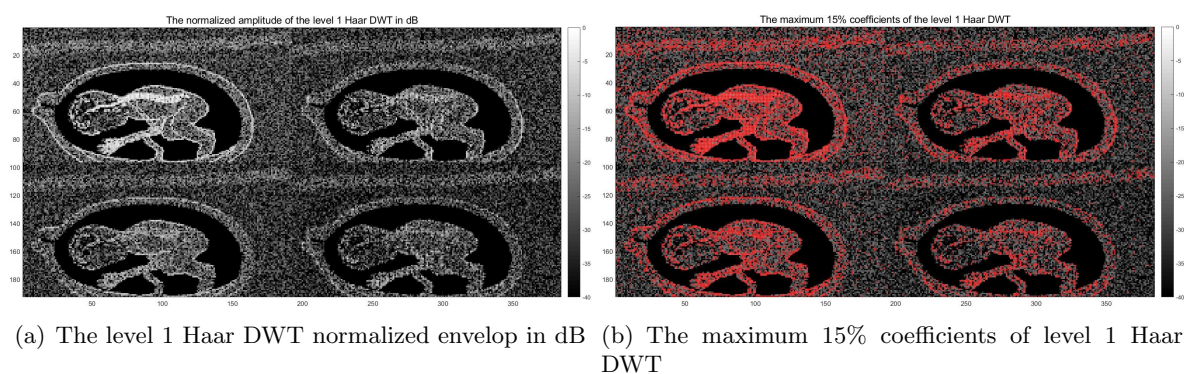


Figure 3.6: The level 1 Haar DWT of the fetus phantom interpolation image, and its maximum 15% coefficients.

Figure 3.6 shows the level 1 Haar 2D-DWT normalized spectrum from -40dB to 0dB of the fetus phantom interpolation image and the position of the maximum 15% coefficients in this spectrum.

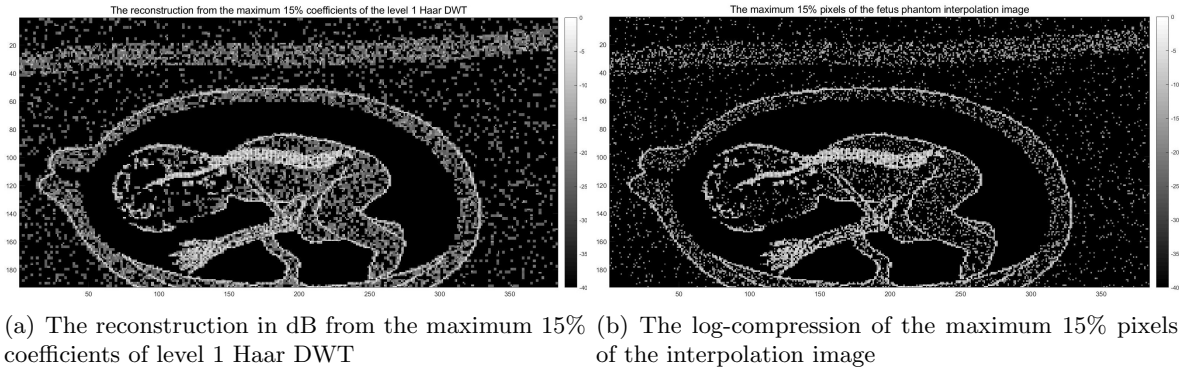


Figure 3.7: The normalized absolute values from -40dB to 0dB of: (a) the reconstruction from the maximum 15% level 1 Haar DWT coefficients; (b) the maximum 15% pixels of the fetus phantom interpolation image.

Figure 3.7(a) shows the log-compression of the reconstruction from the maximum 15% coefficients of the level 1 Haar 2D-DWT shown in Figure 3.6(b). Figure 3.7(b) shows the maximum 15% pixels in the fetus phantom interpolation image. In both images, many details of the true image are distorted, such as the details in the face.

Figures 3.8(a) and 3.8(b) indicate the maximum 15% 2D-FFT coefficients and 2D-DCT coefficients of the fetus phantom interpolation image.

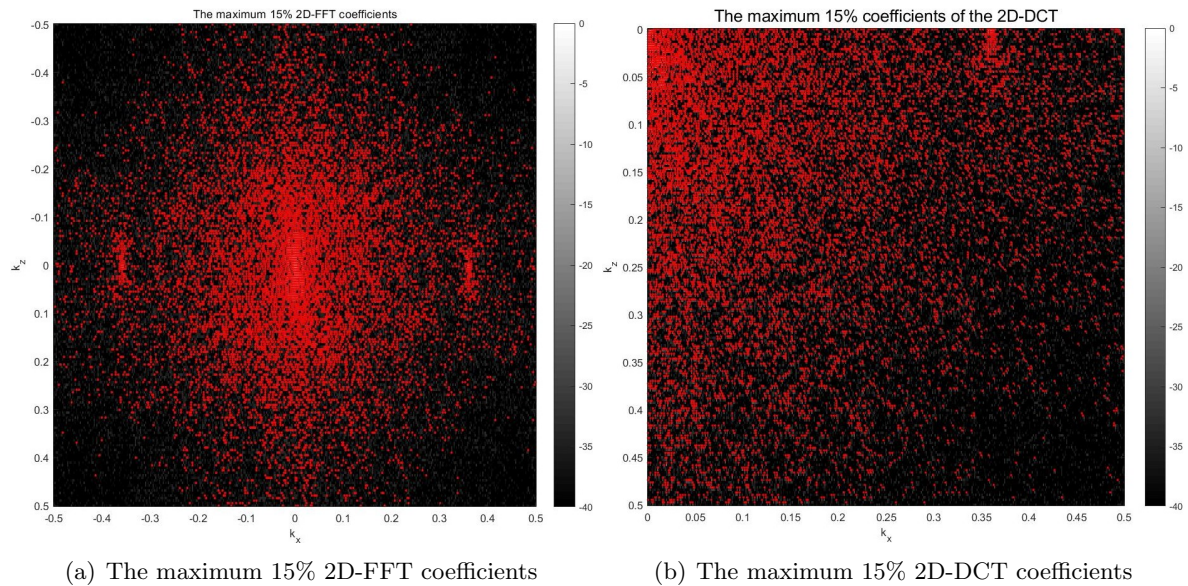


Figure 3.8: The maximum 15% 2D-FFT and 2D-DCT coefficients of the fetus phantom interpolation image.

Figures 3.9(a) and 3.9(b) show the normalized absolute values from -40dB to 0dB of the reconstructions from the 2D-FFT and 2D-DCT coefficients shown in Figures 3.8(a) and 3.8(b) respectively. The reconstructions are distorted.

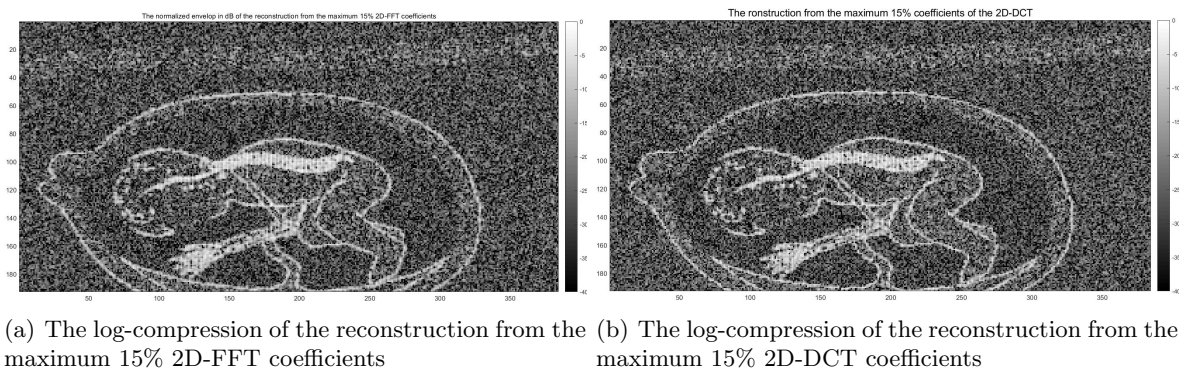


Figure 3.9: The log-compression from -40dB to 0dB of the reconstruction from the maximum 15% 2D-DCT coefficients and 2D-FFT coefficients respectively.

3.1.2 The kidney phantom linear interpolation image

In this paragraph, the simulations are performed on the kidney phantom interpolation image.

Figure 3.10 shows the 512×512 linear interpolation image of the kidney phantom scattering intensity in linear scale and its normalized absolute values from -40dB to 0dB.

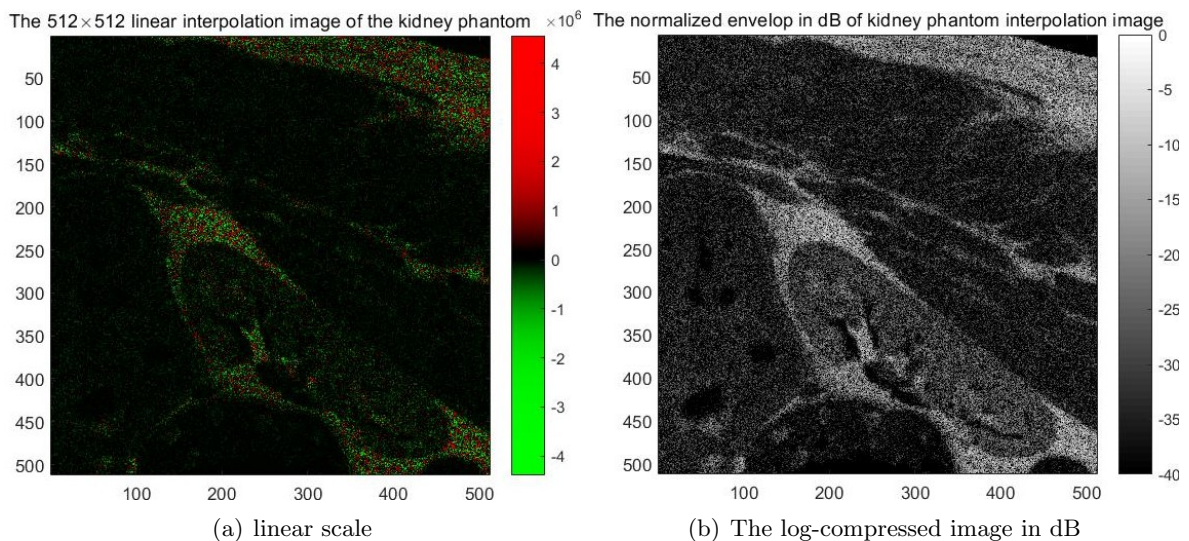


Figure 3.10: The linear interpolation image of the kidney phantom scattering intensity.

Figure 3.11(a) shows the curves of the Daubechies2 DWT from level 1 to level 6 respectively. The level 1 Daubechies2 DWT is sparser than the others. Figure 3.11(b) shows the curves of the discrete Meyer DWT from level 1 to level 6 respectively. The level 1 discrete Meyer DWT is sparser than the others.

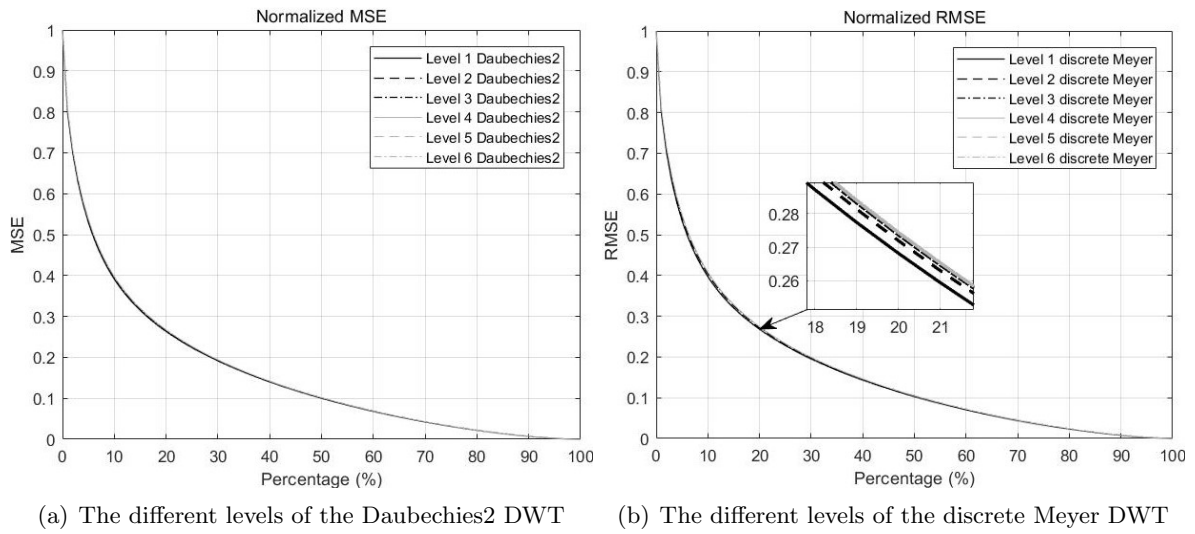


Figure 3.11: Comparison among the different levels of the Daubechies2 DWT and the discrete Meyer DWT.

Figure 3.12(a) shows the curves of the level 1 DWTs with the filters from Daubechies 1 to Daubechies 6 respectively. The Daubechies2 DWT is sparser than the others. Figure 3.12(b) shows the curves of the block 2D-DCT with some different block sizes. The block 2D-DCT with block size 1×2 is sparser than the others.

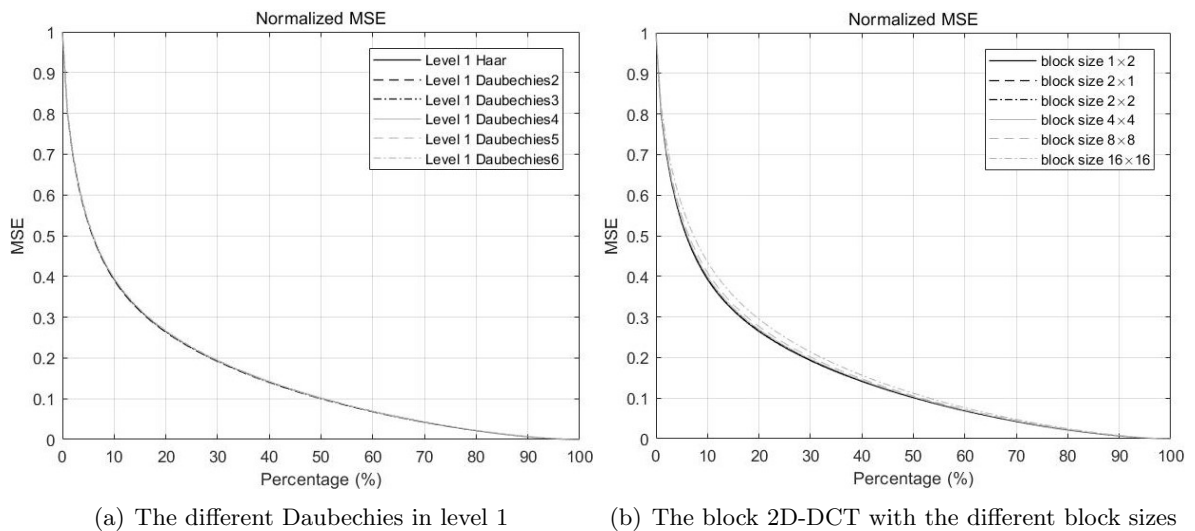
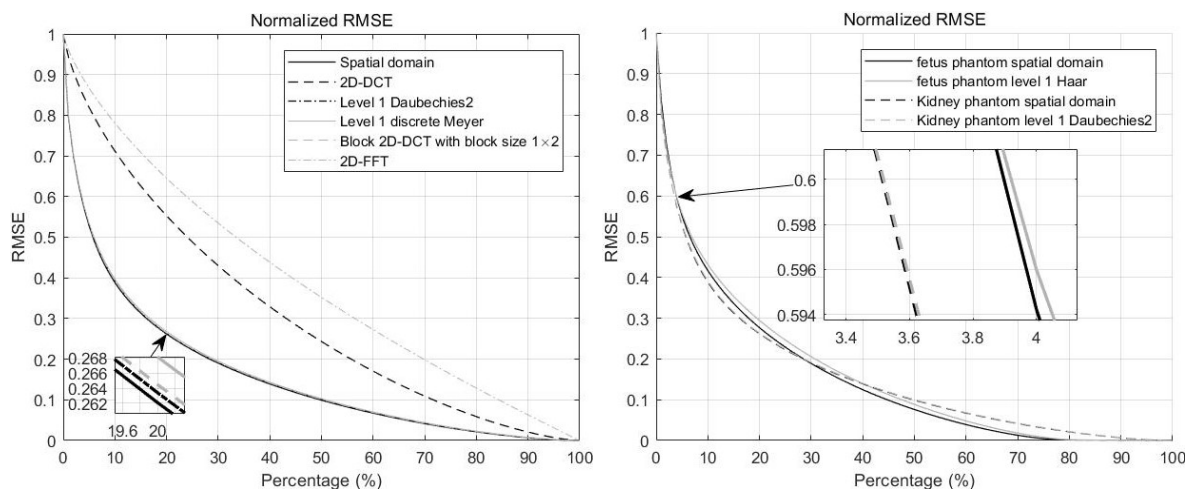


Figure 3.12: Comparison among the different Daubechies in level 1 and comparison among the block 2D-DCT with the different block sizes.

Figure 3.13(a) shows the curves of the spatial domain, 2D-DCT, 2D-FFT and the sparsest transformations in Figures 3.11(a), 3.11(b), 3.12(a) and 3.12(b) respectively. For the kidney phantom, the original interpolation image is sparser than the other

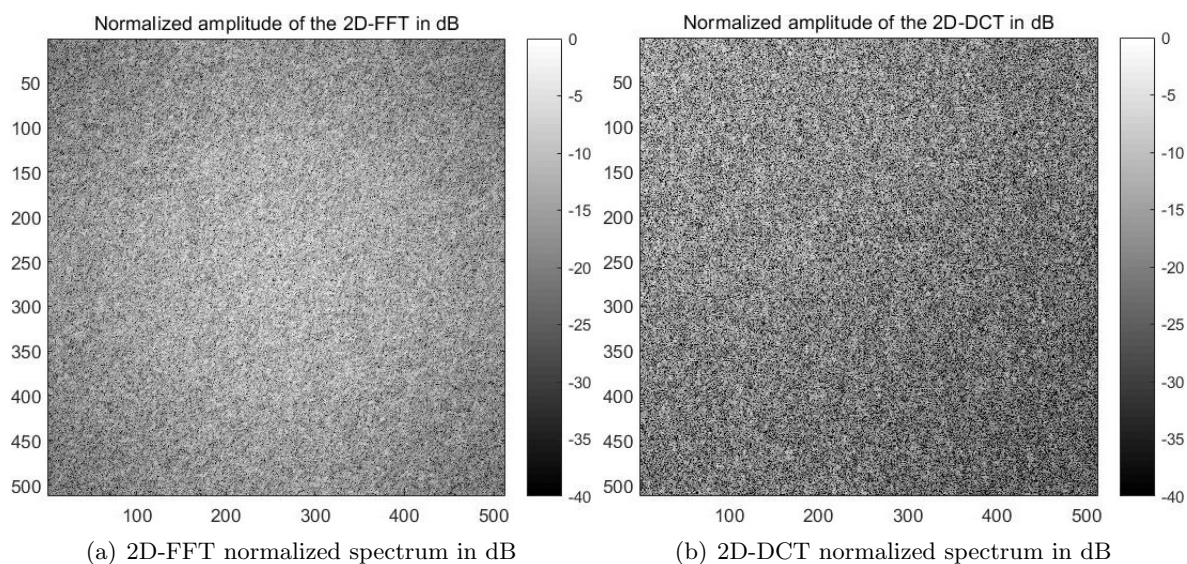
transformations as well. Figure 3.13(b) shows the comparison of the sparsity between the fetus phantom and the kidney phantom. Their sparsity is different but similar.



(a) The different transforms of the kidney phantom (b) The spatial domain and the 2D-DWT of the fetus phantom and the kidney phantom

Figure 3.13: Comparison of the sparsity among the spatial domain, the 2D-DCT, the Haar DWT, the discrete Meyer DWT, block 2D-DCT and 2D-FFT of the kidney phantom and comparison of the sparsity between the fetus phantom and the kidney phantom.

Figure 3.14 shows the normalized absolute values from -40dB to 0dB of the 2D-DCT and the 2D-FFT of the kidney phantom interpolation image.



(a) 2D-FFT normalized spectrum in dB (b) 2D-DCT normalized spectrum in dB

Figure 3.14: The 2D-FFT and 2D-DCT normalized spectrum in dB of the kidney phantom interpolation image.

Figure 3.15 shows the level 1 Daubechies2 DWT spectrum of the kidney phantom interpolation image and the position of the maximum 15% coefficients in the spectrum.

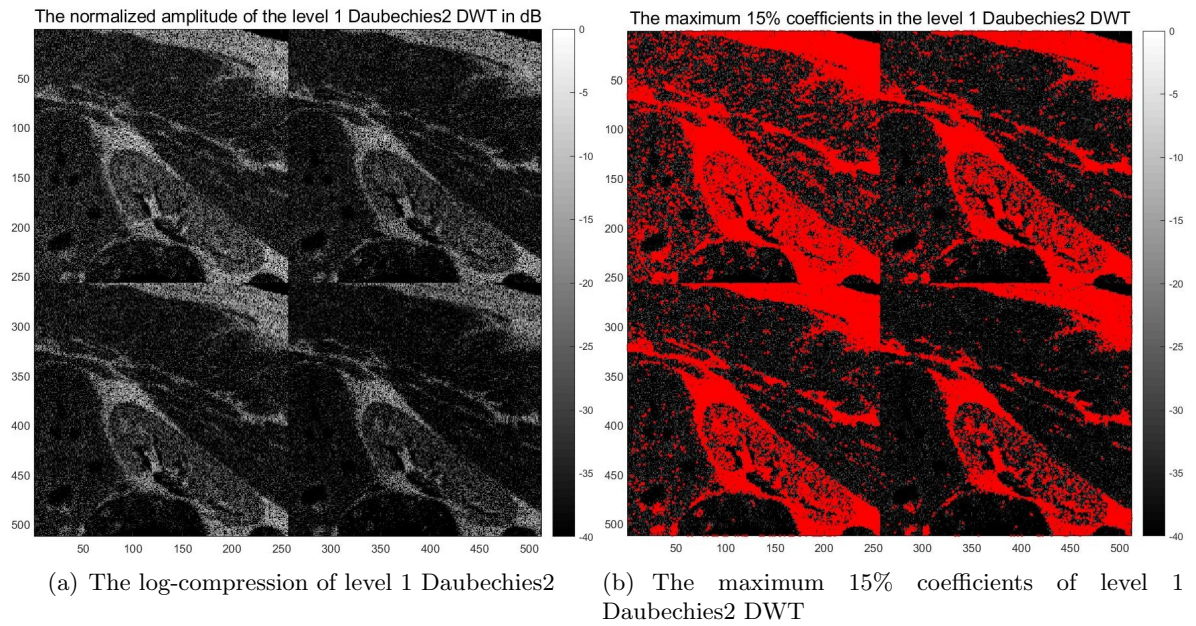


Figure 3.15: The level 1 Daubechies2 DWT of the kidney phantom interpolation image, and its maximum 15% coefficients.

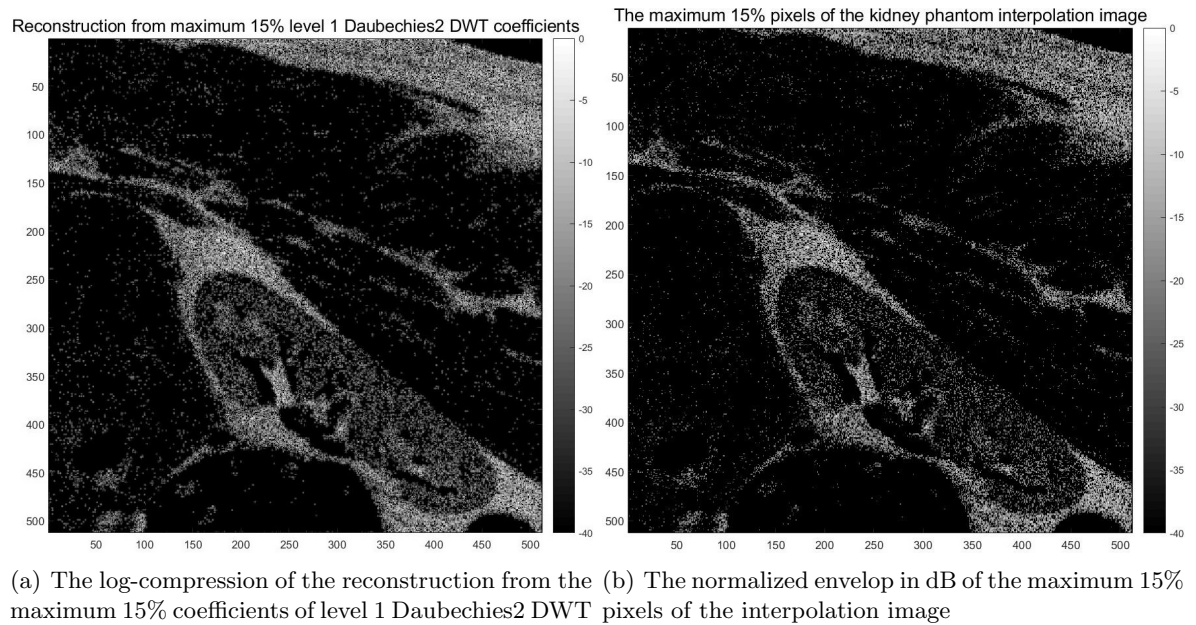


Figure 3.16: The normalized absolute values in dB of the reconstruction from the maximum 15% coefficients in level 1 Daubechies2 DWT, and the maximum 15% pixels of the kidney phantom interpolation image.

Figure 3.16(a) shows the normalized absolute values from -40dB to 0dB of the reconstruction from the maximum 15% coefficients of the level 1 Daubechies2 2D-DWT shown in Figure 3.15(b). Figure 3.16(b) shows the maximum 15% pixels in dB of the kidney phantom interpolation image.

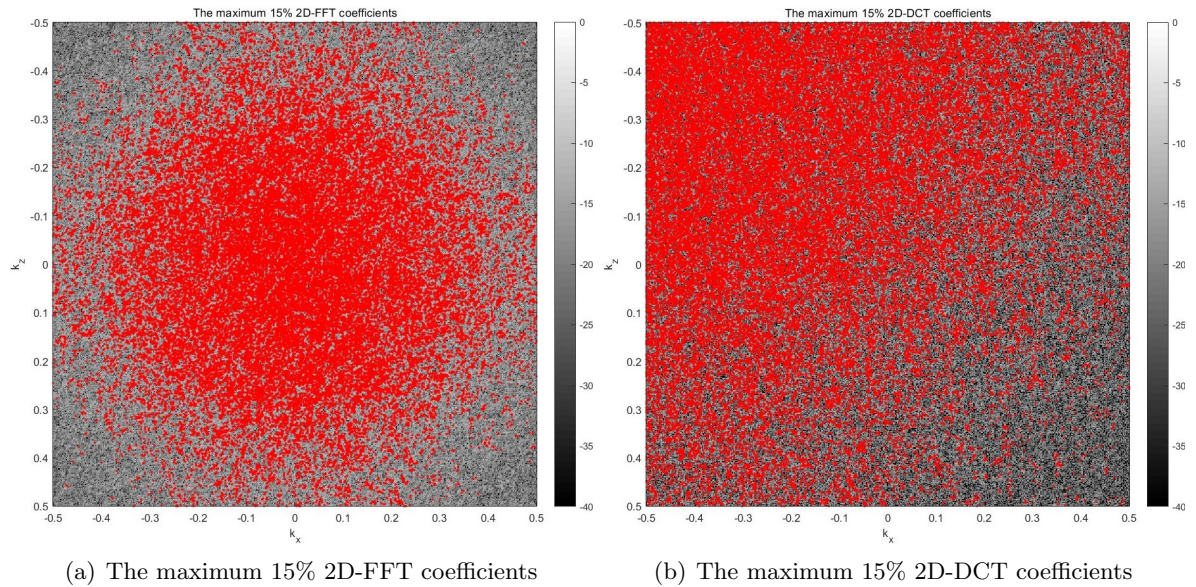


Figure 3.17: The maximum 15% 2D-FFT and 2D-DCT coefficients of the kidney phantom interpolation image.

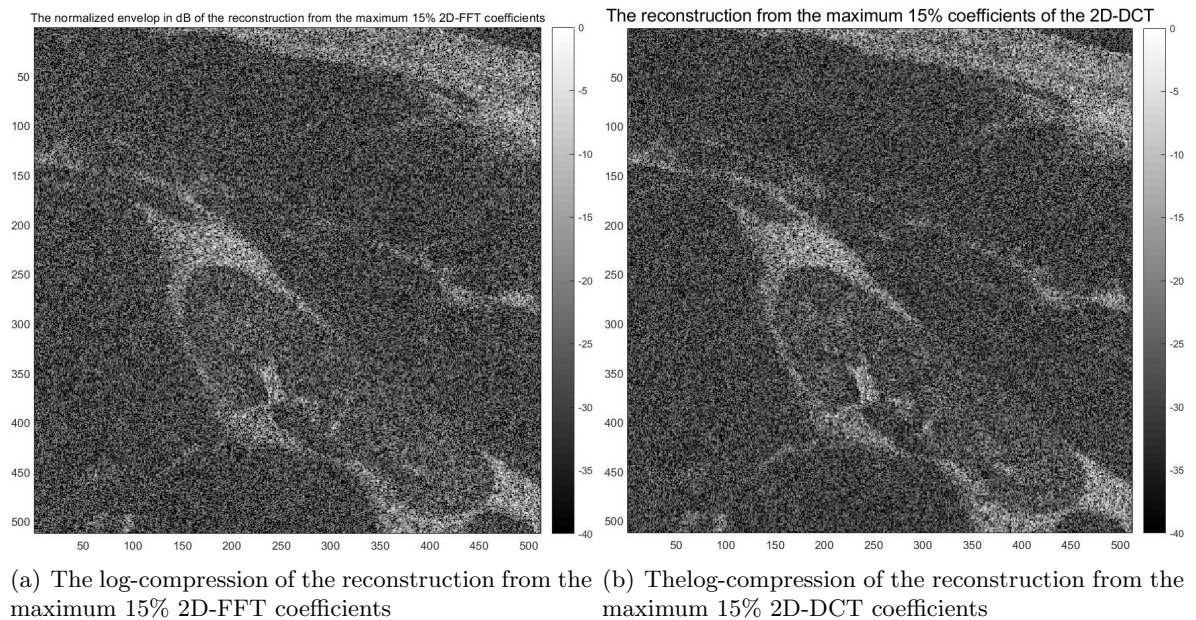


Figure 3.18: The normalized absolute values in dB of the reconstruction from the maximum 15% 2D-FFT and 2D-DCT coefficients.

Figure 3.17 indicates the maximum 15% 2D-FFT and 2D-DCT coefficients of the kidney phantom interpolation image.

Figure 3.18 shows the normalized absolute values from -40dB to 0dB of the reconstructions from the maximum 15% 2D-FFT and 2D-DCT coefficients.

3.1.3 Analysis

As for the linear interpolation images of the fetus and the kidney phantom scattering intensity, the spatial domain is sparser than the other transforms, but the spatial sparsity is still insufficient. Therefore, the sparse space of the ultrasound reconstructed images is researched.

3.2 The sparse space of the ultrasound reconstruction images

The scattering intensity interpolation images are not sparse enough in the common transforms. They are very impulsive. That is, they are not smooth. As a result, they are hard to compress. We can hardly reconstruct them because of this impulsive structure. So it is more realistic to focus on beamformed images. Moreover, in this report, the aim is to improve the reconstruction performance with transmitting 1 PW (plane wave). Therefore, the ultrasound images reconstructed with multiple PWs by the conventional beamforming techniques can be regarded as the true image to research the sparse space. The fetus phantom MF (matched filter) image and carotid MF image are simulated. The fetus image is a computer simulation, and the carotid image is the experimental data.

3.2.1 The fetus phantom 21-PW MF image

This simulation is done in MATLAB. To be convenient, the imaging domain is set as Figure 3.19. The imaging domain is approximately a $17.53\text{mm} \times 8.77\text{mm}$ rectangular area. The size of the fetus phantom shrinks about 5.48 times to fit the imaging domain.

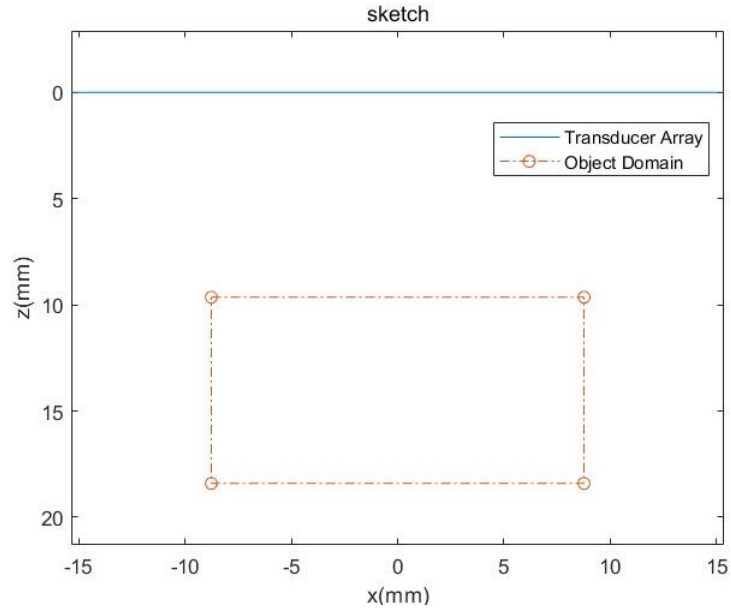


Figure 3.19: The imaging domain.

The parameters are listed in Table 3.1.

sampling frequency	$f_s = 50MHz$
pulse wave frequency	$f_0 = 5MHz$
ultrasound wave speed	$c_0 = 1540m/s$
wavelength	$\lambda = c_0/f_0 = 0.308mm$
the width of array element	$0.2mm$
the height of array element	$2mm$
kerf	$0.04mm$
the number of array elements	128
the length of array	$30.68mm$
imaging domain	$ x < 8.77mm, 9.64mm < z < 18.41mm$

Table 3.1: Parameters of the fetus phantom MF image

In this case, the US pulse is a 2-circle 5MHz sine pulse with Hanning window, the time response of which is formulated as equation (3.3).

$$p(t) = (0.5 - 0.5 \cos \pi f_0 t) \cdot \sin 2\pi f_0 t, \quad t \in [0, 2/f_0]. \quad (3.3)$$

Figure 3.20 shows the time response and the normalized frequency spectrum of the US pulse. Since the frequency domain of the real signals is conjugate symmetric with respect to the origin, only the spectrum of the non-negative frequencies is shown.

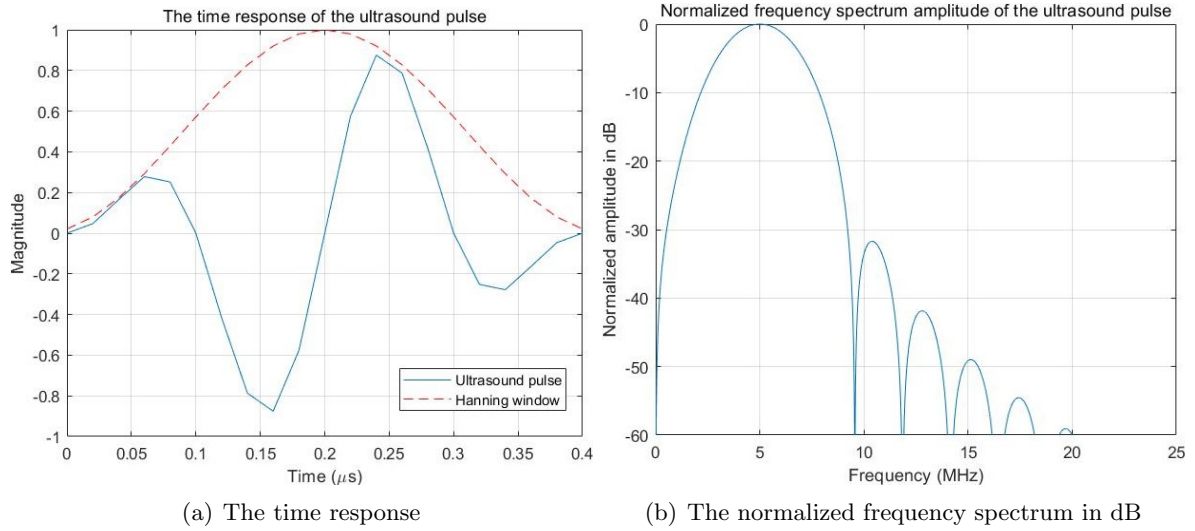


Figure 3.20: The time response and the normalized frequency spectrum of the US pulse.

Figure 3.21 shows the normalized envelopes from -40 to 0dB of the 3-PW and 6-PW MF images.

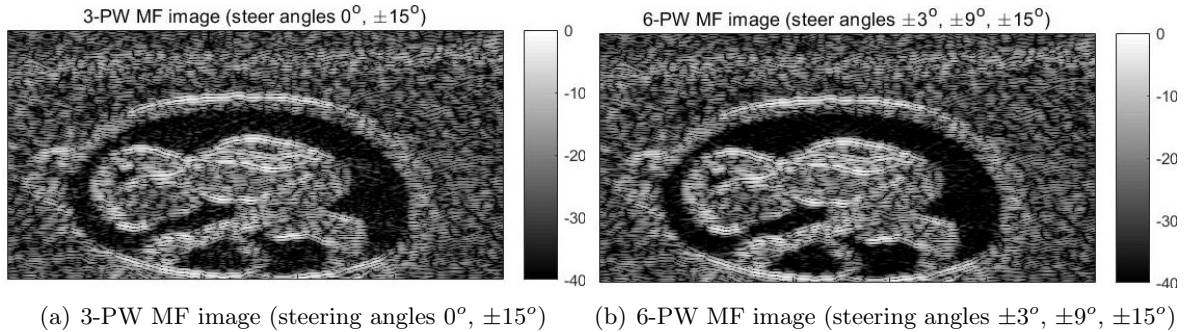


Figure 3.21: The normalized envelopes in dB of the noiseless fetus phantom 3-PW and 6-PW MF images.

The 256×512 noiseless 21-PW MF image is shown as Figure 3.22, and Figure 3.23 shows the normalized envelop from -40dB to 0dB of its z-directional Hilbert transform. There are nearly 9 pixels per wavelength. The steering angles of the 21 PWs are $0^\circ, \pm 1.5^\circ, \pm 3^\circ, \dots, \pm 15^\circ$. Compared with the 3-PW and 6-PW images in Figure 3.21, the 21-PW image is not improved much. It is concluded that more PWs with the different steering angles between $\pm 15^\circ$ will not significantly improve the image quality. So here the 21-PW image is regarded as the true image.

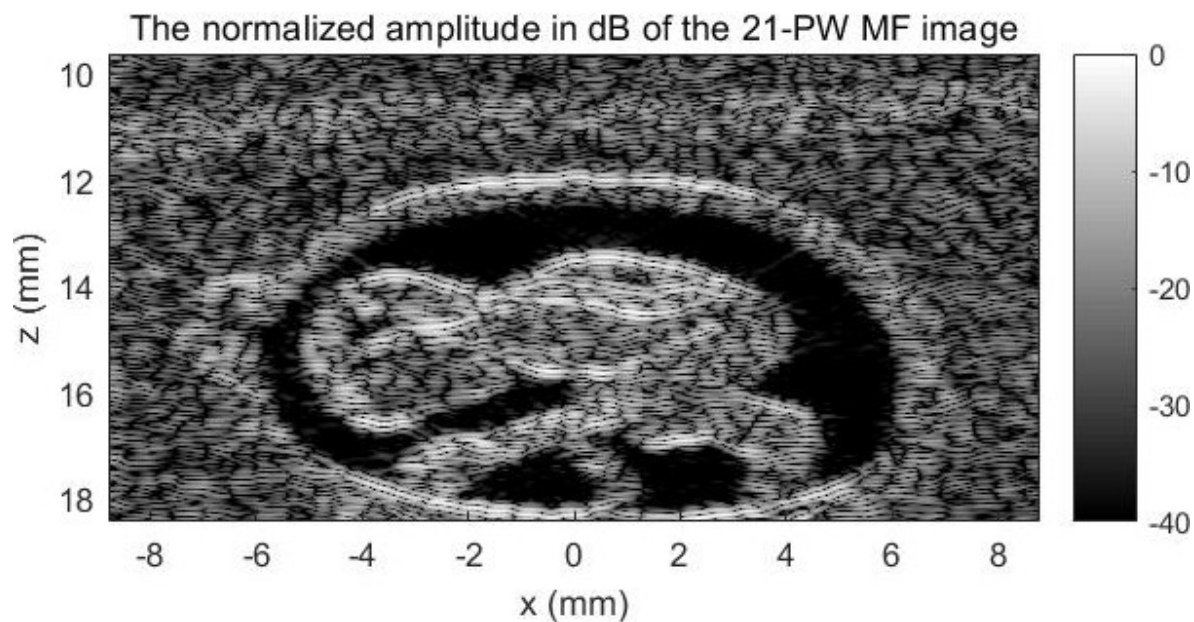


Figure 3.22: The normalized absolute values in dB of the noiseless fetus phantom 21-PW MF image.

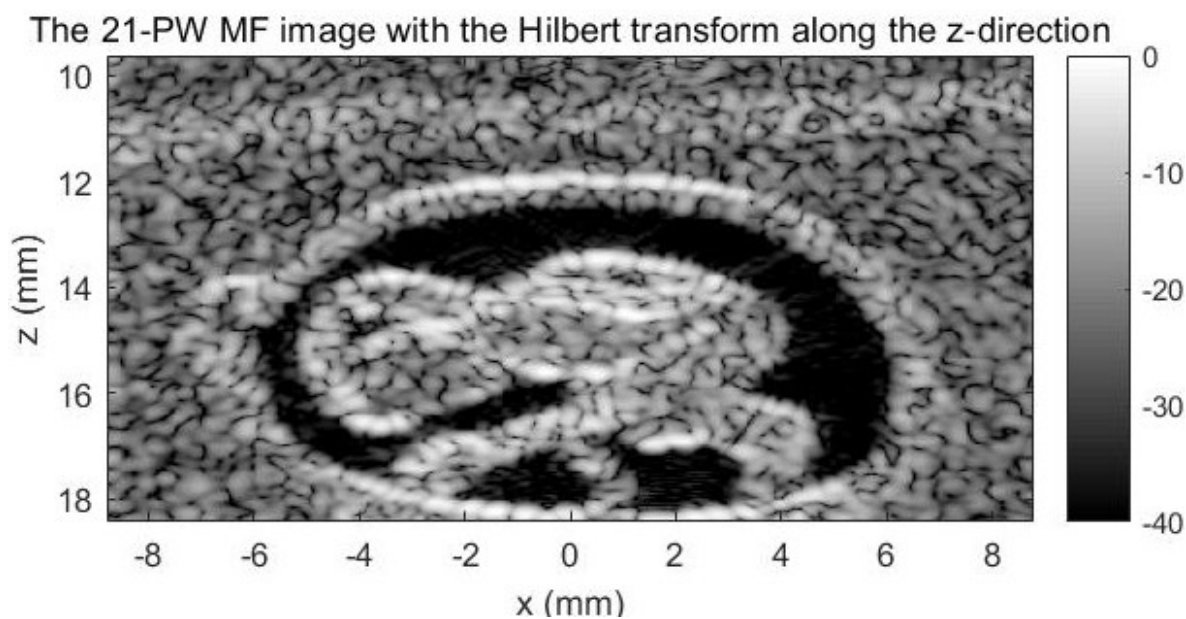


Figure 3.23: The normalized envelop in dB of the z-directional Hilbert transformation.

The 2D-FFT and 2D-DCT of the MF image are shown in figure 3.24. It shows that the image is over-sampled. Oversampling can make some transforms (like DCT and FFT) sparse. However, the sparsity caused by oversampling cannot improve the image

quality and such sparsity is unnecessary and avoidable. Therefore, this over-sampled image should be down-sampled to the Nyquist sampling rate. This can reduce the interference in finding a good sparse space of the US image.

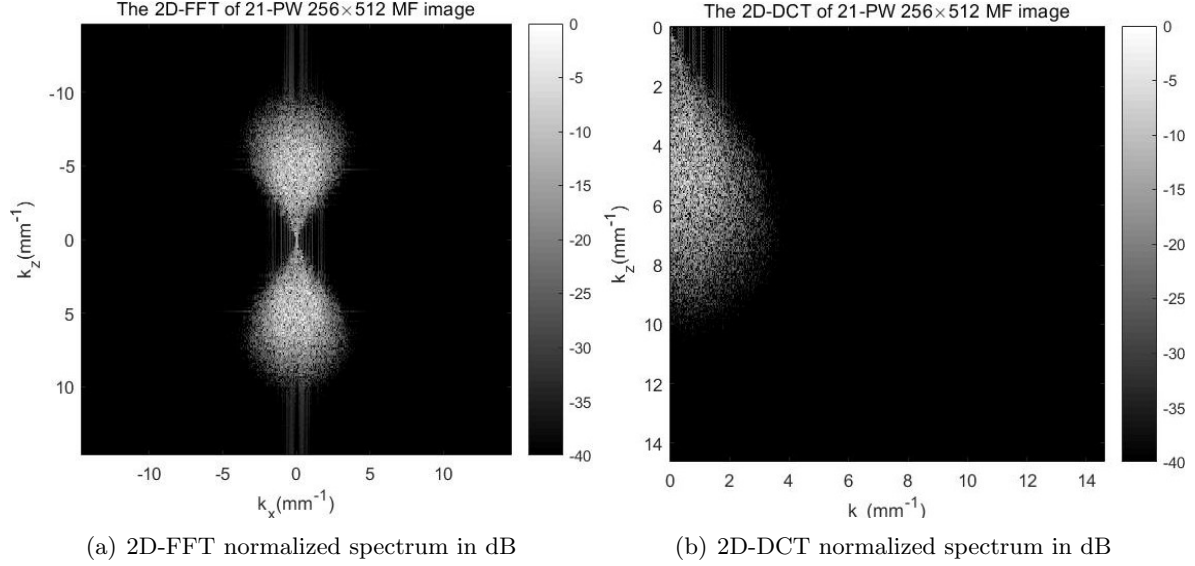


Figure 3.24: The 2D-FFT and 2D-DCT normalized envelope of the fetus phantom 21-PW MF image.

Figure 3.25 shows the normalized absolute values from -40dB to 0dB of the Nyquist sampling MF image. The normalized RMSE between the over-sampled image and the Nyquist sampling image is about 6.87%, so it is a good approximation.

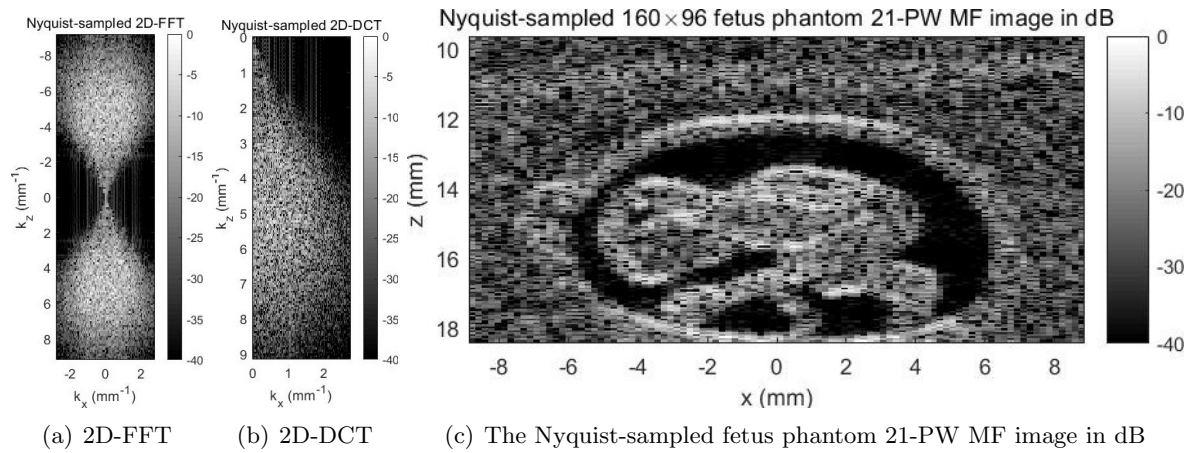


Figure 3.25: The normalized absolute values in dB of Nyquist sampling fetus phantom MF image and its 2D-FFT and 2D-DCT.

Figure 3.26 shows the envelop in dB of the Hilbert transformation with the Tukey window in z-direction of the Nyquist sampling fetus phantom MF image. The ratio

of the Tukey window is 0.2. The most details shown in Figure 3.23 is also shown in Figure 3.26, such as the umbilical cord and the edges of the spine. Therefore, Figure 3.25(c) is chosen as the true image, to which the reconstructions are compared.

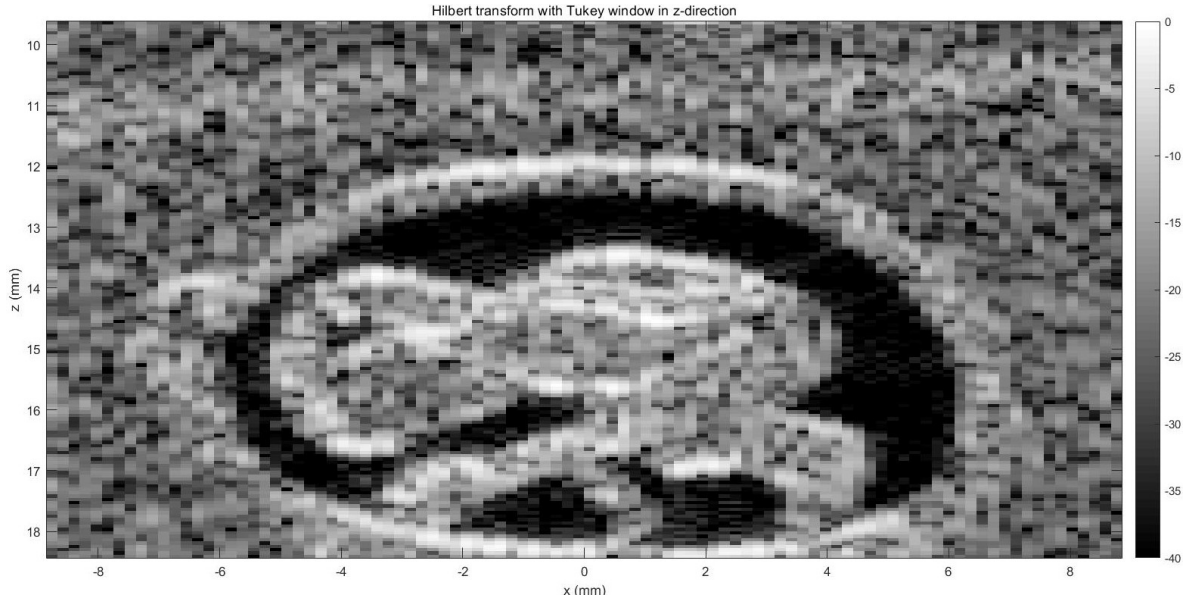


Figure 3.26: The normalized envelop from -40dB to 0dB of the Hilbert transformation with Tukey window in z-direction of the Nyquist sampling fetus phantom MF image.

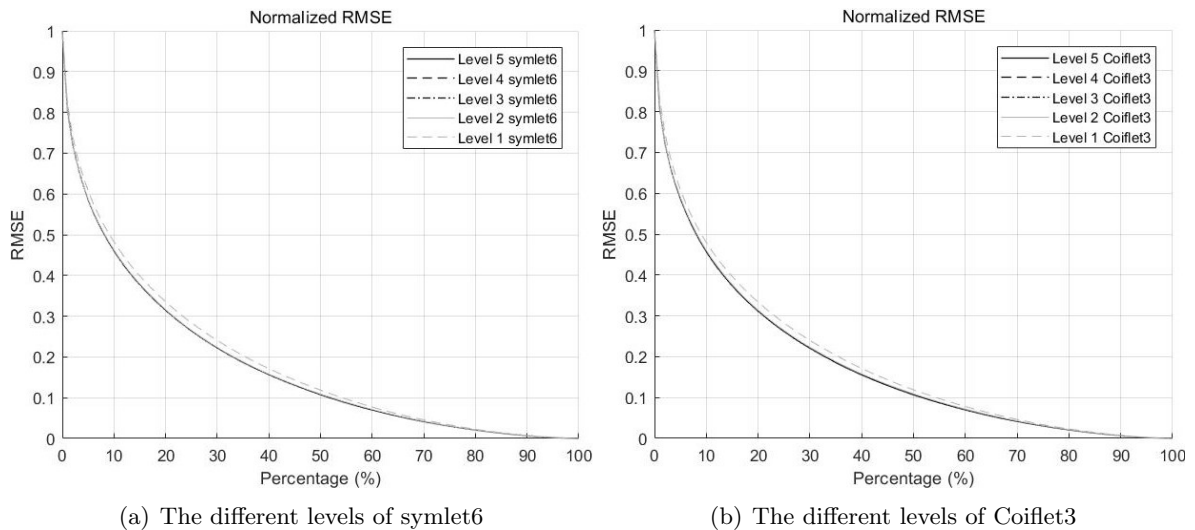


Figure 3.27: Comparison among the different levels of the symlet6 and the Coiflet3.

Figure 3.27(a) shows the curves of the symlet6 from level 1 to level 5 respectively. The level 1 symlet6 is not as sparse as the others, and the difference from level 2 to level 5 is little. Figure 3.27(b) shows the curves of the Coiflet3 from level 1 to level 5

respectively. The level 1 Coiflet3 is also not as sparse as the others. For many other 2D-DWTs, the sparsity also varies little from level 2 to level 5. So, for this fetus MF image, the level of 2D-DWT can be chosen as 5.

Figure 3.28(a) shows the curves of the level 5 2D-DWTs with the filters Haar, symlet4, symlet6 Coiflet3, Coiflet4 and Meyer respectively. The difference of their sparsity is little.

According to Figure 3.24, the fetus MF image has different frequency characteristics in the x and z direction. So one idea for improving the sparsity is that the 2D-DWT can apply different filters in x and z directions. Another idea is that two different 1D-DWTs can be used in x and z directions with different filters and different levels, which is a kind of wavelet packet transform but with different filters in different dimensions. We will refer to this technique as 'wavelet packet' for the remainder of this thesis. Therefore, the level 5 2D-DWT with the symlet6 and Coiflet3 filters in x and z directions is compared with the level 5 symlet6 and Coiflet3 2D-DWTs, and the wavelet packet transform which performs level 1 Coiflet4 and level 3 Coiflet3 1D-DWTs in x and z directions is compared with the 2D-DWTs and the wavelet packet transforms with the single filters. Figure 3.28(b) shows the comparison of their sparsity. We can see that 2D-DWT with the symlet6 and Coiflet3 filters in x and z directions is sparser than symlet6 and Coiflet3 2D-DWTs, and the wavelet packet transform which performs level 1 Coiflet4 and level 3 Coiflet3 1D-DWTs in x and z directions is the sparsest transform among these transforms. Therefore, as for the sparse space of the ultrasound images, the 2D-DWT with different filters in two directions can work better than the normal 2D-DWTs and the wavelet packet can also have better performance with different filters in two directions, and the wavelet packet transform can work better than the 2D-DWT but the subband tree needs selecting.

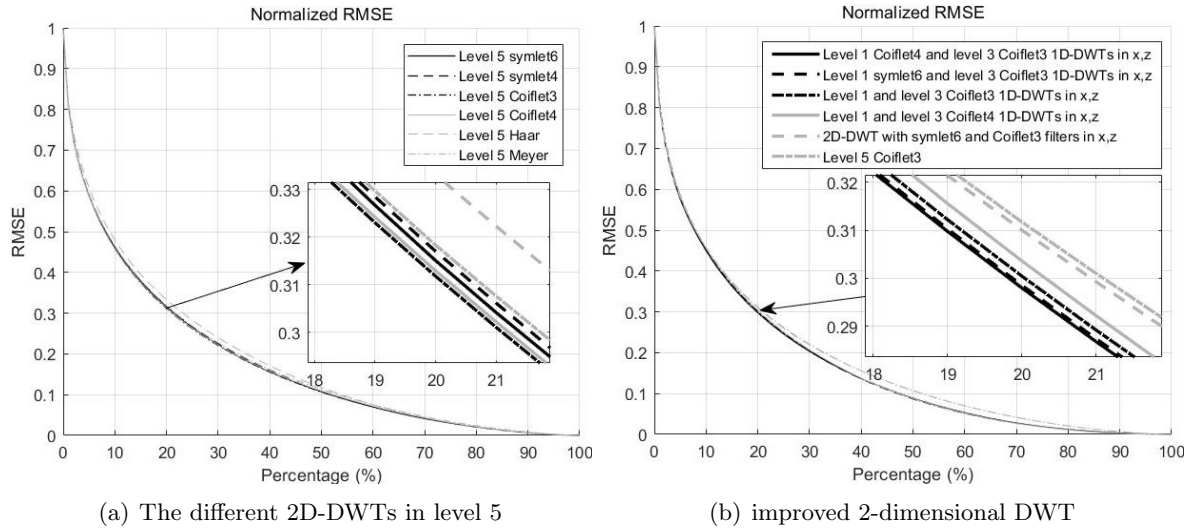


Figure 3.28: Comparison of the different 2D-DWTs.

Figure 3.29(a) shows the curves of the block 2D-DCT with the block size 8×6 , 8×4 , 8×8 , 4×6 , 16×6 and 16×12 respectively. In this case, the block 2D-DCT with

block size 8×6 is sparser than the others. Figure 3.29 shows the curves of the spatial domain, 2D-DCT, 2D-FFT, different 1D-DWTs in two directions, block 2D-DCT with block size 8×6 and wave atom respectively. As the number of wave atom coefficients is larger than that of the image pixels, so it uses the same number of coefficients as the other transformations. According to the curves, the wave atom and the block 2D-DCT and different 1D-DWTs in two dimensions are sparser than the others. But, since the wave atom coefficients are more than the image pixels, it is not as good as block 2D-DCT and different 1D-DWTs in two directions.

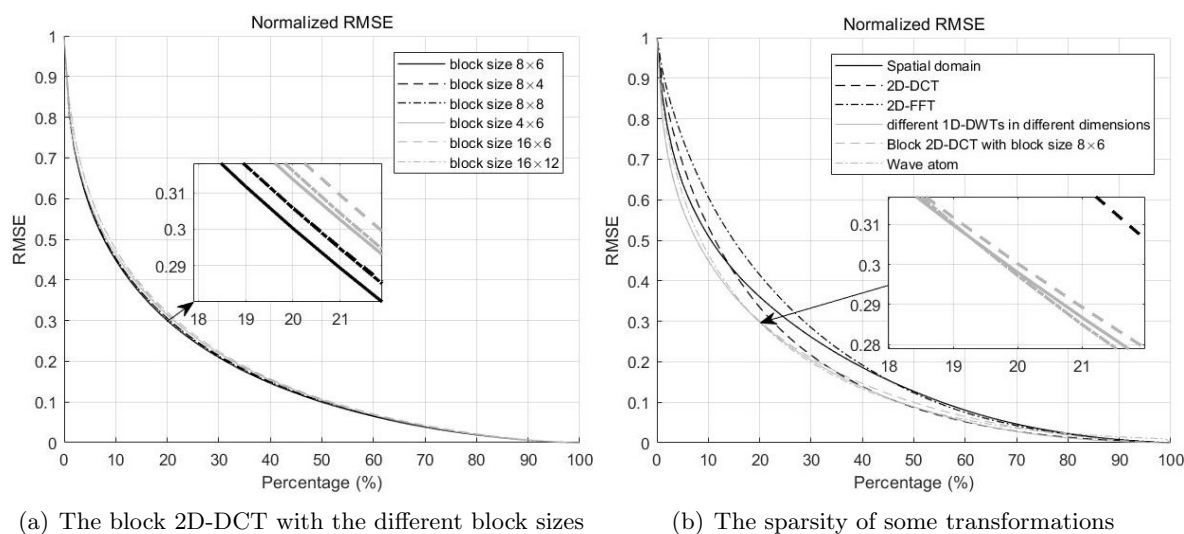


Figure 3.29: The sparsity of block 2D-DCT and some other transformations.

Figure 3.30 shows the level 5 Meyer DWT spectrum of the fetus phantom 21-PW MF image and the positions of its maximum 15% coefficients.

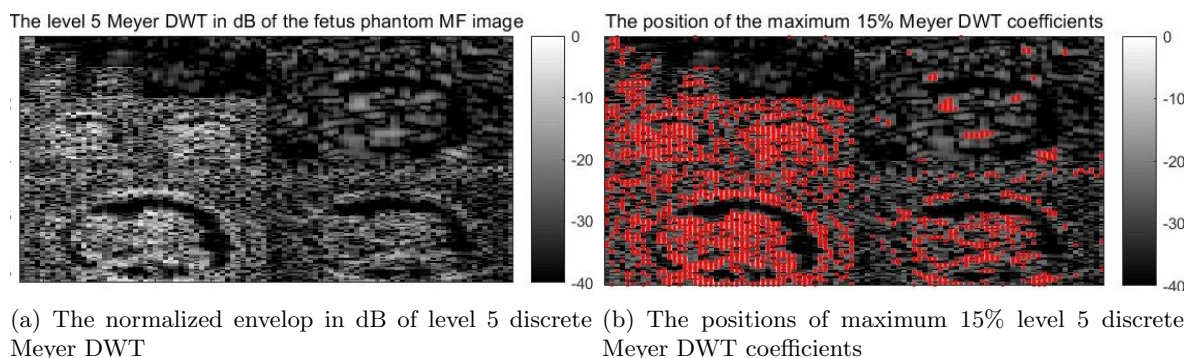


Figure 3.30: The level 5 discrete Meyer DWT of the fetus phantom 21-PW MF image, and the positions of its maximum 15% coefficients.

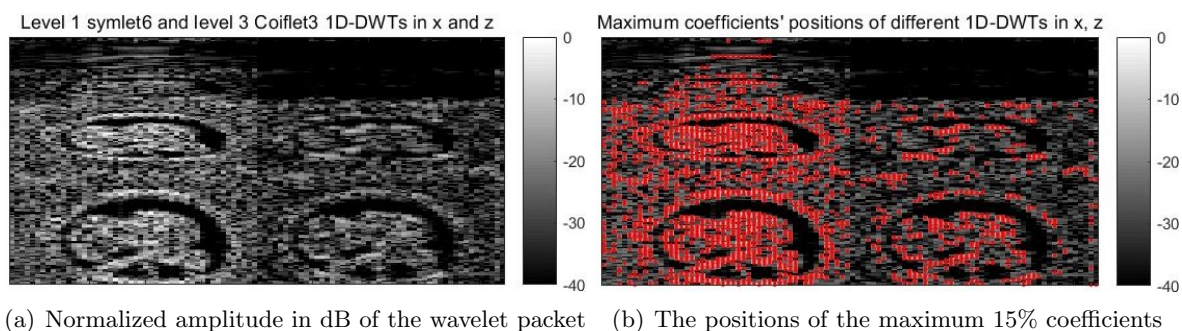


Figure 3.31: The wavelet packet performing level 1 symlet6 and level 3 Coiflet3 1D-DWTs in x and z directions of the fetus phantom 21-PW MF image, and the positions of its maximum 15% coefficients.

Figure 3.31 shows the wavelet packet transform which performs level 1 symlet6 and level 3 Coiflet3 1D-DWTs in x and z dimensions of the fetus phantom 21-PW MF image and the positions of its maximum 15% coefficients.

Figure 3.32 shows the block 2D-DCT spectrum with block size 8×6 of the fetus phantom 21-PW MF image and the positions of its maximum 15% coefficients.

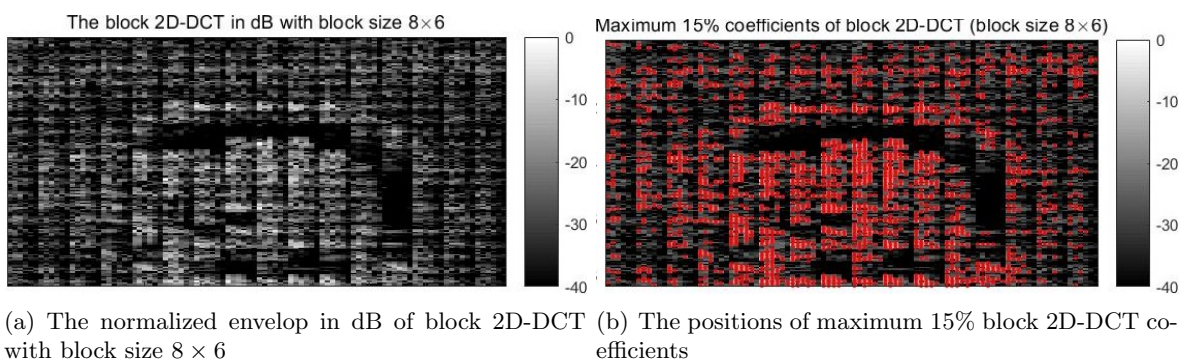


Figure 3.32: The block 2D-DCT in dB with block size 8×6 of the fetus phantom 21-PW MF image, and the positions of its maximum 15% coefficients.

Figure 3.33 shows the wave atom spectrum of the fetus phantom 21-PW MF image and the positions of its maximum coefficients. We can see that the number of wave atom coefficients is 160×160 , which is larger than the number of image pixels. So the wave atom is not an orthogonal transform for this case.

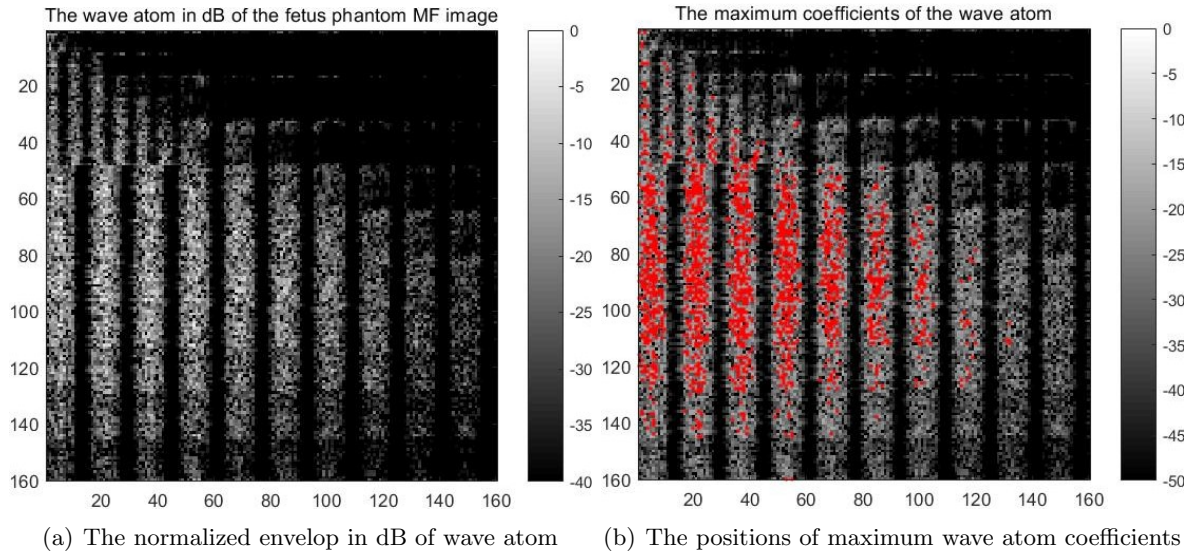


Figure 3.33: The wave atom in dB of the fetus phantom 21-PW MF image, and the positions of its maximum coefficients.

Figure 3.34(a) shows the normalized absolute values in dB of the reconstruction from the maximum 15% level 5 Meyer 2D-DWT coefficients shown in Figure 3.30(b). Figure 3.34(b) shows the normalized absolute values in dB of the reconstruction from the maximum 15% coefficients of the wavelet packet shown in Figure 3.31(b). Figure 3.34(b) has better contrast than Figure 3.34(a).

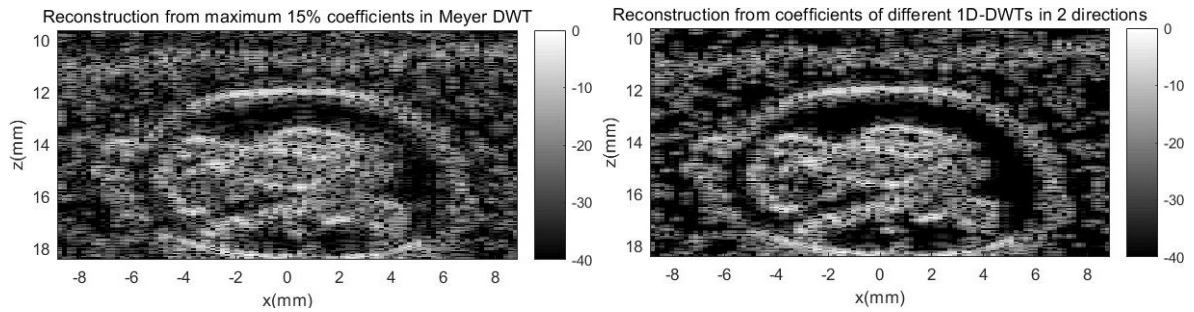
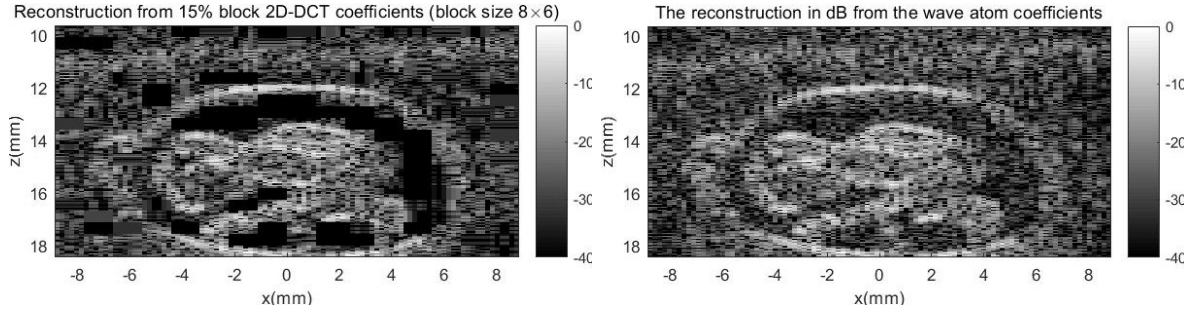


Figure 3.34: The reconstruction from the maximum 15% coefficients in level 5 discrete Meyer DWT and the wavelet packet performing level 1 symlet6 and level 3 Coiflet3 1D-DWTs in x and z directions.

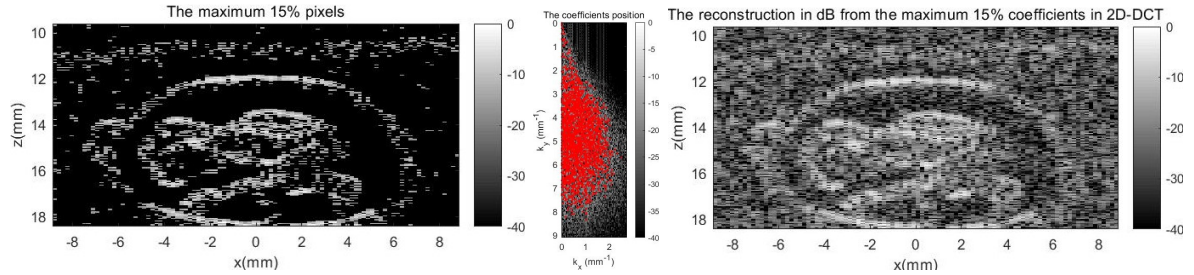
Figure 3.35(a) shows the reconstruction from the maximum 15% coefficients of the block 2D-DCT shown in Figure 3.32(b). We can see some block artifacts. It is because the image is divided into many blocks to perform the 2D-DCT on each block. Figure 3.35(b) shows the reconstruction from the maximum 15% wave atom coefficients shown in Figure 3.33(b).



(a) Log-compression of reconstruction from maximum 15% coefficients of block 2D-DCT with block size 8×6 (b) The log-compression of the reconstruction from the maximum 15% coefficients of wave atom

Figure 3.35: The reconstructions from the maximum 15% pixel number coefficients in block 2D-DCT with block size 8×6 and in wave atom of the fetus phantom 21-PW MF image.

Figure 3.36(a) shows the normalized absolute values in dB of the maximum 15% pixels in the fetus phantom MF image. Choosing spatial domain as sparse space will cause the weak scatterers ignored, since weak scatterers are usually not sparse in spatial domain. However, because we often see the log-compressed US image and log-compression will emphasize the weak scatterers, ignoring weak scatterers will severely influence the image quality. So Figure 3.36(a) looks bad. Figure 3.36(b) indicates the maximum 15% 2D-DCT coefficients of the fetus phantom MF image, and Figure 3.36(c) shows the reconstruction from them. The reconstruction is distorted. Because the 2D-DCT is not good at representing the local spatial characteristics, the reconstruction has bad contrast.



(a) The log-compression of the maximum 15% pixels of the 21-PW MF image (b) DCT coefficients (c) The reconstruction from the maximum 15% 2D-DCT coefficients

Figure 3.36: The maximum 15% pixels of the fetus phantom 21-PW MF image, and the maximum 15% 2D-DCT coefficients of the fetus phantom MF image, and the normalized absolute values in dB of the reconstruction from the maximum 15% 2D-DCT coefficients.

3.2.2 The experimental carotid MF image

Next, we analyze a beamformed US image from an *in vivo* measurement. Some imaging parameters are listed in table 3.2.

sampling frequency	$f_s = 20.832MHz$
ultrasound wave speed	$c_0 = 1540m/s$
pitch	$0.150mm$

Table 3.2: Parameters of the experimental carotid MF image

The pixel length in x-direction and z-direction is equal to the pitch and $c_0/2f_s$ respectively. The normalized amplitudes from -50dB to 0dB of the 901×246 carotid ultrasound image is shown as Figure 3.37(a), and Figure 3.37(b) shows the normalized envelop from -50dB to 0dB of its z-directional Hilbert transform. In this part, the dB range for the images is from -50dB to 0dB.

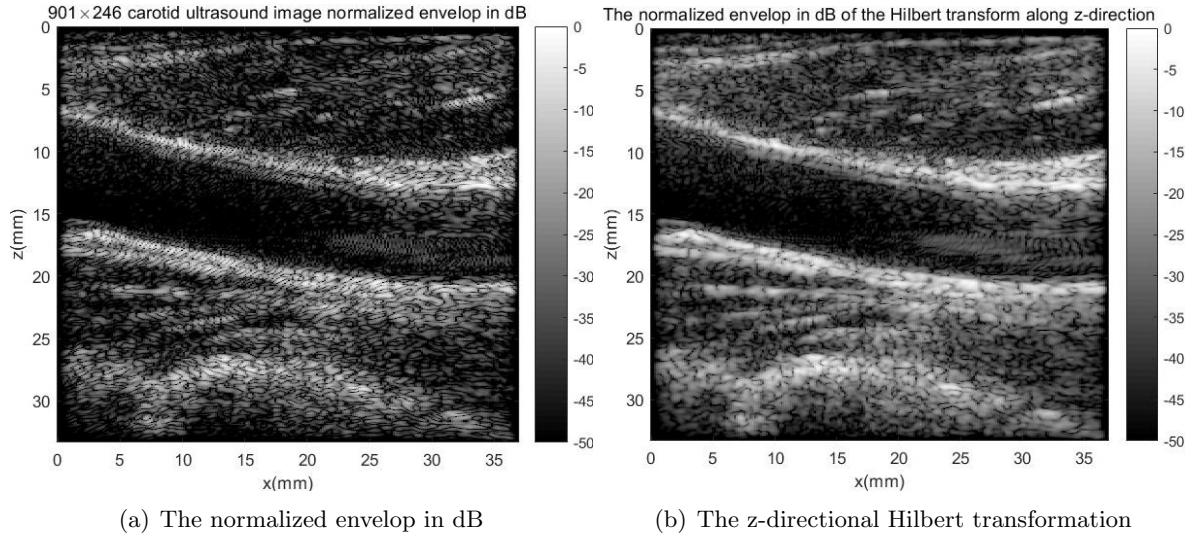


Figure 3.37: The 901×246 carotid ultrasound image.

The 2D-DCT and 2D-FFT of the 901×246 carotid ultrasound image are shown in Figures 3.38(a) and 3.38(d) respectively. The image is approximately band-limited, so truncating the 2D-DCT will only change the image envelop a little. To avoid the unnecessary sparsity, the 2D-DCT matrix is truncated from the 225th row to the 640th row and from the first column to the 128th column. To eliminate the discontinuities caused by truncation, a window shown in Figure 3.38(b) is multiplied to the cropped 2D-DCT. The window in z-direction is the Tukey window with ratio 0.1, and it in x-direction is half of the Tukey window with ratio 0.05. Figure 3.38(c) shows the truncated and windowed 2D-DCT.

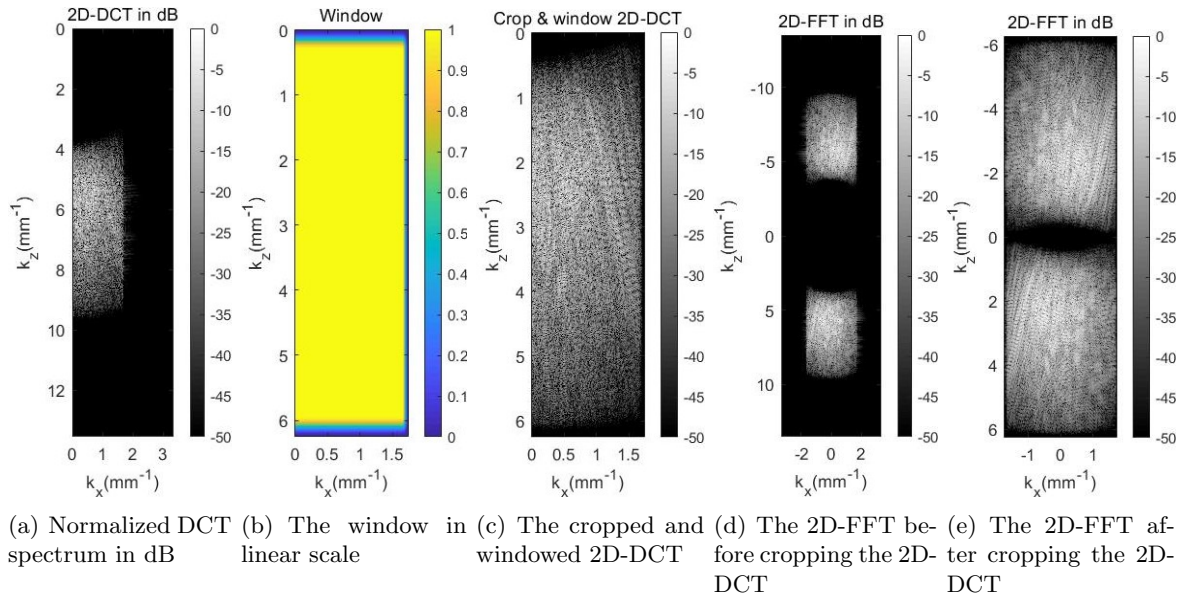


Figure 3.38: The normalized 2D-FFT and 2D-DCT spectrum from -50dB to 0dB of both the carotid ultrasound images before and after truncating and windowing in the 2D-DCT.

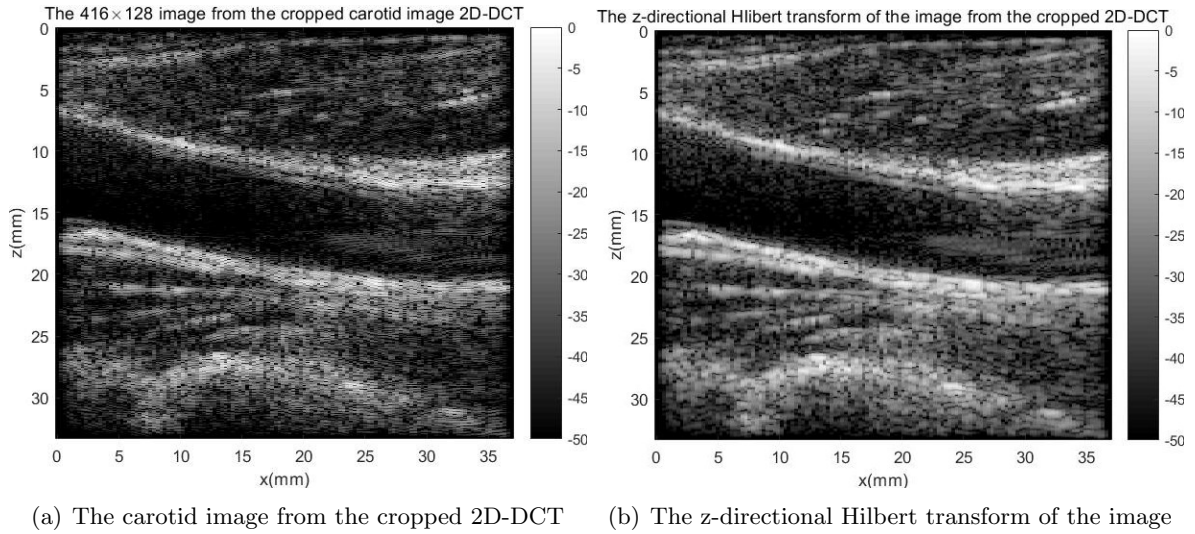


Figure 3.39: The carotid image from the cropped and windowed 2D-DCT and its z-directional Hilbert transform envelop in dB.

Figure 3.39(a) shows the normalized amplitude in dB of the inverse 2D-DCT from the truncated and windowed 2D-DCT. Figure 3.39(b) shows the z-directional Hilbert transform normalized envelop in dB of the 2D-IDCT image. The 2D-IDCT image remains most details in original carotid ultrasound image and the normalized RMSE between original 2D-DCT and windowed truncated 2D-DCT is only about 1.92%. Therefore, it is better to look for the sparse space of the truncated 2D-DCT. In other words, it

is better for analyzing the sparse space of the ultrasound images to regard the 2D-IDCT carotid image from the truncated 2D-DCT as the true image.

Figure 3.40(a) shows the curves of the discrete Meyer 2D-DWT from level 1 to level 5 respectively. The level 5 is also one of the sparsest among them. Therefore, as for 2D-DWTs, level 5 is one of the sparsest levels. Figure 3.40(b) shows the curves of the level 5 Meyer and different Daubechies 2D-DWTs. The Meyer 2D-DWT is sparser than the Daubechies 2D-DWTs.

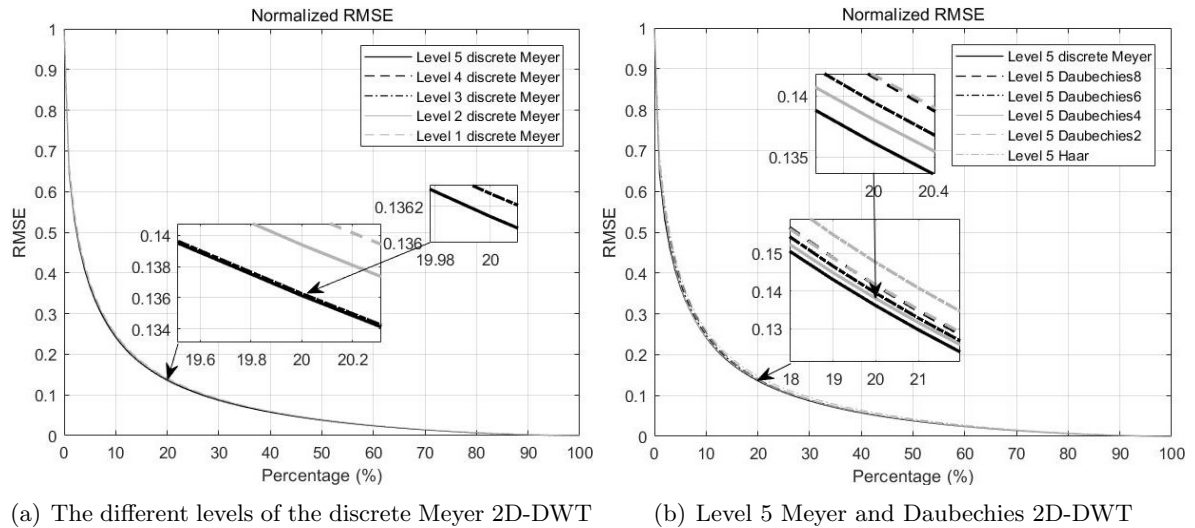


Figure 3.40: Comparison of the different levels the Meyer 2D-DWT and different level 5 Daubechies 2D-DWT.

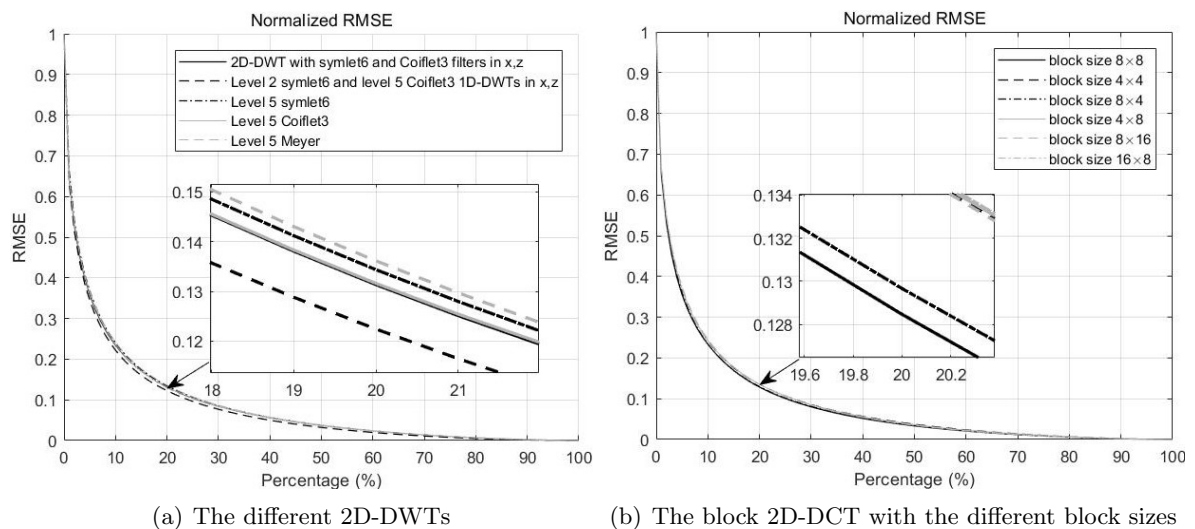
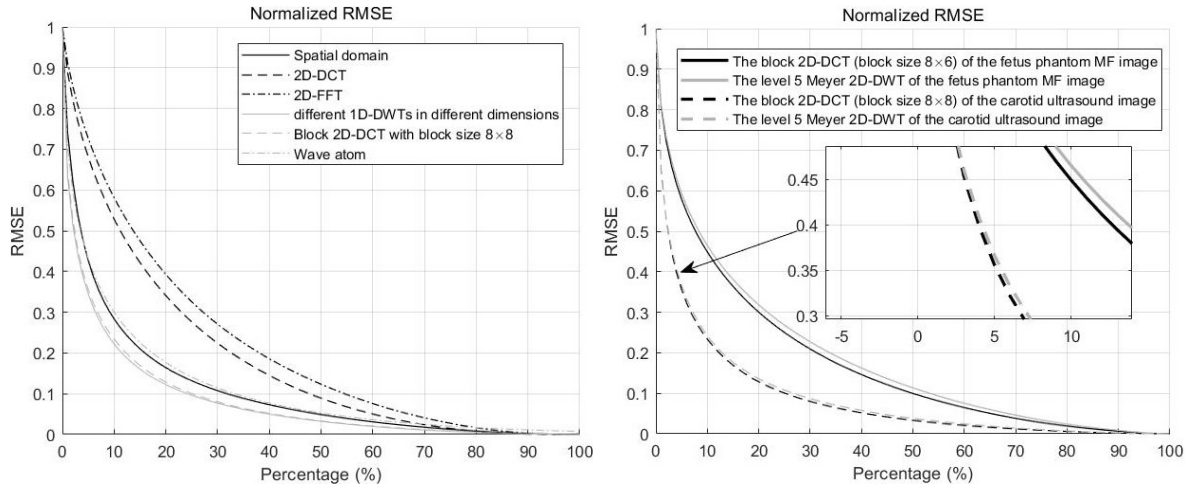


Figure 3.41: Comparison of the different 2D-DWTs and comparison of the block 2D-DCT with the different block sizes.

Figure 3.41(a) shows the curves of three level 5 2D-DWTs with the filters Meyer, symlet6, Coiflet3, and the level 5 2D-DWT with symlet6 and Coiflet3 in x and z directions, and the wavelet packet performing level 2 symlet6 and level 5 Coiflet3 1D-DWTs in x and z directions. The wavelet packet is sparser than others. According to Figure 3.38(e), carotid MF image also has different frequency characteristics in x and z directions, so it can be sparser than the normal 2D-DWTs to use different 1D-DWTs in two directions or use the 2D-DWT with different filters in two dimensions, which is corresponding to Figure 3.41(a). Figure 3.41(b) shows the curves of the block 2D-DCT with the block size 8×8 , 4×4 , 8×4 , 4×8 , 8×16 and 16×8 respectively. In this case, the block 2D-DCT with block size 8×8 is sparser than the others. Here the pixel size is about 0.29mm in x-direction and about 0.08mm in z-direction. The physical size of the 8×8 block is about 2.31mm in x-direction and 0.64mm in z-direction.

Figure 3.42(a) shows the curves of the spatial domain, 2D-DCT, 2D-FFT, wavelet packet, block 2D-DCT with block size 8×8 and wave atom respectively. The wavelet packet with different filters in two directions is sparser than the other transforms. But the improvement of the sparsity is not much compared to spatial domain. In frequency domain, the sparsity is worse. It is typically difficult to sparse represent an image with strong boundaries in frequency domain. Theoretically, the spatial sparsity and the frequency sparsity of one image observe an uncertainty principle.[11] Namely, since the carotid MF image is fairly sparse in spatial domain, its frequency domain is not that sparse. Figure 3.42(b) shows the comparison of the sparsity between the fetus phantom MF image and the carotid ultrasound image. The carotid ultrasound image is much sparser than the fetus phantom MF image.

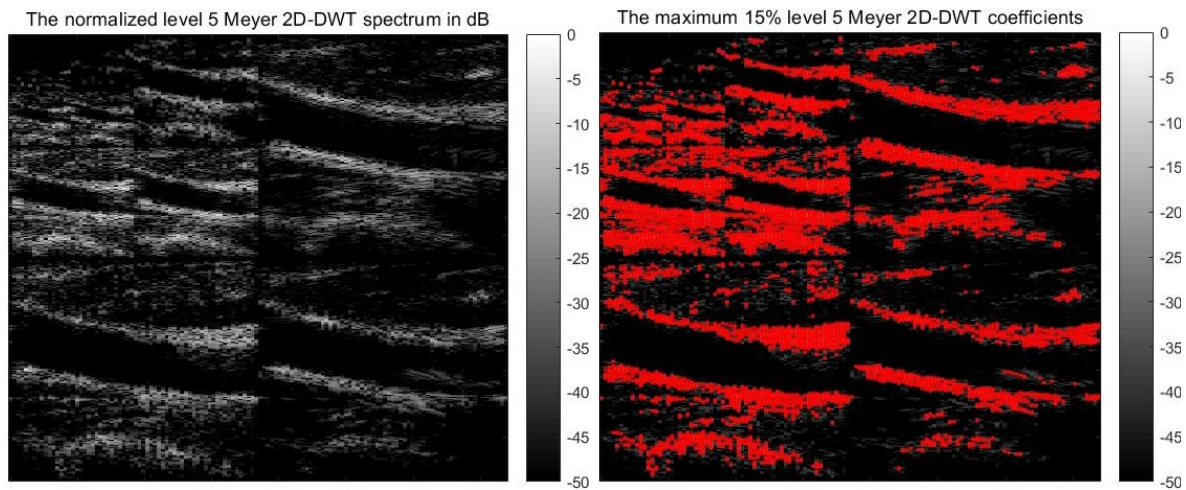


(a) The different transforms of the carotid ultrasound image (b) Level 5 Meyer 2D-DWT and block 2D-DCT of the fetus phantom MF image and the carotid MF image

Figure 3.42: Sparsity of some other transformations and comparison of the sparsity between the fetus phantom MF image and the carotid ultrasound image.

In this case, the transformation applying two different 1D-DWTs in two directions and the block 2D-DCT are sparser than the others.

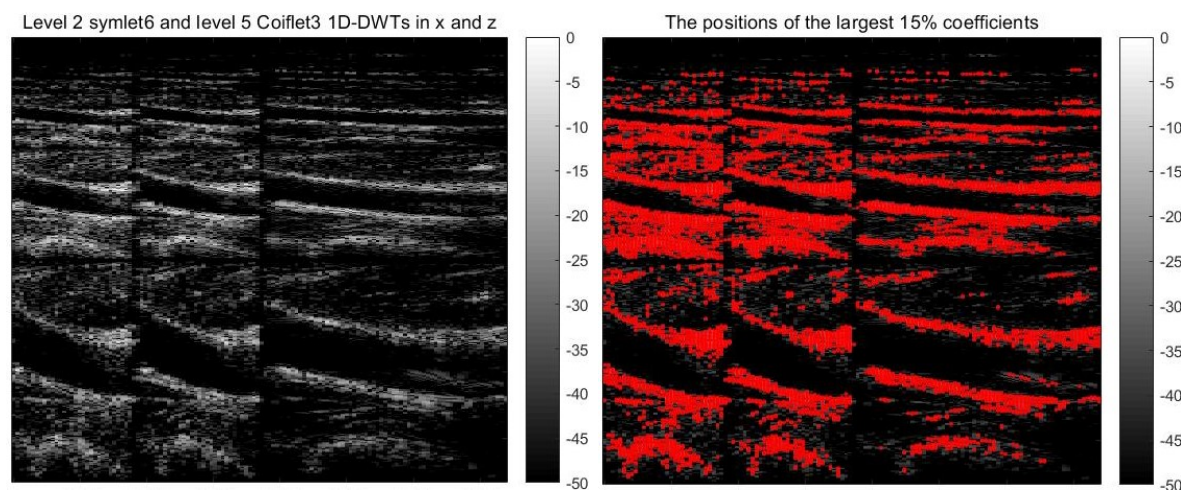
Figure 3.43 shows the level 5 Meyer 2D-DWT normalized spectrum in dB of the carotid image and the positions of its maximum 15% coefficients.



(a) The normalized spectrum in dB of level 5 Meyer 2D-DWT (b) The positions of maximum 15% level 5 discrete Meyer DWT coefficients

Figure 3.43: The carotid image level 5 Meyer 2D-DWT normalized spectrum in dB, and the positions of its maximum 15% coefficients.

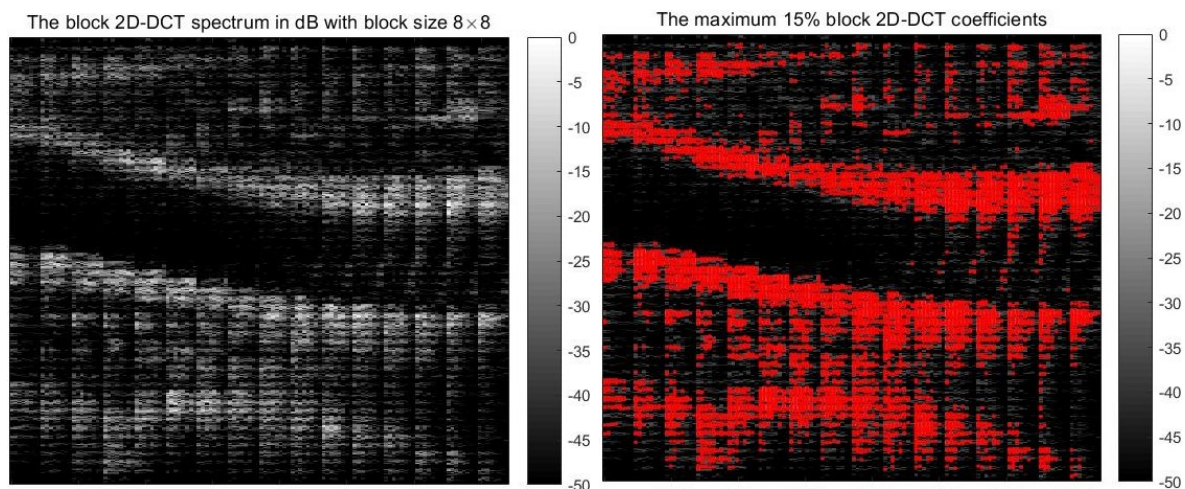
Figure 3.44 shows the normalized spectrum in dB of the wavelet packet which performs level 2 symlet6 and level 5 Coiflet3 1D-DWTs in x and z directions and the positions of its maximum 15% coefficients.



(a) The normalized spectrum in dB of level 2 symlet6 and level 5 Coiflet3 1D-DWTs in x and z (b) The positions of maximum 15% coefficients of level 2 symlet6 and level 5 Coiflet3 1D-DWTs in x and z

Figure 3.44: Normalized spectrum in dB of wavelet packet performing level 2 symlet6 and level 5 Coiflet3 1D-DWTs in x and z direction, and the positions of its maximum 15% coefficients.

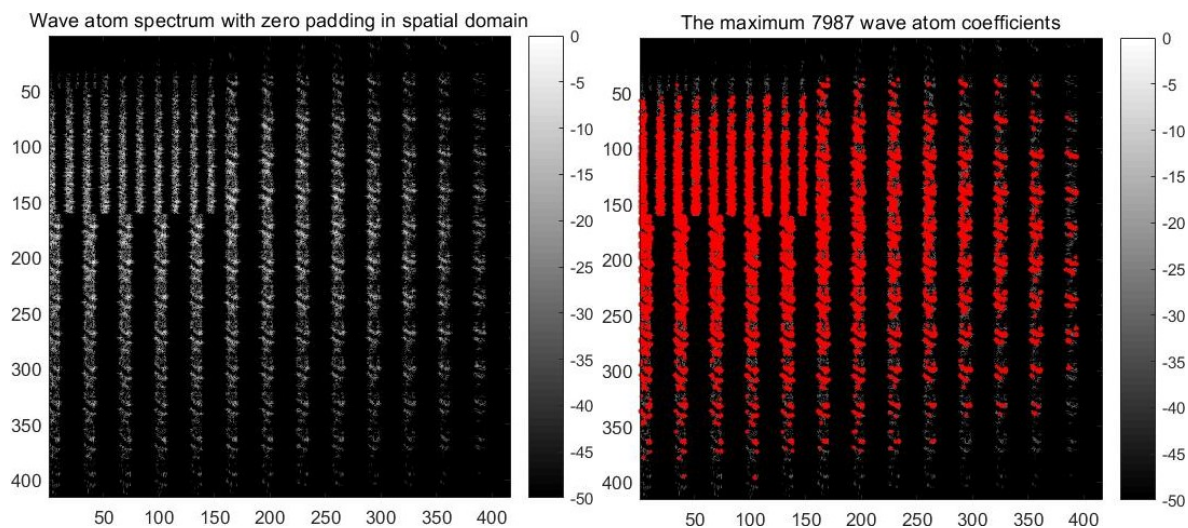
Figure 3.45 shows the block 2D-DCT normalized spectrum in dB with block size 8×8 of the carotid image and the positions of its maximum 15% coefficients.



(a) The normalized spectrum in dB of block 2D-DCT with block size 8×8 (b) The positions of the maximum 15% block 2D-DCT coefficients

Figure 3.45: The block 2D-DCT normalized spectrum in dB with block size 8×8 of the carotid image, and the positions of its maximum 15% coefficients.

Figure 3.46 shows the normalized wave atom spectrum in dB of the carotid image and the positions of its maximum 7987 coefficients.

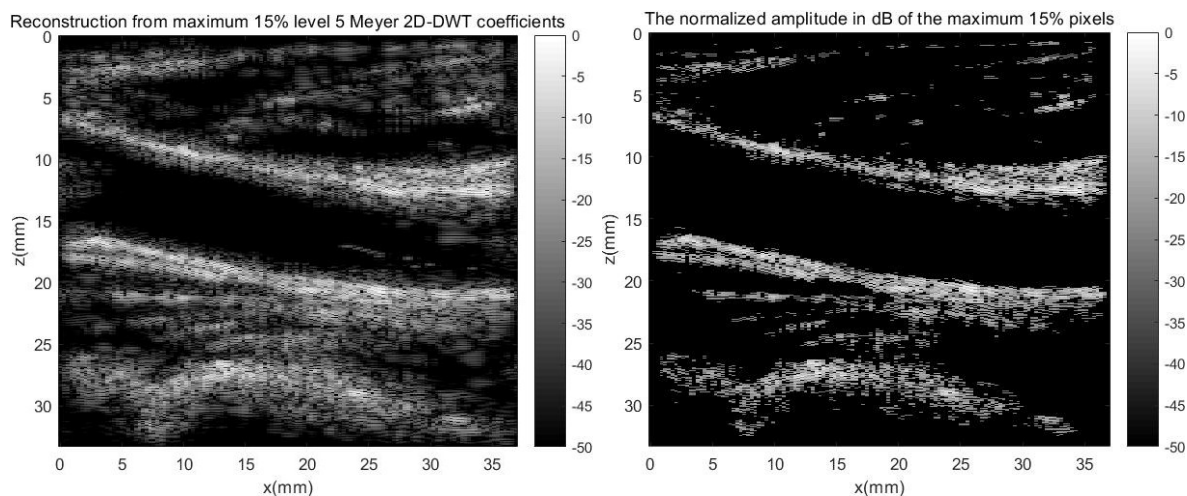


(a) The normalized spectrum in dB of wave atom (b) The positions of maximum 7987 wave atom coefficients

Figure 3.46: The wave atom in dB of the fetus phantom 21-PW MF image, and the positions of its maximum coefficients.

Figure 3.47(a) shows the normalized amplitude in dB of the reconstruction from the

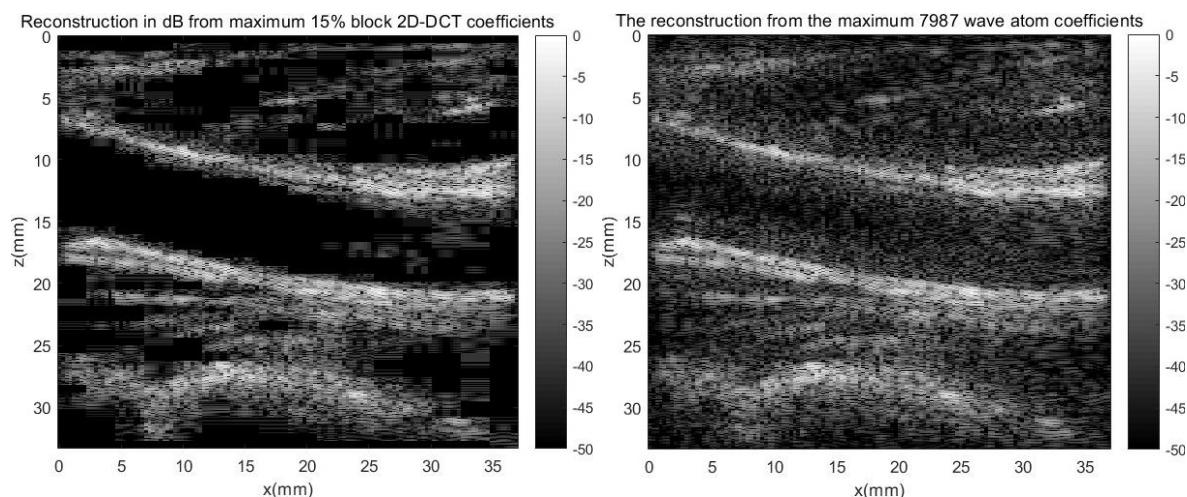
maximum 15% coefficients shown in Figure 3.43(b). Figure 3.47(b) shows the maximum 15% pixels in the carotid image.



(a) The log-compression of the reconstruction from the maximum 15% coefficients of level 5 Meyer 2D-DWT (b) The normalized amplitudes in dB of the maximum 15% pixels of the carotid image

Figure 3.47: The reconstruction from the maximum 15% coefficients in level 5 Meyer 2D-DWT, and the maximum 15% pixels of the carotid image.

Figure 3.48(a) shows the reconstruction from the maximum 15% coefficients shown in Figure 3.45(b). Figure 3.48(b) shows the reconstruction from the maximum 15% coefficients shown in Figure 3.46(b).



(a) Log-compression of reconstruction from maximum 15% coefficients of block 2D-DCT with block size 8×8 . (b) The normalized amplitudes in dB of the reconstruction from the maximum coefficients of wave atom

Figure 3.48: The reconstructions from the maximum 15% pixel number coefficients in block 2D-DCT with block size 8×8 and in the wave atom of the carotid image.

Figure 3.49 shows the reconstruction from the maximum 15% coefficients shown in Figure 3.44(b).

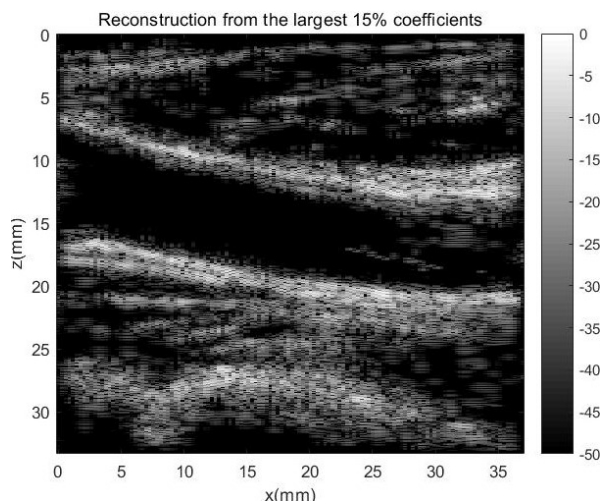
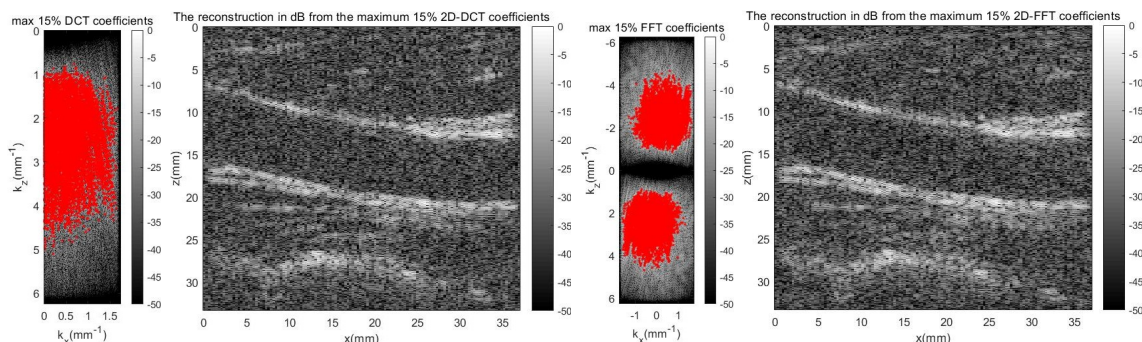


Figure 3.49: The reconstruction from the largest 15% coefficients of level 2 symlet6 and level 5 Coiflet3 1D-DWTs in x and z directions

Figures 3.50(a) and 3.50(c) indicate the maximum 15% 2D-DCT and 2D-FFT coefficients, and Figures 3.50(b) and 3.50(d) show their reconstructions. The reconstructions are distorted.



(a) Max DCT coefficients (b) The reconstruction from the maximum 15% 2D-DCT coefficients (c) Max FFT coefficients (d) The reconstruction from the maximum 15% 2D-FFT coefficients

Figure 3.50: Maximum 15% coefficients and their reconstructions for 2D-DCT and 2D-FFT of carotid image.

3.3 Sparse dictionary learning for the US images

The above simulations do not find a enough good sparse space for the US images, so in this paragraph, the K-SVD algorithm described in Section 2.3.3 on page 10 is performed on several experimental beamformed carotid US images to train a good sparse dictionary of the carotid US images. The experimental data used for the learning

are from two healthy volunteers, and then the obtained sparse dictionary is tested on the beamformed carotid US image of a third volunteer. Figure 3.51 shows the carotid US images used for the learning, the experimental carotid US image I and II, and their 2D-DCTs.

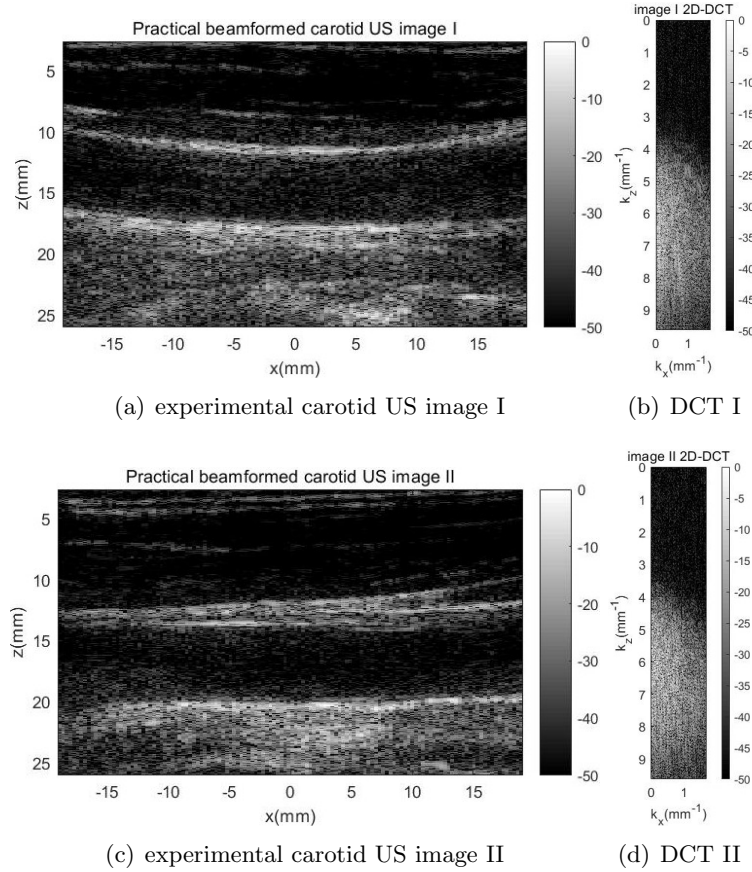


Figure 3.51: The experimental beamformed carotid images used for training, and their 2D-DCTs.

From Figure 3.51(a) and 3.51(c), we can see that there are strong boundaries in these two images, which are the interesting part of the longitudinal carotid images. Figure 3.51(b) and 3.51(d) are the 2D-DCTs of these two carotid US images, and they show that these two US images are mostly band-limited along z-direction in k-space. So their 2D-DCTs can be cropped to reduce the unnecessary sparsity. As an example, the 2D-DCT in Figure 3.52(a) is obtained by cropping the 2D-DCT in Figure 3.51(b). The US image1 and 2 in Figure 3.52(b) and 3.52(c) are gained by respectively performing 2D-IDCT on the cropped 2D-DCTs of the US image I and II. Both image1 and 2 are the 288×128 matrices.

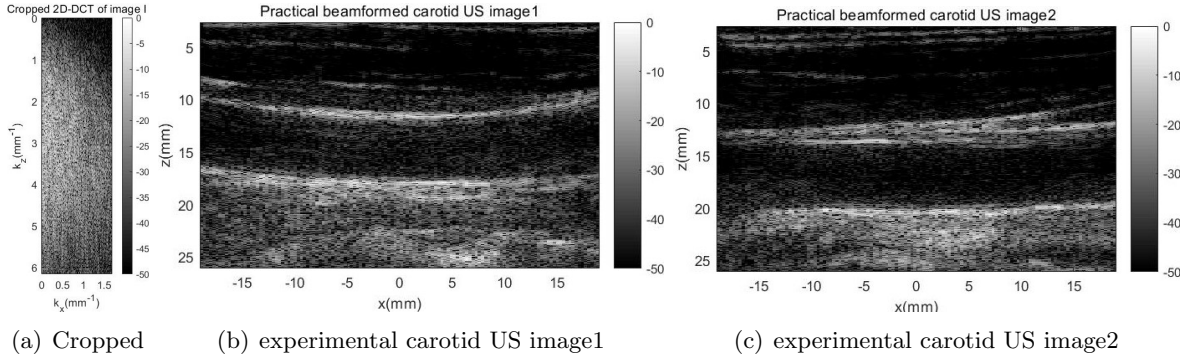


Figure 3.52: The cropped 2D-DCT of the carotid US image I, and the training images reconstructed from their cropped 2D-DCTs (image1 and 2 correspond to image I and II).

The K-SVD algorithm is used for sparse dictionary learning. Due to the computation complexity and the limitation of the computer memory, we divide the training images into a number of patches and K-SVD can only learn the sparse dictionary of these patches. These patches are usually overlapped for training so that we can get much more training samples.

If the digital size of the patch is chosen as 24×16 , two beamformed carotid US images shown above can provide 59890 training samples. The physical size of these patches is about $1.95mm \times 4.77mm$, so we can get local sparse representations. The pixel number of the patch is 384 and it is far smaller than the number of the training samples, so the sample number is sufficient. The training sample set Θ in (2.3) on page 10 will be a 384×59890 matrix. In Θ , the patches have different scattering energy, some are very large and some are very small. Since K-SVD is used to minimize the MSE as (2.3), the dictionary will focus on the patches with high energy. However, these low-energy patches may still show important details in a log-compressed US images, so we will enhance the pixel intensities of these patches. Therefore, the log-compression is applied among the pixel intensities of all the patches. Assume R_{dB} is the dB range of the log-compression and $I_{max} = \max\{\|\theta_1\|_2, \|\theta_2\|_2, \dots\}$ indicates the maximal root of mean energy of the patches, where θ is one patch. So the intensity amplification ratio of the i th patch θ_i is calculated as (3.4). In this case, dB range is $R_{dB} = 50$.

$$Amplification\ ratio = \max\left\{\frac{I_{max}}{\|\theta_i\|_2} \left(1 + \frac{20}{R_{dB}} \log_{10} \frac{\|\theta_i\|_2}{I_{max}}\right), 1\right\}. \quad (3.4)$$

We choose the length of dictionary equal to the pixel number of the patches (i.e., 384), then the \mathbf{D} in (2.3), the sparse dictionary matrix for one patch, will be a 384×384 square matrix. The sparsity constraint T_0 is chosen to be 77, i.e., about 20% of the number of pixels in a patch. So we can get a dictionary by the K-SVD algorithm with the above parameters.

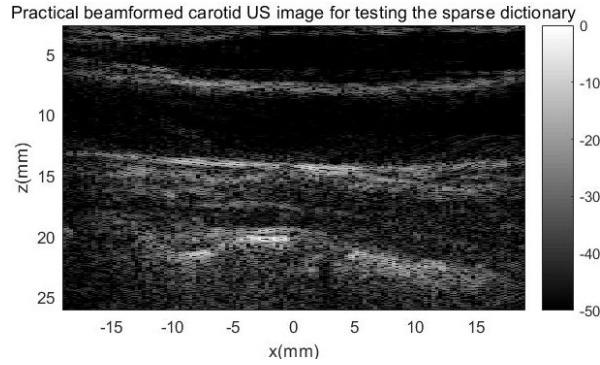


Figure 3.53: A experimental beamformed carotid image used for testing the dictionary.

The obtained dictionary will be tested on another experimental carotid US image shown in Figure 3.53. The 2D-DCT of this image is also cropped and its pixel number is 288×128 as well.

The sparsity curve of the dictionary is drawn in Figure 3.54(b), which is the relationship between the number of non-zero coefficients and RMSE of the reconstruction with these coefficients. Since the dictionary matrix is not necessarily orthogonal or full column rank, the OMP algorithm is used to find a certain number of best representation coefficients of an image. Figure 3.54 compares the sparsity of the dictionary with some other transformations. We can see the dictionary is not that sparse. Some transforms are even sparser than the learned dictionary. Next, we will see the reconstruction image qualities with 10% number of coefficients of the obtained dictionary.

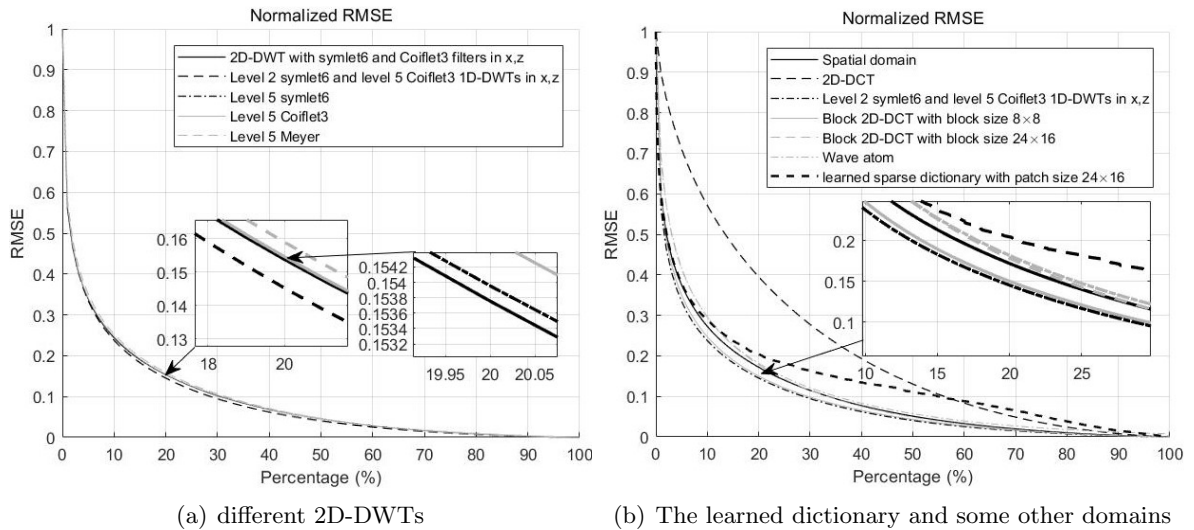


Figure 3.54: The sparsity curves of the learned sparse dictionary and some other transforms.

Figure 3.55 and Figure 3.56 show the reconstructions from the largest 10% coefficients of several transforms. Then, they will be compared with the reconstruction from the largest 10% representation coefficients of the obtained dictionary.

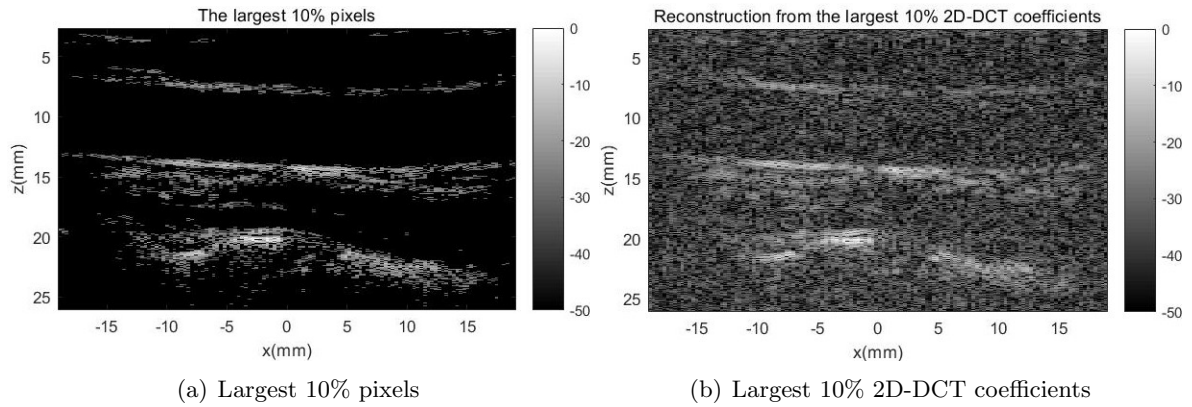


Figure 3.55: Reconstructions from largest 10% coefficients in spatial domain and 2D-DCT.

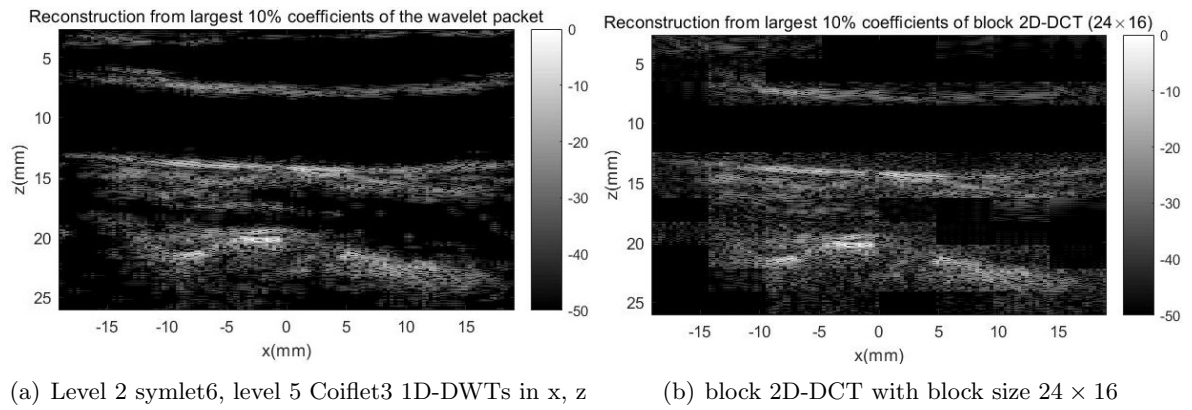


Figure 3.56: Reconstructions from the largest 10% coefficients of the different 1D-DWT in each direction and the block 2D-DCT with block size 24×16 .

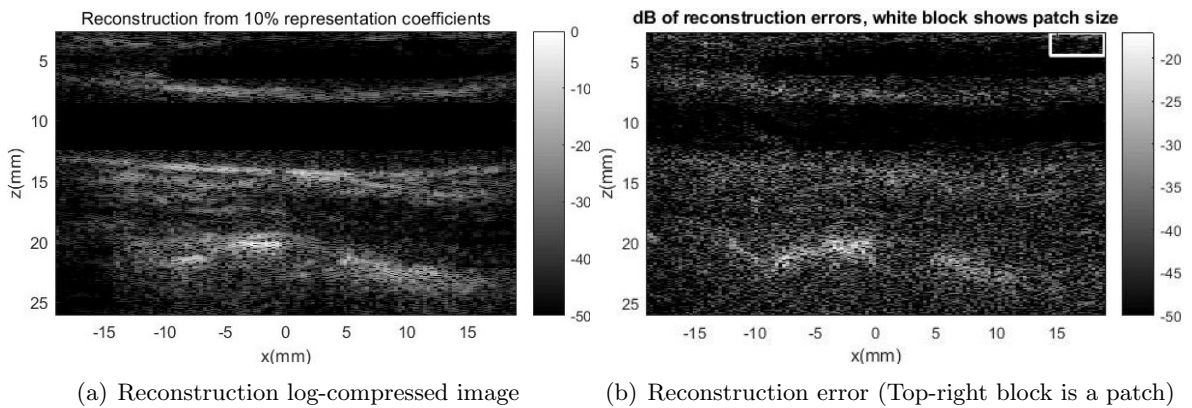


Figure 3.57: Reconstruction from 10% number of the representation coefficients of the learned dictionary with patch size 24×16 , and the error between reconstruction and true image.

Figure 3.57(a) shows the reconstruction from the 10% number of representation coefficients of the learned sparse dictionary, and Figure 3.57(b) shows the reconstruction error. The error is divided by the maximum pixel strength in the true image. The white block at top-right of the error image shows the patch size. In Figure 3.57(a), we can see the boundaries are reconstructed very well. Compared with Figure 3.55, Figure 3.57(a) looks much better. Compared with Figure 3.56, it has better performance on the weak scatterers. However, there are block artifacts in the reconstructed image. So smaller patch may reduce the block artifacts.

Then, the dictionary learning is performed with patch size 8×8 . We perform two simulations. One is performed with the length of dictionary equal to the pixel number of a patch, so the dictionary matrix \mathbf{D} of one patch is a 64×64 square matrix. For the other simulation, the length of dictionary is 8 times number of the pixels in one patch, so the dictionary matrix \mathbf{D} of a single patch becomes a 64×512 fat matrix. This is because the sparsity can increase with longer dictionary. The sparsity curves of these three dictionaries are drawn in Figure 3.58.

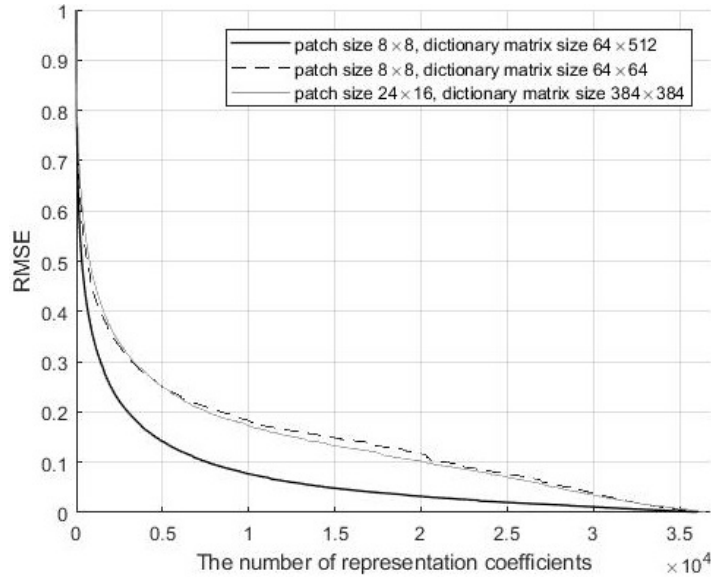


Figure 3.58: Sparsity comparison of three different sparse dictionaries.

From Figure 3.58, we can see that the long dictionary is sparser than the other two dictionaries. As for the two square dictionary matrices corresponding to patch sizes 24×16 and 8×8 , their sparsity are similar. Therefore, we will then compare the reconstructions from a limited number of their representation coefficients. Figure 3.57(a) uses the 10% representation coefficients, so we will use the same number of the coefficients of the other two dictionaries for the reconstructions. As the total coefficient number is 36864, its 10% is about 3686. The total number of coefficients in 8 times fat dictionary is 294912, so its 1.25% number of coefficients is equal to 3686. As for the patch size 8×8 , Figure 3.59(a) shows the reconstruction from the 10% representation coefficients of the square dictionary matrix, and Figure 3.60(a) shows the reconstruction from the 1.25% representation coefficients of the fat dictionary matrix.

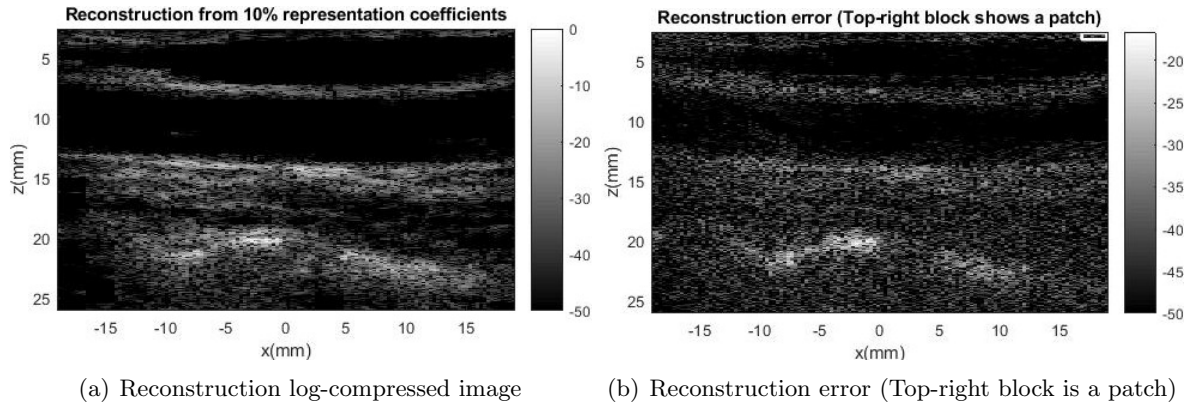


Figure 3.59: Reconstruction from about 10% number of the total 36864 representation coefficients (3686 coefficients) of the square dictionary matrix with patch size 8×8 .

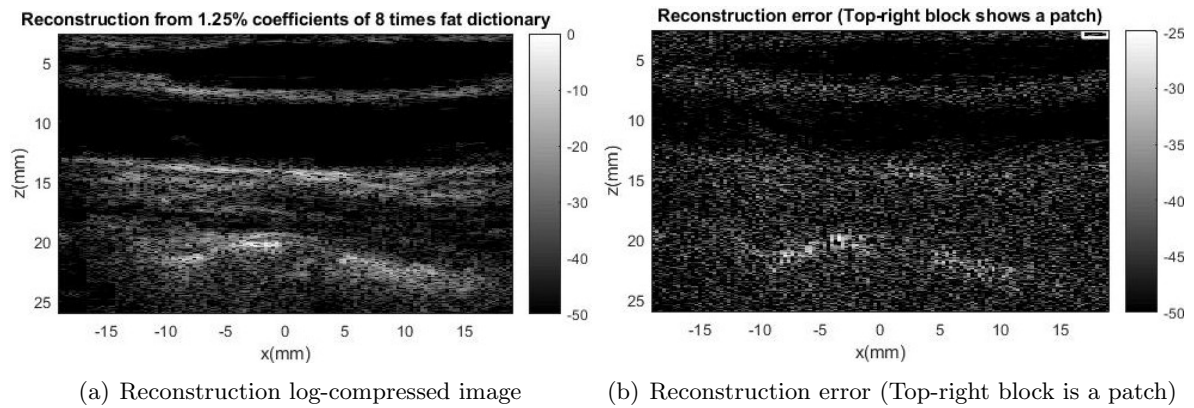


Figure 3.60: Reconstruction from about 1.25% number of the total 294912 representation coefficients (3686 coefficients) of the 8 times fatter dictionary matrix with patch size 8×8 .

From Figure 3.59(a), we can see that the small patch does reduce the block artifacts and the image quality is good. Comparing Figure 3.59(a) with Figure 3.60(a), their image quality looks similar. But, Comparing Figure 3.59(b) with Figure 3.60(b), we can see that the error shown in Figure 3.60(b) is less.

Above, the dictionary learning have been analyzed for the carotid longitudinal-sectional US image, but the carotid longitudinal-sectional images have simple structures that are mainly some lines. To check whether the dictionary learning can work well on the US images with more complicated structures, then, the simulations will be performed on the beamformed carotid cross-sectional US image. Figure 3.61 shows two beamformed carotid cross-sectional US images. We can see the lines and round holes in the images that are more complicated structures.

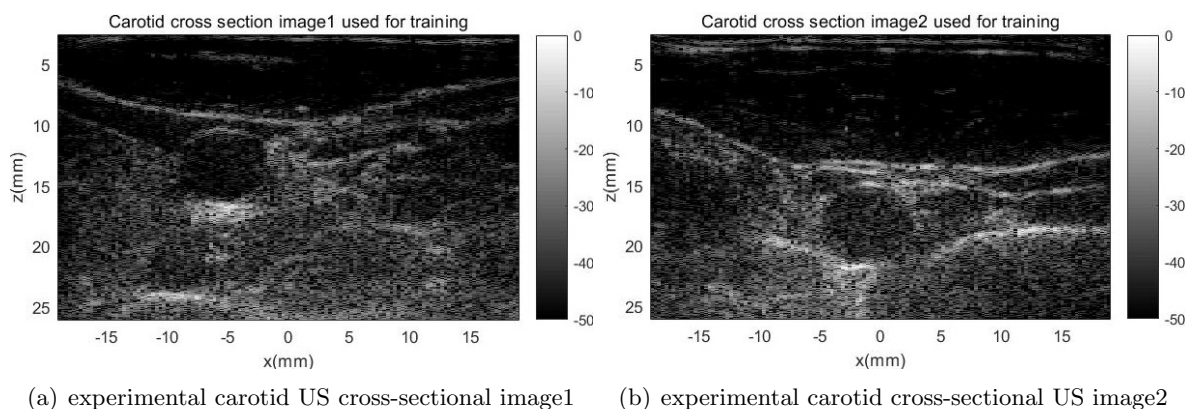


Figure 3.61: The experimental beamformed carotid cross-sectional US images used for training.

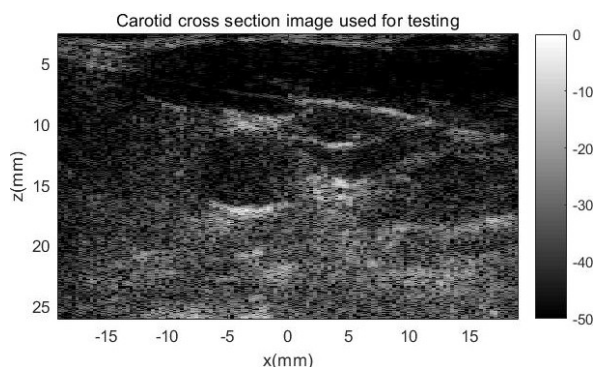


Figure 3.62: experimental beamformed carotid cross-sectional US image used for testing dictionary.

The images in Figure 3.61 will be used for training the sparse dictionary, and the image in Figure 3.62 will be used to test the learned dictionary. The 2D-DCTs of these three images are all cropped like what we did on the longitudinal-sectional images. The number of image pixels after cropping are also 288×128 .

The patch size is chosen to be 8×8 . And the dictionary length is chosen to be respectively the number of the pixels and 8 times thereof, so that two dictionaries are obtained with the same procedures as described above. The sparsity curves are compared in Figure 3.63. The long dictionary is sparser than the others.

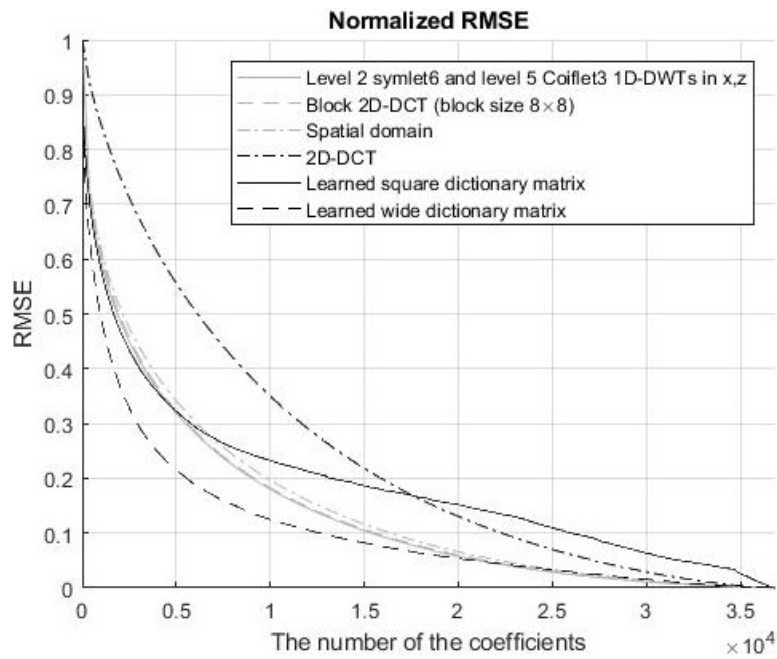


Figure 3.63: Comparison of sparsity of the dictionaries and sparsity in some other domains.

Figure 3.64 and Figure 3.65 show the reconstructions from the largest 3686 coefficients of some domains respectively.

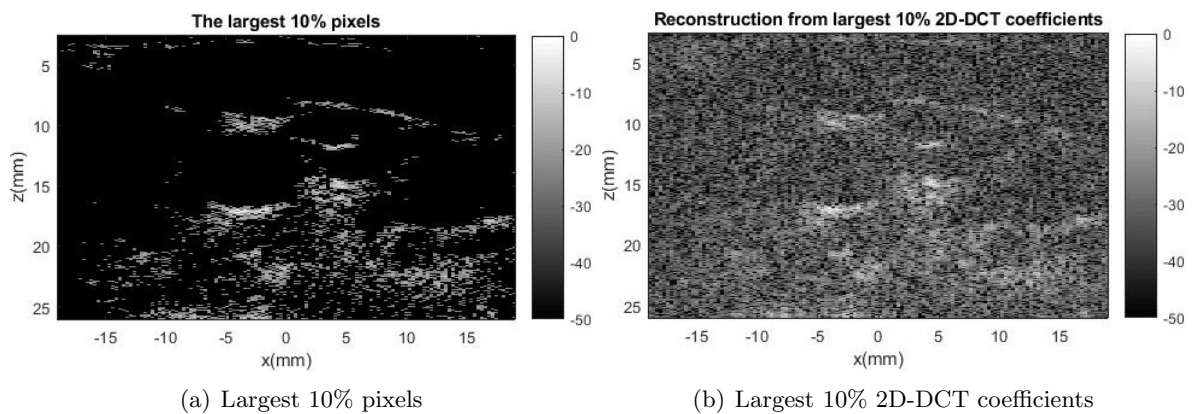


Figure 3.64: Reconstructions from largest 10% coefficients in spatial domain and 2D-DCT.

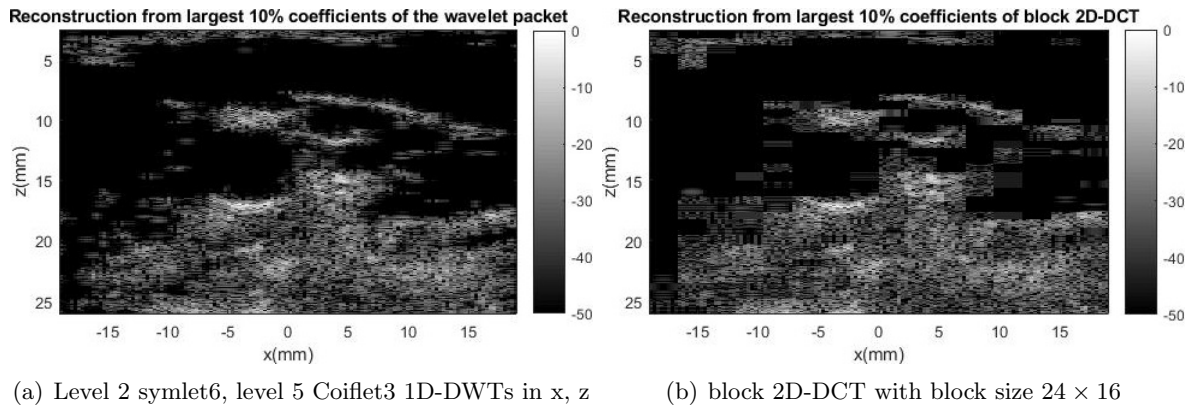


Figure 3.65: Reconstructions from the largest 10% coefficients of the wavelet packet performing different 1D-DWTs in two directions and the block 2D-DCT with block size 8×8 .

Figure 3.66 shows the reconstruction from about 10% coefficients (i.e., 3686 coefficients) of the dictionary whose length is equal to the image pixel number. It has many block artifacts. Compared with Figure 3.65(b) which also has many block artifacts, the image quality of Figure 3.66(a) is better. Compared with Figure 3.65(a), in Figure 3.66(a), the weak scatterers are reconstructed better.

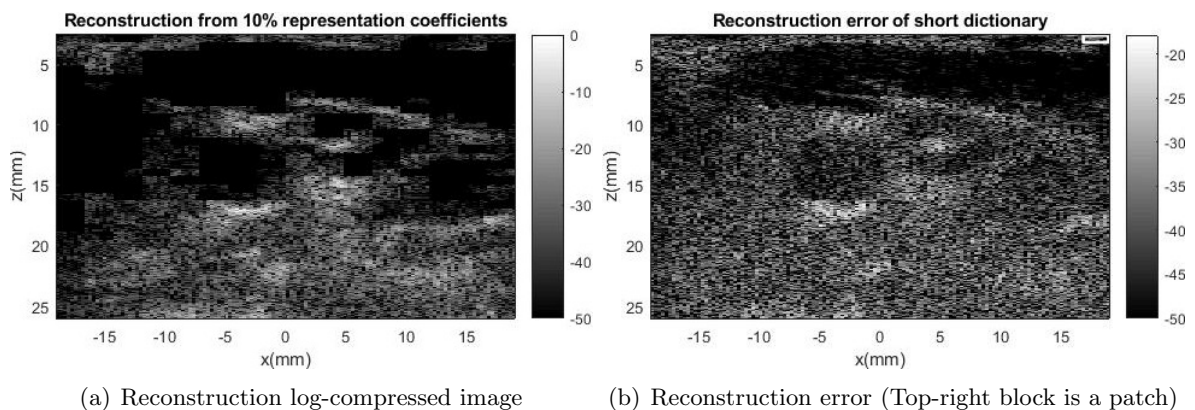


Figure 3.66: Reconstruction from about 10% number of total 36864 representation coefficients (i.e., 3686 coefficients) of the square dictionary matrix.

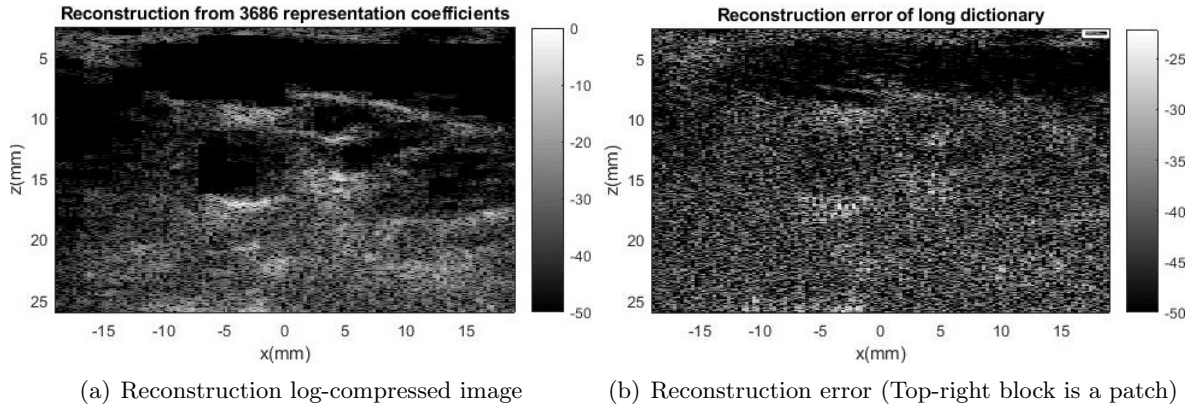


Figure 3.67: Reconstruction from about 1.25% number of total 294912 representation coefficients (i.e., 3686 coefficient) of the 8 times fat dictionary matrix.

Figure 3.67 shows the reconstruction from about 1.25% coefficients (i.e., 3686 coefficients) of the long dictionary whose length is 8 times the number of the pixels. It has very good image quality.

Therefore, to be the sparse space of the beamformed carotid US images, the dictionary learned by K-SVD works better than the normal transformations. And as the dictionary gets longer, the sparsity increases.

3.4 Reconstruction from the simulated US measurements

In this section, we show ultrasound reconstructions from simulated raw RF data, using l_1 -regularization with different bases. The simulation is performed in MATLAB. The imaging domain is approximately a $17.53\text{mm} \times 8.77\text{mm}$ rectangular area shown as figure 3.19 at page 25. The parameters here are the same as the parameters listed in table 3.1 at page 25. The transmitted ultrasound pulse here is also the same as that in Section 3.2.1, the response of which is formulated as (3.3) and shown as figure 3.20 at page 26. Here only 1 plane wave with a steering angle of 0° is transmitted. Here the SNR is defined as (3.5), where \mathbf{y} is the vector consisting of all the received signals and σ_n is the standard deviation of the additive white Gaussian noise (AWGN). The SNR here is 20dB.

$$SNR = 20 \lg(\|\mathbf{y}\|_\infty / \sigma_n). \quad (3.5)$$

To save the computer memory, the received signal \mathbf{y} and the system matrix \mathbf{A} is formulated in band-limited Fourier domain from +3.5MHz to +6.5MHz, which is shown as figure Figure 3.68.

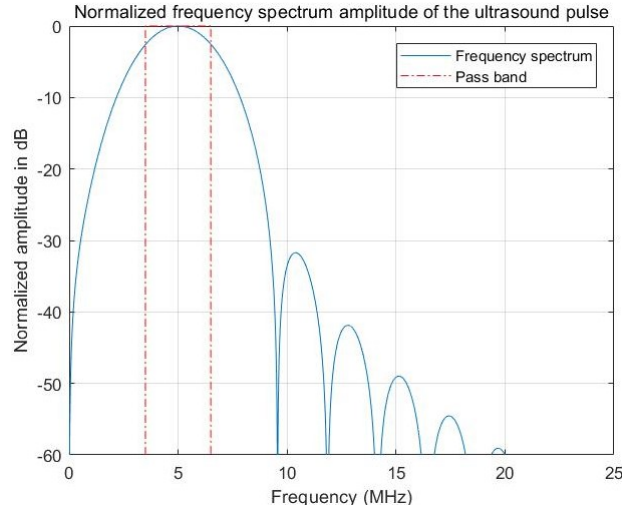


Figure 3.68: The frequency band from +3.5MHz to +6.5MHz.

The imaging grid is 160×96 that 160 pixels in z -direction and 96 pixels in x -direction. So the pixel size is about $54.79\mu m \times 182.62\mu m$ that z -directional and x -directional pixel lengths are about $54.79\mu m$ and $182.62\mu m$. There are about 5.62 and 1.69 pixels per wavelength in z -direction and x -direction respectively. LSQR algorithm solves (1.1) without l_1 -regularization. According to the experiments, it is found that the reconstructed image of 14 LSQR iterations is one of the results with best quality. The 14-iteration LSQR reconstruction is shown in Figure 3.69. The outline of the fetus phantom can be seen, but the image is distorted and has bad contrast.

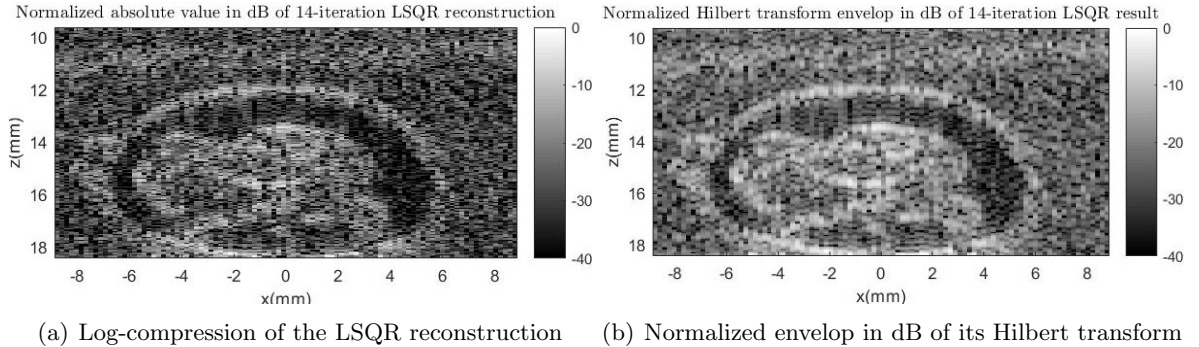


Figure 3.69: The 14-iteration LSQR reconstruction.

The YALL1 solver is used here to solve the l_1 -regularization problem, because of its high convergence speed. Figure 3.70 shows the reconstructions l_1 -regularized in the block 2D-DCT (block size 8×6) with τ equal to 0.0002, 0.002 and 0.006 respectively. Since the empty area in Figure 3.70(b) is darker and clearer than that in Figure 3.70(a), the reconstruction performance with $\tau = 0.0002$ is better than that with $\tau = 0.002$. In Figure 3.70(c), the image is distorted much and the intensity of background is not uniform along z -direction, so $\tau = 0.006$ is too large for the reconstruction. Therefore,

τ is equal to 0.002 in the remainder of the simulations.

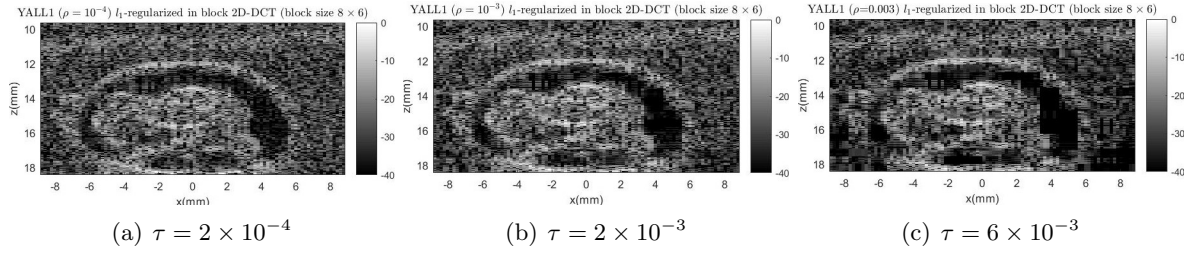
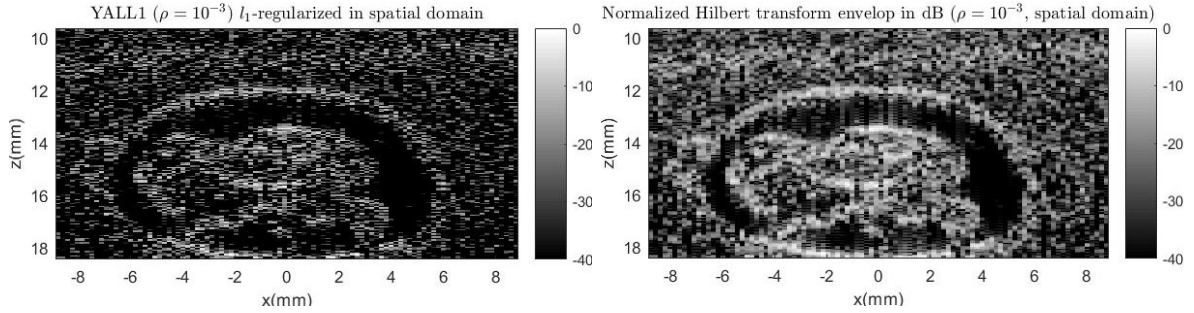


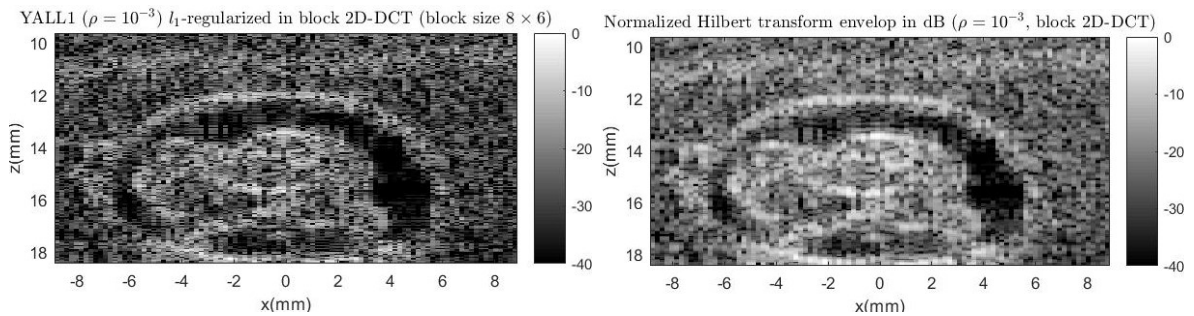
Figure 3.70: The YALL1 reconstruction l_1 -regularized in the block 2D-DCT (block size 8×6) with different τ .

The reconstruction l_1 -regularized in the spatial domain is shown as Figure 3.71. The image has many impulses and is much sparser than the true image, which is distorted. But compared with the LSQR result, it has better contrast.



(a) Normalized amplitude in dB of the reconstruction (b) Normalized envelop in dB of its Hilbert transform

Figure 3.71: The YALL1 reconstruction l_1 -regularized in the spatial domain and its Hilbert transform.

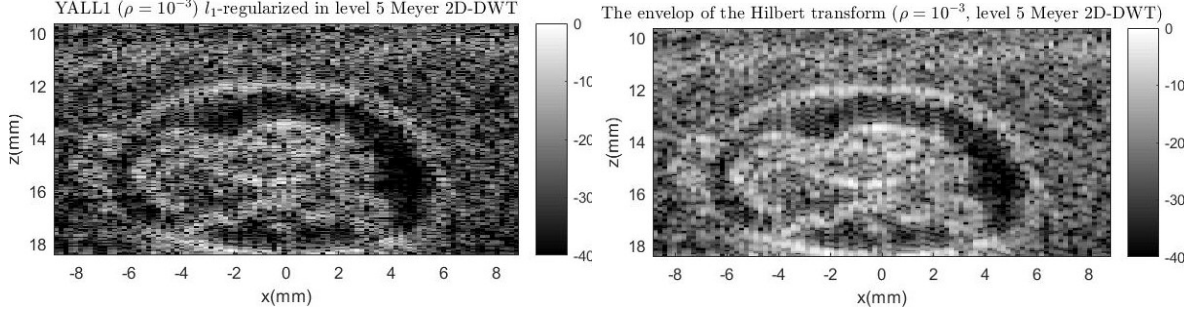


(a) Normalized amplitude in dB of the reconstruction (b) Normalized envelop in dB of the Hilbert transform

Figure 3.72: The YALL1 reconstruction l_1 -regularized in the block 2D-DCT (block size 8×6) and its Hilbert transform.

The reconstruction l_1 -regularized in the block 2D-DCT with block size 8×6 is shown

as Figure 3.72. Compared with LSQR result, large empty regions have good contrast, but the contrast of small empty regions are not good and the image has some block artifacts. This is because that the block size is not small enough.

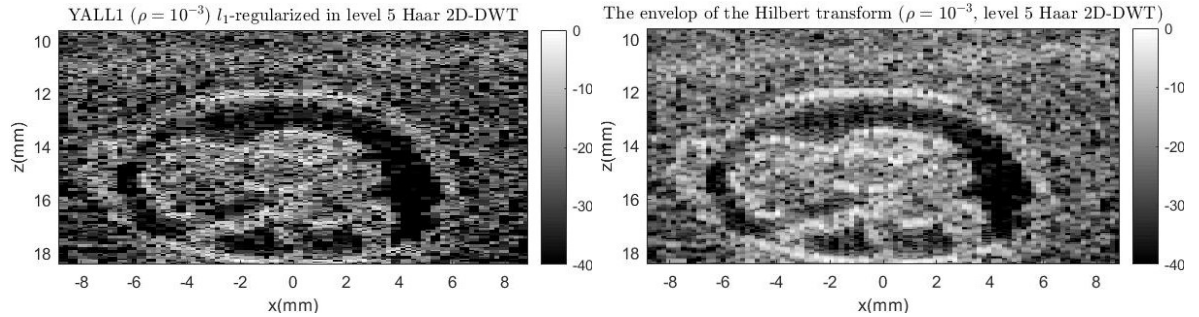


(a) Normalized amplitude in dB of the reconstruction (b) Normalized envelop in dB of the Hilbert transform

Figure 3.73: The YALL1 reconstruction l_1 -regularized in the level 5 Meyer 2D-DWT and its Hilbert transform.

The reconstruction l_1 -regularized in the level 5 Meyer 2D-DWT is shown as Figure 3.73. The empty regions do not have good contrast. This is because the Meyer filter is very long so that its spatial resolution is not good enough.

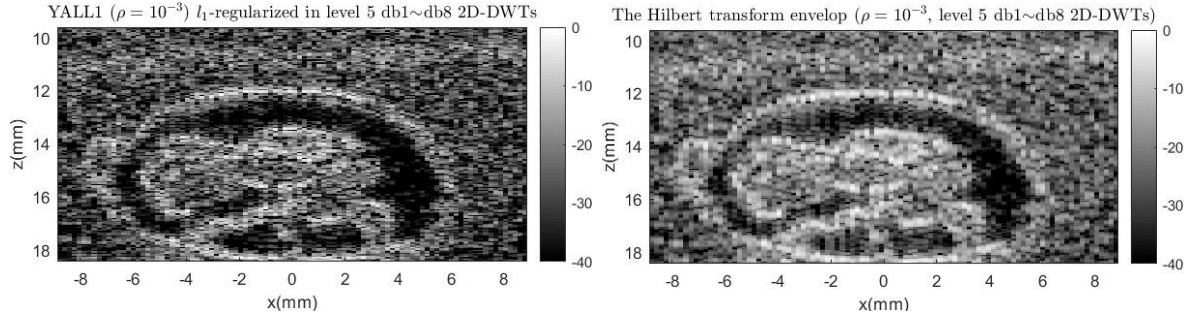
The reconstruction l_1 -regularized in the level 5 Haar 2D-DWT is shown as figure Figure 3.74. The image has better contrast in empty regions than Figure 3.72 and 3.73 except the block artifacts. The good contrast of empty region is because that the length of the Haar filter is only 2. Since the Haar filter coefficients have the same absolute values, the Haar 2D-DWT may be a good sparse representation of the homogeneous tissues.



(a) Normalized amplitude in dB of the reconstruction (b) Normalized envelop in dB of the Hilbert transform

Figure 3.74: The YALL1 reconstruction l_1 -regularized in the level 5 Haar 2D-DWT and its Hilbert transform.

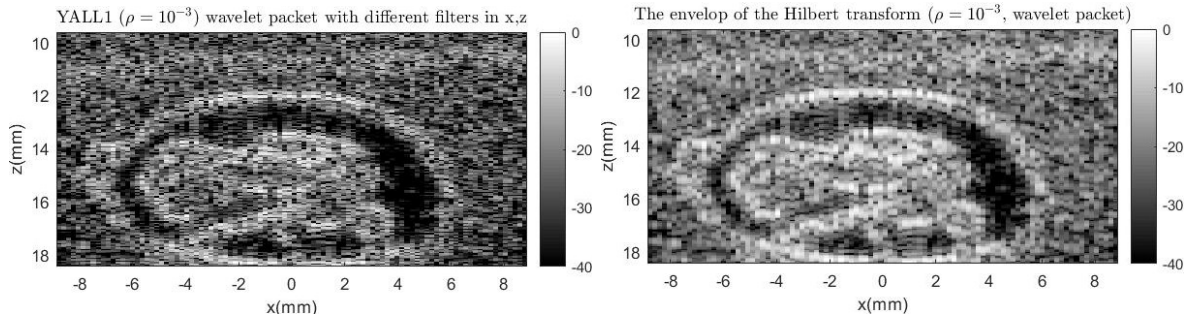
Since increasing the dictionary length can increase the sparsity, [5] uses a concatenation from Daubechies1 to Daubechies8 2D-DWTs as the sparse dictionary. Figure 3.75 shows the reconstruction of the fetus phantom in this thesis if using this dictionary. The image quality is not improved much compared with the above reconstructions.



(a) Normalized amplitude in dB of the reconstruction (b) Normalized envelop in dB of the Hilbert transform

Figure 3.75: The YALL1 reconstruction l_1 -regularized in the concatenation from Daubechies1 to Daubechies8 2D-DWTs and its Hilbert transform.

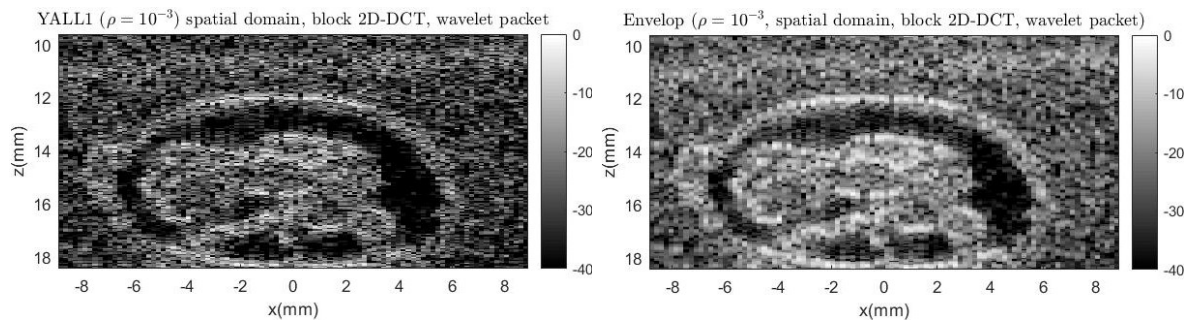
The sparsest transformation of the MF US images which is found in this study is the wavelet packet performing level 1 symlet6 and level 3 Coiflet3 in x and z directions. Figure 3.76 shows the reconstruction with it. The image quality is not much better than the above reconstructions. This is because that its sparsity is still not enough to improve the image quality of the reconstructions.



(a) Normalized amplitude in dB of the reconstruction (b) Normalized envelop in dB of the Hilbert transform

Figure 3.76: The YALL1 reconstruction l_1 -regularized in the wavelet packet transform and its Hilbert transform.

Then, to increase the sparsity, we use the concatenation of the sparse domain and block 2D-DCT and wavelet packet. The block size of the block 2D-DCT is 8×6 . The wave packet is the same as the transform used for Figure 3.76. The reconstruction is not improved much. Although increasing dictionary length can increase sparsity, the problem also becomes more complex as there are more variables to solve. Moreover, even though the three transforms are the sparsest, their concatenation is not necessarily the sparsest dictionary with this longer length.



(a) Normalized amplitude in dB of the reconstruction (b) Normalized envelop in dB of the Hilbert transform

Figure 3.77: The YALL1 reconstruction l_1 -regularized in the concatenation from Daubechies1 to Daubechies8 2D-DWTs and its Hilbert transform.

In this thesis, we first modeled the US imaging as a linear inverse problem and explain that a good sparse space of the US image can improve the US image reconstruction performance. This motivated us to find such a sparse space in this thesis. Next, we introduced two reconstruction algorithms LSQR, which can be used to l_2 -regularized linear inverse problem, and YALL1, which is used to solve the l_1 -regularized linear inverse problem. We also described a model for the US scattering intensity of a medical phantom. The inside of the tissue is modeled as the point-wise product of a scatter map and a zero-mean white Gaussian stochastic process, and some boundaries of the tissue are modeled as strong scatterers. Then, we introduced the 2D-DWT, wave atom, 2D-DCT and block 2D-DCT that are potentially good sparse transforms of medical US images, and we introduced a sparse dictionary learning algorithm, K-SVD.

After this, we computed and analyzed the sparsity of the US scattering intensity images before beamforming in the different transform spaces for both a fetus phantom and a kidney phantom. We also computed and analyzed the sparsity in different transform spaces of a beamformed fetus MF US image, simulated by computer, and a experimental carotid MF US image. Then, we performed the K-SVD sparse dictionary learning algorithm on several experimental beamformed carotid US images to obtain several dictionaries with different parameters, and we computed and analyzed the sparsity of the other experimental carotid US images in these dictionaries. At last, we reconstructed the US images from the simulated US measurement data using the LSQR and YALL1 algorithms, and we selected some transforms to use for the l_1 -regularization in the YALL1. We analyzed the effects of these transforms on reconstructed image quality.

There are four conclusions as below.

1. It is difficult to find a good sparse space of the pre-beamformed US scattering intensity images. The US scattering intensity can be modeled as the point-wise product of a scatter map and a white stochastic process. Due to this white stochastic process, a good sparse space hardly exists. This study does not find a transform sparser than its spatial domain.

2. As for the MF US images, its frequency characteristics are different in x and z directions, so the wavelet transforms with different filters in x and z directions can be sparser than the wavelet transforms with the same filters in two directions. However, the sparsity improvement is very little, though it typically presents a sparser transform than most 2D-DWT decompositions.

3. If there are suitable and sufficient samples for the sparse dictionary learning, the K-SVD algorithm can find a good square dictionary matrix from the experimental beamformed carotid US images. Compared with many other transforms, in this dictionary, we can use fewer coefficients to reconstruct a good-looking beamformed carotid US image. For the beamformed carotid US image with simpler structures, the dictionary works better. So it can be a good dictionary for the compression of these

images.

4. Increasing the dictionary length can make the images have much sparser representations. However, as for the reconstruction from the US measurements, longer dictionary might make the problem more complex, but this has not been investigated in this thesis. Actually, there is not a single transform in this study that results in a large image quality improvement of the reconstruction from raw RF data compared to the spatial domain and some other normal transforms.

Future work

There are four works that can be done in the future.

1. The wavelet packet transform in this study is not the best wavelet packet transform for the US images. Since wavelet packet has a lot of decomposition methods, also known as subband trees, the best subband tree can be selected according to some decomposition criteria. So future work can use suitable samples and decomposition criteria to find sparser wavelet packet transforms. For instance, the decomposition criteria are the l_1 -norm of the coefficient vector. Namely, the decomposition will not be performed if it will increase the l_1 -norm. In this way, we can obtain sparser wavelet packet transforms.

2. The sparse dictionary learning in this thesis does not involve the matrix \mathbf{A} . In future work, we can take account of \mathbf{A} when training the sparse dictionary. As an example, the optimization problem of the dictionary learning can be written as (5.1). \mathbf{Y} is the set of the samples of the measurement data. \mathbf{A} should be the array manifold matrix with wider bandwidth or multiple PWs so that it can reconstruct better US images. Other variables are explained in Section 2.3.3 in page 10.

$$\min_{\mathbf{D}, \mathbf{\Gamma}} \{ \|\mathbf{Y} - \mathbf{A}\mathbf{D}\mathbf{\Gamma}\|_F^2 \} \quad \text{s.t.} \quad \forall i, \|\gamma_i\|_0 \leq T_0. \quad (5.1)$$

However, this problem is too large to use the K-SVD algorithm. So we need to use the other algorithms or reduce the computation complexity of this problem.

3. Future work can focus on finding the optimal dictionary length. We can also try finding a good concatenation of well-known transforms to be the sparse dictionary.

4. Figure 2.2 on page 8 shows that the model of US scattering intensity is the point-wise product of a scatter map and a white Gaussian process. Scatter map can be regarded as an ideal image. Usually, it is easy to find good sparse spaces for the scatter map of the US images. In this study, the sparsity of the scatter map is not utilized to find a sparse space of the medical US images, so future work can take advantage of the sparsity of the scatter map. The following is a possible research direction to make use of this sparsity.

According to Section 2.1 in page 5, the scattering intensity image can be approximated as (5.2), where \mathbf{x} is the scattering intensity image vector and $\mathbf{m}_x \in \mathbb{R}_{>0}^{N \times 1}$ is the scatter map vector and $\mathbf{w}_x \in \mathbb{R}^{N \times 1}$ is the stochastic process. \circ indicates the Hadamard product, which is an element-wise product of two vectors and can also be expressed as the product of a diagonal matrix and a vector.[24] $\mathbf{\Lambda}_{\mathbf{m}_x} \in \mathbb{R}^{N \times N}$ and $\mathbf{\Lambda}_{\mathbf{w}_x} \in \mathbb{R}^{N \times N}$ are two diagonal matrices with \mathbf{m}_x and \mathbf{w}_x as their leading diagonals. If the sparse transform of the scatter map is known, \mathbf{m}_x can be expressed as (5.2), where $\mathbf{\Psi}_{\mathbf{m}_x} \in \mathbb{C}^{N \times K}$ denotes the sparse dictionary matrix of \mathbf{m}_x and $\mathbf{c}_x \in \mathbb{R}^{K \times 1}$ indicates the representation

coefficient vector.

$$\mathbf{x} = \mathbf{m}_x \circ \mathbf{w}_x = \Lambda_{\mathbf{m}_x} \mathbf{w}_x = \Lambda_{\mathbf{w}_x} \mathbf{m}_x, \quad \mathbf{m}_x = \Psi_{\mathbf{m}_x} \mathbf{c}_x. \quad (5.2)$$

Therefore, (1.1) in page 2 can be rewritten as (5.3). We are not interested in \mathbf{w}_x , so $\hat{\mathbf{w}}_x$ does not have to be very close to \mathbf{w}_x . Then, sufficient dimensionality reduction or a good sparse space of $\hat{\mathbf{w}}_x$ can help us to find a good sparse space of the US images, which is explained below.

$$\mathbf{y} = \mathbf{A} \Lambda_{\mathbf{m}_x} \hat{\mathbf{w}}_x + \mathbf{n} = \mathbf{A} \Lambda_{\hat{\mathbf{w}}_x} \mathbf{m}_x + \mathbf{n} = \mathbf{A} \Lambda_{\hat{\mathbf{w}}_x} \Psi_{\mathbf{m}_x} \mathbf{c}_x + \mathbf{n}. \quad (5.3)$$

Assume $\mathbf{D}_{\hat{\mathbf{w}}_x} = [\mathbf{e}_{\hat{\mathbf{w}}_x,1} \cdots \mathbf{e}_{\hat{\mathbf{w}}_x,\tilde{N}}]_{N \times \tilde{N}}$ is a dictionary matrix of $\hat{\mathbf{w}}_x$ and $c_{\hat{\mathbf{w}}_x,i}$ are its representation coefficients. Then, (5.3) can be rewritten as (5.4). If we can find a dictionary $\mathbf{D}_{\hat{\mathbf{w}}_x}$ of $\hat{\mathbf{w}}_x$ that can make $c_{\hat{\mathbf{w}}_x,i}$ sparse enough or can make \tilde{N} small enough, vector $[c_{\hat{\mathbf{w}}_x,1} \mathbf{c}_x^T \cdots c_{\hat{\mathbf{w}}_x,\tilde{N}} \mathbf{c}_x^T]_{1 \times \tilde{N}K}$ can be very sparse so that $[\Lambda_{\mathbf{e}_{\hat{\mathbf{w}}_x,1}} \Psi_{\mathbf{m}_x} \cdots \Lambda_{\mathbf{e}_{\hat{\mathbf{w}}_x,\tilde{N}}} \Psi_{\mathbf{m}_x}]_{N \times \tilde{N}K}$ may be a good sparse dictionary of the medical US images. In addition, some assumptions can be used to constrain the stochastic process $\hat{\mathbf{w}}_x$, such as stationarity, mean, variance, auto-correlation, PSD, etc.

$$\begin{aligned} \mathbf{y} &= \mathbf{A} \Lambda_{\hat{\mathbf{w}}_x} \Psi_{\mathbf{m}_x} \mathbf{c}_x + \mathbf{n} = \mathbf{A} \sum_{i=1}^{\tilde{N}} c_{\hat{\mathbf{w}}_x,i} \Lambda_{\mathbf{e}_{\hat{\mathbf{w}}_x,i}} \Psi_{\mathbf{m}_x} \mathbf{c}_x + \mathbf{n} \\ &= \mathbf{A} [\Lambda_{\mathbf{e}_{\hat{\mathbf{w}}_x,1}} \Psi_{\mathbf{m}_x} \cdots \Lambda_{\mathbf{e}_{\hat{\mathbf{w}}_x,\tilde{N}}} \Psi_{\mathbf{m}_x}] [c_{\hat{\mathbf{w}}_x,1} \mathbf{c}_x^T \cdots c_{\hat{\mathbf{w}}_x,\tilde{N}} \mathbf{c}_x^T]^T \end{aligned} \quad (5.4)$$

Bibliography

- [1] Michal Aharon, Michael Elad, Alfred Bruckstein, et al. K-svd: An algorithm for designing overcomplete dictionaries for sparse representation. *IEEE Transactions on signal processing*, 54(11):4311, 2006.
- [2] Ali Naci Akansu and Yipeng Liu. On-signal decomposition techniques. *Optical Engineering*, 30(7):912–921, 1991.
- [3] Amir Beck and Marc Teboulle. A fast iterative shrinkage-thresholding algorithm for linear inverse problems. *SIAM journal on imaging sciences*, 2(1):183–202, 2009.
- [4] Stephen Becker, Jérôme Bobin, and Emmanuel J Candès. NESTA: A fast and accurate first-order method for sparse recovery. *SIAM Journal on Imaging Sciences*, 4(1):1–39, 2011.
- [5] Adrien Besson, Rafael E Carrillo, Olivier Bernard, Yves Wiaux, and Jean-Philippe Thiran. Compressed delay-and-sum beamforming for ultrafast ultrasound imaging. In *Image Processing (ICIP), 2016 IEEE International Conference on*, pages 2509–2513. Ieee, 2016.
- [6] Marta M Betcke, Ben T Cox, Nam Huynh, Edward Z Zhang, Paul C Beard, and Simon R Arridge. Acoustic wave field reconstruction from compressed measurements with application in photoacoustic tomography. *IEEE Transactions on Computational Imaging*, 3(4):710–721, 2017.
- [7] José M Bioucas-Dias and Mário AT Figueiredo. A new twist: two-step iterative shrinkage/thresholding algorithms for image restoration. *IEEE Transactions on Image processing*, 16(12):2992–3004, 2007.
- [8] Guillaume David, Jean-luc Robert, Bo Zhang, and Andrew F Laine. Time domain compressive beam forming of ultrasound signals. *The Journal of the Acoustical Society of America*, 137(5):2773–2784, 2015.
- [9] Laurent Demanet and Lexing Ying. Wave atoms and sparsity of oscillatory patterns. *Applied and Computational Harmonic Analysis*, 23(3):368–387, 2007.
- [10] Minh N Do and Martin Vetterli. The contourlet transform: an efficient directional multiresolution image representation. *IEEE Transactions on image processing*, 14(12):2091–2106, 2005.
- [11] David L Donoho and Philip B Stark. Uncertainty principles and signal recovery. *SIAM Journal on Applied Mathematics*, 49(3):906–931, 1989.
- [12] Michael A Ellis, Francesco Viola, and William F Walker. Super-resolution image reconstruction using diffuse source models. *Ultrasound in medicine & biology*, 36(6):967–977, 2010.

- [13] Kjersti Engan, Sven Ole Aase, and J Hakon Husoy. Method of optimal directions for frame design. In *Acoustics, Speech, and Signal Processing, 1999. Proceedings., 1999 IEEE International Conference on*, volume 5, pages 2443–2446. IEEE, 1999.
- [14] Jalal Fadili and Jean-Luc Starck. Curvelets and ridgelets. In *Computational Complexity*, pages 754–773. Springer, 2012.
- [15] Per Christian Hansen. *Discrete inverse problems: insight and algorithms*, volume 7. Siam, 2010.
- [16] Jørgen A Jensen. Ultrasound imaging and its modeling. In *Imaging of Complex Media with Acoustic and Seismic Waves*, pages 135–166. Springer, 2002.
- [17] Jørgen Arendt Jensen. Field: A program for simulating ultrasound systems. In *10TH NORDICBALTIC CONFERENCE ON BIOMEDICAL IMAGING, VOL. 4, SUPPLEMENT 1, PART 1: 351–353*. Citeseer, 1996.
- [18] Jørgen Arendt Jensen and Peter Munk. Computer phantoms for simulating ultrasound b-mode and cfm images. In *Acoustical imaging*, pages 75–80. Springer, 1997.
- [19] Jørgen Arendt Jensen and Niels Bruun Svendsen. Calculation of pressure fields from arbitrarily shaped, apodized, and excited ultrasound transducers. *IEEE transactions on ultrasonics, ferroelectrics, and frequency control*, 39(2):262–267, 1992.
- [20] Silvan Kraft, Athanasios Karamalis, Debdoot Sheet, Enken Drecol, Ernst J Rummeny, Nassir Navab, Peter B Noël, and Amin Katouzian. Introducing nuclei scatterer patterns into histology based intravascular ultrasound simulation framework. In *Medical Imaging 2013: Ultrasonic Imaging, Tomography, and Therapy*, volume 8675, page 86750Y. International Society for Optics and Photonics, 2013.
- [21] Roberto Lavarello, Farzad Kamalabadi, and William D O’Brien. A regularized inverse approach to ultrasonic pulse-echo imaging. *IEEE transactions on medical imaging*, 25(6):712–722, 2006.
- [22] Hervé Liebgott, Rémy Prost, and Denis Friboulet. Pre-beamformed rf signal reconstruction in medical ultrasound using compressive sensing. *Ultrasonics*, 53(2):525–533, 2013.
- [23] Jing Liu, Qiong He, and Jianwen Luo. A compressed sensing strategy for synthetic transmit aperture ultrasound imaging. *IEEE transactions on medical imaging*, 36(4):878–891, 2017.
- [24] Elizabeth Million. The hadamard product. *Course Notes*, 3:6, 2007.
- [25] C. Paige and M. Saunders. Lsqr: Sparse equations and least squares. *online at (<http://web.stanford.edu/group/SOL/software/lsqr/>)*, 2012.

- [26] Christopher C Paige and Michael A Saunders. Lsqr: An algorithm for sparse linear equations and sparse least squares. *ACM Transactions on Mathematical Software (TOMS)*, 8(1):43–71, 1982.
- [27] An Hoai Pham, Bjarne Stage, Martin Christian Hemmsen, Bo Lundgren, Mads Møller Pedersen, Tina Bock Pedersen, and Jørgen Arendt Jensen. Simulation of ultrasound backscatter images from fish. In *Medical Imaging 2011: Physics of Medical Imaging*, volume 7961, page 796152. International Society for Optics and Photonics, 2011.
- [28] Céline Quinsac, Adrian Basarab, Jean-Marc Girault, and Denis Kouamé. Compressed sensing of ultrasound images: Sampling of spatial and frequency domains. In *Signal Processing Systems (SIPS), 2010 IEEE Workshop on*, pages 231–236. IEEE, 2010.
- [29] Ron Rubinstein, Michael Zibulevsky, and Michael Elad. Efficient implementation of the k-svd algorithm using batch orthogonal matching pursuit. Technical report, Computer Science Department, Technion, 2008.
- [30] Martin F Schiffner and Georg Schmitz. Fast pulse-echo ultrasound imaging employing compressive sensing. In *Ultrasonics Symposium (IUS), 2011 IEEE International*, pages 688–691. IEEE, 2011.
- [31] Ivan W Selesnick. Wavelet transforms—a quick study. *Physics Today magazine*, 2007.
- [32] Kaushal K Shukla and Arvind K Tiwari. *Efficient algorithms for discrete wavelet transform: with applications to denoising and fuzzy inference systems*. Springer Science & Business Media, 2013.
- [33] Andreas M Tillmann. On the computational intractability of exact and approximate dictionary learning. *IEEE Signal Processing Letters*, 22(1):45–49, 2015.
- [34] E. van den Berg and M. P. Friedlander. SPGL1: A solver for large-scale sparse reconstruction, June 2007. <http://www.cs.ubc.ca/labs/scl/spgl1>.
- [35] Pim Q. van der Meulen. Regularized least squares imaging for high resolution ultrasound. Master’s thesis, Delft University of Technology, September 2016.
- [36] V Vermehren and HM de Oliveira. Close expressions for meyer wavelet and scale function. *arXiv preprint arXiv:1502.00161*, 2015.
- [37] Francesco Viola, Michael A Ellis, and William F Walker. Time-domain optimized near-field estimator for ultrasound imaging: Initial development and results. *IEEE Transactions on Medical Imaging*, 27(1):99–110, 2008.
- [38] Gregory K Wallace. The jpeg still picture compression standard. *IEEE transactions on consumer electronics*, 38(1):xviii–xxxiv, 1992.
- [39] Junfeng Yang and Yin Zhang. Alternating direction algorithms for L1-problems in compressive sensing. *SIAM journal on scientific computing*, 33(1):250–278, 2011.

- [40] Y Zhang, J Yang, and Wotao Yin. Yall1: Your algorithms for L1. *online at* (<http://yall1.blogs.rice.edu>), 2011.

List of Figures

1.1	Sketch of the US pulse propagation during US imaging	1
2.1	Sketch of \mathbf{A} matrix construction.	5
2.2	The sketch showing the constitution of the computer medical US phantom.	8
2.3	The filter bank describing the DWTs.	9
3.1	The linear interpolation image of the fetus phantom US scattering intensity.	14
3.2	Comparison among the different levels of the Haar 2D-DWT and the Meyer 2D-DWT.	15
3.3	Comparison among the different Daubechies in level 1 and comparison among the block 2D-DCT with the different block sizes.	16
3.4	Comparison among the spatial domain, the 2D-DCT, the Haar 2D-DWT, the discrete Meyer 2D-DWT, block 2D-DCT and 2D-FFT.	16
3.5	The 2D-FFT and 2D-DCT normalized spectrum in dB of the fetus phantom interpolation image.	17
3.6	The level 1 Haar DWT of the fetus phantom interpolation image, and its maximum 15% coefficients.	17
3.7	The normalized absolute values from -40dB to 0dB of: (a) the reconstruction from the maximum 15% level 1 Haar DWT coefficients; (b) the maximum 15% pixels of the fetus phantom interpolation image.	18
3.8	The maximum 15% 2D-FFT and 2D-DCT coefficients of the fetus phantom interpolation image.	18
3.9	The log-compression from -40dB to 0dB of the reconstruction from the maximum 15% 2D-DCT coefficients and 2D-FFT coefficients respectively.	19
3.10	The linear interpolation image of the kidney phantom scattering intensity.	19
3.11	Comparison among the different levels of the Daubechies2 DWT and the discrete Meyer DWT.	20
3.12	Comparison among the different Daubechies in level 1 and comparison among the block 2D-DCT with the different block sizes.	20
3.13	Comparison of the sparsity among the spatial domain, the 2D-DCT, the Haar DWT, the discrete Meyer DWT, block 2D-DCT and 2D-FFT of the kidney phantom and comparison of the sparsity between the fetus phantom and the kidney phantom.	21
3.14	The 2D-FFT and 2D-DCT normalized spectrum in dB of the kidney phantom interpolation image.	21
3.15	The level 1 Daubechies2 DWT of the kidney phantom interpolation image, and its maximum 15% coefficients.	22
3.16	The normalized absolute values in dB of the reconstruction from the maximum 15% coefficients in level 1 Daubechies2 DWT, and the maximum 15% pixels of the kidney phantom interpolation image.	22
3.17	The maximum 15% 2D-FFT and 2D-DCT coefficients of the kidney phantom interpolation image.	23

3.18	The normalized absolute values in dB of the reconstruction from the maximum 15% 2D-FFT and 2D-DCT coefficients.	23
3.19	The imaging domain.	25
3.20	The time response and the normalized frequency spectrum of the US pulse. 26	
3.21	The normalized envelopes in dB of the noiseless fetus phantom 3-PW and 6-PW MF images.	26
3.22	The normalized absolute values in dB of the noiseless fetus phantom 21-PW MF image.	27
3.23	The normalized envelop in dB of the z-directional Hilbert transformation. 27	
3.24	The 2D-FFT and 2D-DCT normalized envelop of the fetus phantom 21-PW MF image.	28
3.25	The normalized absolute values in dB of Nyquist sampling fetus phantom MF image and its 2D-FFT and 2D-DCT.	28
3.26	The normalized envelop from -40dB to 0dB of the Hilbert transformation with Tukey window in z-direction of the Nyquist sampling fetus phantom MF image.	29
3.27	Comparison among the different levels of the symlet6 and the Coiflet3. 29	
3.28	Comparison of the different 2D-DWTs.	30
3.29	The sparsity of block 2D-DCT and some other transformations.	31
3.30	The level 5 discrete Meyer DWT of the fetus phantom 21-PW MF image, and the positions of its maximum 15% coefficients.	31
3.31	The wavelet packet performing level 1 symlet6 and level 3 Coiflet3 1D-DWTs in x and z directions of the fetus phantom 21-PW MF image, and the positions of its maximum 15% coefficients.	32
3.32	The block 2D-DCT in dB with block size 8×6 of the fetus phantom 21-PW MF image, and the positions of its maximum 15% coefficients. .	32
3.33	The wave atom in dB of the fetus phantom 21-PW MF image, and the positions of its maximum coefficients.	33
3.34	The reconstruction from the maximum 15% coefficients in level 5 discrete Meyer DWT and the wavelet packet performing level 1 symlet6 and level 3 Coiflet3 1D-DWTs in x and z directions.	33
3.35	The reconstructions from the maximum 15% pixel number coefficients in block 2D-DCT with block size 8×6 and in wave atom of the fetus phantom 21-PW MF image.	34
3.36	The maximum 15% pixels of the fetus phantom 21-PW MF image, and the maximum 15% 2D-DCT coefficients of the fetus phantom MF image, and the normalized absolute values in dB of the reconstruction from the maximum 15% 2D-DCT coefficients.	34
3.37	The 901×246 carotid ultrasound image.	35
3.38	The normalized 2D-FFT and 2D-DCT spectrum from -50dB to 0dB of both the carotid ultrasound images before and after truncating and windowing in the 2D-DCT.	36
3.39	The carotid image from the cropped and windowed 2D-DCT and its z-directional Hilbert transform envelop in dB.	36

3.40	Comparison of the different levels the Meyer 2D-DWT and different level 5 Daubechies 2D-DWT.	37
3.41	Comparison of the different 2D-DWTs and comparison of the block 2D-DCT with the different block sizes.	37
3.42	Sparsity of some other transformations and comparison of the sparsity between the fetus phantom MF image and the carotid ultrasound image.	38
3.43	The carotid image level 5 Meyer 2D-DWT normalized spectrum in dB, and the positions of its maximum 15% coefficients.	39
3.44	Normalized spectrum in dB of wavelet packet performing level 2 symlet6 and level 5 Coiflet3 1D-DWTs in x and z direction, and the positions of its maximum 15% coefficients.	39
3.45	The block 2D-DCT normalized spectrum in dB with block size 8×8 of the carotid image, and the positions of its maximum 15% coefficients.	40
3.46	The wave atom in dB of the fetus phantom 21-PW MF image, and the positions of its maximum coefficients.	40
3.47	The reconstruction from the maximum 15% coefficients in level 5 Meyer 2D-DWT, and the maximum 15% pixels of the carotid image.	41
3.48	The reconstructions from the maximum 15% pixel number coefficients in block 2D-DCT with block size 8×8 and in the wave atom of the carotid image.	41
3.49	The reconstruction from the largest 15% coefficients of level 2 symlet6 and level 5 Coiflet3 1D-DWTs in x and z directions	42
3.50	Maximum 15% coefficients and their reconstructions for 2D-DCT and 2D-FFT of carotid image.	42
3.51	The experimental beamformed carotid images used for training, and their 2D-DCTs.	43
3.52	The cropped 2D-DCT of the carotid US image I, and the training images reconstructed from their cropped 2D-DCTs (image1 and 2 correspond to image I and II).	44
3.53	A experimental beamformed carotid image used for testing the dictionary.	45
3.54	The sparsity curves of the learned sparse dictionary and some other transforms.	45
3.55	Reconstructions from largest 10% coefficients in spatial domain and 2D-DCT.	46
3.56	Reconstructions from the largest 10% coefficients of the different 1D-DWT in each direction and the block 2D-DCT with block size 24×16	46
3.57	Reconstruction from 10% number of the representation coefficients of the learned dictionary with patch size 24×16 , and the error between reconstruction and true image.	46
3.58	Sparsity comparison of three different sparse dictionaries.	47
3.59	Reconstruction from about 10% number of the total 36864 representation coefficients (3686 coefficients) of the square dictionary matrix with patch size 8×8	48

3.60	Reconstruction from about 1.25% number of the total 294912 representation coefficients (3686 coefficients) of the 8 times fatter dictionary matrix with patch size 8×8	48
3.61	The experimental beamformed carotid cross-sectional US images used for training.	49
3.62	experimental beamformed carotid cross-sectional US image used for testing dictionary.	49
3.63	Comparison of sparsity of the dictionaries and sparsity in soome other domains.	50
3.64	Reconstructions from largest 10% coefficients in spatial domain and 2D-DCT.	50
3.65	Reconstructions from the largest 10% coefficients of the wavelet packet performing different 1D-DWTs in two directions and the block 2D-DCT with block size 8×8	51
3.66	Reconstruction from about 10% number of total 36864 representation coefficients (i.e., 3686 coefficients) of the square dictionary matrix. . . .	51
3.67	Reconstruction from about 1.25% number of total 294912 representation coefficients (i.e., 3686 coefficient) of the 8 times fat dictionary matrix. .	52
3.68	The frequency band from +3.5MHz to +6.5MHz.	53
3.69	The 14-iteration LSQR reconstruction.	53
3.70	The YALL1 reconstruction l_1 -regularized in the block 2D-DCT (block size 8×6) with different τ	54
3.71	The YALL1 reconstruction l_1 -regularized in the spatial domain and its Hilbert transform.	54
3.72	The YALL1 reconstruction l_1 -regularized in the block 2D-DCT (block size 8×6) and its Hilbert transform.	54
3.73	The YALL1 reconstruction l_1 -regularized in the level 5 Meyer 2D-DWT and its Hilbert transform.	55
3.74	The YALL1 reconstruction l_1 -regularized in the level 5 Haar 2D-DWT and its Hilbert transform.	55
3.75	The YALL1 reconstruction l_1 -regularized in the concatenation from Daubechies1 to Daubechies8 2D-DWTs and its Hilbert transform. . . .	56
3.76	The YALL1 reconstruction l_1 -regularized in the wavelet packet transform and its Hilbert transform.	56
3.77	The YALL1 reconstruction l_1 -regularized in the concatenation from Daubechies1 to Daubechies8 2D-DWTs and its Hilbert transform. . . .	57

List of Tables

3.1	Parameters of the fetus phantom MF image	25
3.2	Parameters of the experimental carotid MF image	35